Real Time Density Functional Simulations of Quantum Scale Conductance

by

Jeremy Scott Evans

B.A., Franklin & Marshall College (2003)

Submitted to the Department of Chemistry
in partial fulfillment of the requirements for the degree of

Doctor of Philosophy

at the

MASSACHUSETTS INSTITUTE OF TECHNOLOGY

June 2009

Author .....
Department of Chemistry
February 2, 2009

Certified by .....
Troy Van Voorhis
Associate Professor of Chemistry
Thesis Supervisor

Accepted by .....
Robert W. Field
Chairman, Department Committee on Graduate Theses

This doctoral thesis has been examined by a Committee of the Department of Chemistry as follows:

Professor Robert J. Silbey .....

Chairman, Thesis Committee

Class of 1942 Professor of Chemistry

Professor Troy Van Voorhis .....

Thesis Supervisor

Associate Professor of Chemistry

Professor Jianshu Cao .....

Member, Thesis Committee

Associate Professor of Chemistry

Real Time Density Functional Simulations of Quantum Scale Conductance

by

Jeremy Scott Evans

Submitted to the Department of Chemistry
on February 2, 2009, in partial fulfillment of the
requirements for the degree of
Doctor of Philosophy

Abstract

We study electronic conductance through single molecules by subjecting a molecular junction to a time dependent potential and propagating the electronic state in real time using time-dependent density functional theory (TDDFT). This is in contrast with the more common steady-state nonequilibrium Green's function (NEGF) method. We start by examining quantum scale conductance methods in both the steady state and real-time formulations followed by a review of computational quantum chemistry methods. We then develop the real-time density functional theory and numerical solution techniques and use them to examine transport in a simple *trans*-polyacetylene wire. The remaining chapters are devoted to examining real-time transport behavior of various systems and model chemistries. Open-shell calculation of the polyacetylene wire reveal that, in agreement with various correlated model calculations, charge and spin behave as separate quasiparticles with different rates of transport. However, the transport of charge, and especially spin are highly dependent upon the amount of exact exchange included in the approximate exchange-correlation energy functional. This functional dependence is further illustrated when we demonstrate that the conductance gap of a device imperfectly coupled to wires varies based upon the non-local exchange and correlation. We also study the dynamic transport behavior of benzene-1,4-dithiol (BDT) coupled to gold leads and find that both the transient current and device charge density fluctuate with time,. This suggests that the steady-state assumption of the NEGF method may not be accurate.

Thesis Supervisor: Troy Van Voorhis
Title: Associate Professor of Chemistry

Acknowledgments

I first thank my advisor Troy Van Voorhis, whose continued guidance and leadership made this work possible. Troy's mentoring was instrumental in allowing me to develop as a scientist and in bringing me to a place to make meaningful contributions to the scientific community. His door was always open, and he showed me how to make the best use of the time I devoted to my research.

I thank the members of my thesis committee, Dr. Robert J. Silbey and Dr. Jianshu Cao, for their advice through the years and in developing this thesis. I thank Dr. Richard Moog who first taught me quantum mechanics. I thank as well my undergraduate research advisor, Dr. Ronald Musselman for giving me a taste of research and the confidence to pursue my degree here at MIT.

My research colleagues were integral in making my time here interesting and enjoyable. I thank Steve Presse, Jim Witkoskie, Qin Wu, Indranil Rudra, Xiaogeng Song, Seth Difley, Eric Zimányi, Aiyan Lu, Carter Lin, Lee-Ping Wang, Tim Kowalczyk and Ben Kaduk for intersting conversations and for maintaining a friendly atmosphere in the "zoo". I would espescially like to thank Chiao-Lun Cheng and Oleg Vydrov who collaborated on some of the research included in this thesis.

I thank the members of Community of Faith Christian Fellowship who have truly been a family to me in Boston. They have provided support and continued friendship. While I cannot possibly list every member who has touched my life, I specifically thank Pastors Sean Richmond, and Jeff Bianchi for their spiritual leadership. Thank you also to the past and current members of the sound team. Our efforts together have given me an outlet outside of MIT and allowed me to retain my sanity.

Finally, I would like to express my utmost love and appreciation to my family. I thank my parents, Richard Jr. and Linda Evans and my grandparents Richard Sr. and Ruth Evans. I thank my wife's parents, Bill and Jane Ingram as well. Thank you also to my brothers, Josh and Ryan Evans, and my sister, Krista Evans. Foremost, I thank my wife Julia. Her love and support have been essential to me since before I began my graduate studies. This work is dedicated to her.

Contents

1 Introduction **17**

1.1 Single Molecule Electron Transport 17

1.1.1 Landauer Formula 19

1.2 Schrödinger Equation 21

1.3 Conduction System Definitions 23

1.4 Non-Equilibrium Green's Function Method 25

1.4.1 Scattering Theory and Green's Functions 25

1.4.2 Dyson Equation and Self Energies 27

1.4.3 Calculating Transmission 28

1.5 Real Time Propagation Method 30

1.5.1 Hückel Method Example 34

1.5.2 Advantages and Disadvantages 36

1.6 Thesis Format 38

2 Quantum Chemistry Methods **39**

2.1 Basis Sets 39

2.2 Variational Principle 40

2.3 Electronic Hamiltonian 42

2.3.1 All Electron Hamiltonian 42

2.3.2 Effective Core Potentials 43

2.4 The Hartree-Fock Method 44

2.4.1 Single-determinant Solution Space 44

2.4.2 Fock Equation 45

2.5 Correlated Methods . . . 48
2.6 Density Functional Theory . . . 50
2.6.1 Hohenberg-Kohn Theorems . . . 50
2.6.2 Kohn-Sham Method . . . 52
2.6.3 Spin Density Functional Theory . . . 54
2.6.4 Functionals . . . 55
2.6.5 DFT Inaccuracies . . . 59
2.6.6 Time-Dependent DFT . . . 63
2.7 Pariser-Parr-Pople Model Hamiltonian . . . 64

3 Real Time TDDFT Propagation 67
3.1 TDKS Propagation Theory . . . 67
3.2 Numerical Propagation Methods . . . 69
3.3 Molecular Wire Conductance . . . 71
3.3.1 Average Currents . . . 72
3.3.2 Comparison to Long Wire Results . . . 75
3.3.3 Comparison to NEGF . . . 76
3.3.4 Comparison to Voltage Bias . . . 78
3.4 Conclusions . . . 79
3.5 Acknowledgements . . . 79

4 Spin-Charge Separation in Open-Shell Propagations 81
4.1 Methods . . . 83
4.1.1 Systems . . . 83
4.1.2 Real-Time Density Functional Conductance Simulations . . . 83
4.1.3 Empirical Model Hamiltonians . . . 85
4.2 Results . . . 87
4.2.1 Real-Time TDDFT Currents . . . 87
4.2.2 Obtaining Model Hamiltonian Parameters . . . 89
4.2.3 Model Hamiltonian Currents . . . 91
4.3 Discussion . . . 93

4.4 Conclusions . . . 97
4.5 Acknowledgements . . . 98

5 Importance of Non-local Exchange and Correlation 99
5.1 System and Methods . . . 100
5.2 Real-Time Density Functional Conductance Simulations . . . 103
5.3 Model Hamiltonian Conductance Simulations . . . 107
5.3.1 The PPP Model Hamiltonian . . . 107
5.3.2 Non-local Exchange in the PPP model . . . 108
5.3.3 Correlated Conductance of the PPP model . . . 110
5.4 Conclusions . . . 115
5.5 Acknowledgements . . . 118

6 Dynamic Coulomb Blockade in a Metal-Molecule-Metal Junction 119
6.1 System and Method . . . 120
6.2 Results and Discussion . . . 122
6.3 Conclusions . . . 129

7 Conclusions 131

A Geometry of the Gold-BDT-Gold System 133

List of Figures

1-1 From Ref. [1]. Reprinted with permission from AAAS. Schematic of the experimental system and resulting current and conductance profile for a Gold-BDT-Gold conductance measurement (BDT=benzene-1,4-dithiol). In this experiment, the junction was formed by adsorption of BDT from solution into a self-assembled monolayer in the gap of a fractured gold wire. 18

1-2 Schematic of the conducting molecular contact system. The current is positive when particles travel from the source to the drain, and negative when they travel in the other direction. 19

1-3 I-V calculation results for the Hückel example method. The plots depict (a) $n_D(t) - n_S(t)$ as calculated with the voltage potential method for several potentials (b) $n_D(t) - n_S(t)$ as calculated with the chemical potential method at a potential of 1.2β (only one line is shown for visual clarity), and (c) the resulting I-V curves. 35

2-1 Flow chart depicting the self-consistent field procedure. 48

2-2 Dissociation energy curves of H_2^+ calculated using Hartree-Fock, LDA, and B3LYP. The HF calculation is exact within the basis set (6-311+G**) approximation for this system. 61

2-3 Dissociation energy curves of H_2 calculated using CI, Hartree-Fock, LDA, and B3LYP. CI is exact within the chosen basis set (6-31+G**) for this system. The approximated methods are calculated with a restricted (left) and unrestricted (right) density. 62

3-1 Predictor-corrector routine for the 2^{nd} order Magnus integrator. The order row shows the time order (in dt) to which the matrices in the same column are correct. 70

3-2 (top) Source-wire-drain geometry for *trans*-polyacetylene with lead length of $N = 12$ with the source and drain labeled. With larger N, the source and drain length increase, but the device length remains the same. (mid) Chemical potential under which the initial state is determined for potential V in the chemical potential method. (bottom) Resulting electronic state of the polyacetylene for any time $t < 0$ before the potential is removed at $t = 0$. Red indicates electron accumulation and green indicates electron depletion 71

3-3 (left) Transient current through the central four carbons in $C_{50}H_{52}$ at a series of different initial chemical potentials. The current increases with voltage and includes large, persistent fluctuations. (right) Transient currents smoothed over a time window of width $\Delta t = 0.36$ fs. The currents are now more visible and are converged with respect to time step. The current decays at long times due to partial equilibration of the leads. 73

3-4 Maximum smoothed current through the central four carbons of $C_{50}H_{52}$ (red pluses) and $C_{50}H_{52}$ (green squares) as a function of chemical potential bias. The agreement between these methods demonstrates convergence with respect to lead length. The blue dotted line is a linear fit to the $C_{50}H_{52}$ data and returns a conductance of $\approx 0.85G_0$. 74

3-5 Transient current through the central four carbons in $C_{100}H_{102}$ at a series of different chemical potentials. The current fluctuations persist, but the steady-state current lasts longer indicating only the current "shut-off" is a finite lead effect 75

3-6 Maximum smoothed current through the central four carbons in $C_{50}H_{52}$ as a function of chemical potential bias using real time TDDFT (red solid line) and an NEGF approach described in the text (blue dotted line). The two calculations are nearly identical at low bias and differ somewhat at higher biases due to the lack of self-consistency in the NEGF results. 76

3-7 Maximum smoothed current through the central four carbons in $C_{50}H_{52}$ as a function of chemical potential bias (red solid line) and voltage bias (green dashed line). The results are very similar at low bias. At larger bias (4 V), the finite width of the valence band causes the voltage bias current to drop off. 78

4-1 Plot of I_{tot} and I_{spin} as a function of initial N_{tot} and M_{spin} as determined using B3LYP or HF for the anion (left) and cation (right) case. The value of the fixed initial M_{spin} or N_{tot} is set to 1.0. B3LYP produces more linear current profiles than HF due to a reduction in exact exchange. Likewise, spin current profiles are less linear than charge current profiles because spin is more sensitive to exact exchange. . . . 87

4-2 Dependence of N_{tot} upon V_{tot} with $V_{spin} = 0.272V$ and M_{spin} upon V_{spin} with $V_{tot} = 1.36V$ for the anion (left) and cation (right) as predicted by B3LYP, PPP, and PPP-SIE. The stair-step nature of the N_{tot} and M_{spin} profiles increases with decreasing exact exchange and the spin profiles are more step-like than charge profiles. 90

4-3 Maximum total and spin currents plotted against initial N_{tot} and M_{spin} respectively as calculated by PPP, PPP-SIE, PPP-Hartree, and Hückel propagation for the anion (left) and cation (right). The unvaried initial N_{tot} or M_{spin} is held to 1.0. The model results qualitatively mirror the all-electron results when the fraction of exact exchange is adjusted to reflect the DFT exchange-correlation functionals. 92

4-4 Maximum total and spin currents plotted against initial V_{tot} and V_{spin} respectively as calculated by PPP-SIE, for chains of length 50, 100, and 200 sites. The fixed initial potentials are $V_{spin} = 0.272V$ for the total current plots and $V_{tot} = 1.36V$ for the spin current plots. These calculations indicate the ease with which we can approach the thermodynamic limit in the model system. 94

5-1 Chemical structure representation of the model system and the voltage bias. The saturated linking groups destroy the planar nature of the system, so the full geometry is not shown. 101

5-2 Time dependent charge difference between the drain and source in the model junction. The system begins in the ground state and a bias is applied at time zero. After a transient period of a few hundred attoseconds, a quasi-steady state is achieved. This steady state lasts until the charge in the leads is depleted at around 15 fs. Steady state currents can be obtained from the linear fit slope of $n_D - n_S$ vs. t as illustrated by the broken line. These results are with TD-LDA and a voltage bias of 5.44 V, but similar physics prevails for all methods in this article. 102

5-3 Comparison of the I-V curves obtained using the 6-31G* basis set on the entire system with the I-V curves obtained using a mixed basis set (STO-3G on the leads, 6-31G* elsewhere). 104

5-4 The I-V curves computed with four different methods. The STO-3G basis set is used for the leads and 6-31G* for the rest of the model system. 106

5-5 Current-voltage plots calculated using several all electron (left) and PPP (right) methods. Analogous all electron and PPP method pairs are given the same color and line type. The conductance gap shows the same trend with respect to nonlocal exchange for the PPP and all-electron calculations. 109

5-6 Current-voltage plots calculated using several PPP methods. The non-local correlation present in the GCM calculations results in qualitative changes in the current including a near doubling of the conductance gap. 114

5-7 Time-dependent lead charge difference in TD-GCM and TDHF calculations at a fixed bias of 20 V. The correlated results show persistent oscillations not present in the uncorrelated results. 116

6-1 (a) Au_{114}-BDT-Au_{114} system with source and lead regions labeled along with the effect of lead potential, V, and gate potential, V_g, on electronic energies in each region. Atoms depicted include H (gray), C (light blue), S (green), and Au (gold) (b) Time dependent density difference $(n_D - n_S)$ with linear fitting in the steady state region and (c) resulting current-voltage curve. 121

6-2 TDDFT calculated current-voltage curve using B3LYP, LDA, and Hartree-Fock exchange-correlation functionals. The calculated conductances are 16 μS with LDA, 10 μS with B3LYP, and 0 with HF 123

6-3 Time dependent density difference $(n_D - n_S)$ (a) and device charge (b) as calculated by LDA. The vertical lines indicate approximated times at which the first 0 current regions begin for each potential. The periods of 0 current correspond with more negative charge on BDT. . 125

6-4 I-V plots calculated using both the real time propagation method and the voltage potential version of the NEGF procedure described in section 3.3.3. Both methods produce similar profiles, and there is no systematic difference between the two methods. 127

6-5 TDDFT calculated current as a function of gate voltage with left-right voltage set to 1.09 V and calculated with LDA. The response of current to gate voltage is 5.8 μA/V. 129

Chapter 1

Introduction

1.1 Single Molecule Electron Transport

There has recently been an explosion of interest in quantum scale electronic devices resulting from a number of experiments that demonstrate their unique conductance properties [2, 3, 1, 4, 5, 6, 7, 8, 9, 10, 11, 12, 13, 14, 15, 16, 17, 18, 19, 20, 21, 22, 23, 24, 25, 26, 27]. This interest stems from both practical and theoretical considerations. In terms of practical interest, a large aspect of improving both computational performance and portability is increasing the density of electronic components. Currently, transistors are developed at length scales of tens of nanometers. This is only about two orders of magnitude larger than the scale of single-molecule conductors. If these trends continue, understanding the electronic properties of quantum scale electronics will become necessary.

In terms of theoretical interest, the properties of microscopic conductors are fundamentally different than those of macroscopic conductors. In this work, we focus on resistance. For a conducting macroscopic wire, the resistance is calculated by $\frac{\rho L}{A}$ where A is the cross-sectional area, L is the length, and ρ is a property of the material. The resistance arises from scattering of the electrons by the atomic lattice. The resistance is also potential-independent, so the current through a wire is linear with respect to applied potential according to the well known Ohm's law.

Resistance in a quantum scale (angstrom lengths) device is fundamentally dif-

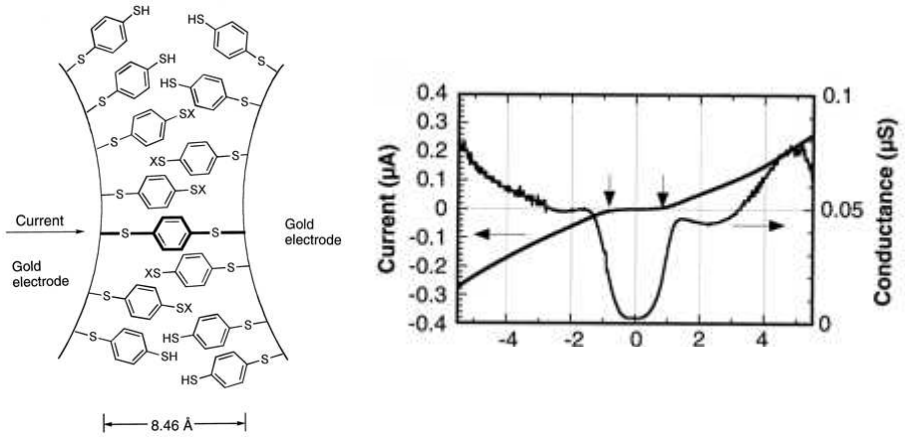

Figure 1-1: From Ref. [1]. Reprinted with permission from AAAS. Schematic of the experimental system and resulting current and conductance profile for a Gold-BDT-Gold conductance measurement (BDT=benzene-1,4-dithiol). In this experiment, the junction was formed by adsorption of BDT from solution into a self-assembled monolayer in the gap of a fractured gold wire.

ferent from macroscopic resistance. In this thesis, we will examine devices that are several angstroms in length. This is less than the typical mean free path of metallic electrons which is on the order of tens of angstroms [28], so we would expect these devices to demonstrate a ballistic transport behavior. Using purely an electron scattering picture of resistance, conducting devices which are too small to scatter electrons should demonstrate essentially no resistance. Single molecule devices have demonstrated measured resistances [1, 16, 23], and even point contacts with effectively perfect lead-device contact show low voltage resistances corresponding to the quantum conductance unit ($G_0 = \frac{2e^2}{h}$) [29, 30, 31, 32]. Furthermore, these experiments reveal conductances that are not independent of applied potential, but instead show a staircase-like dependence of conductance on potential. Point contact experiments reveal step sizes of G_0. A schematic of an experimental system and resulting stair-step conductance for an example single-molecule conductance measurement (Ref. [1] are shown in Fig. 1-1.

Beyond the ballistic conduction behavior and stair-step conductance profile, quantum scale conductors display other unexpected behaviors. For example, the impact of band-lineup on conduction can cause current to actually decrease with an increase

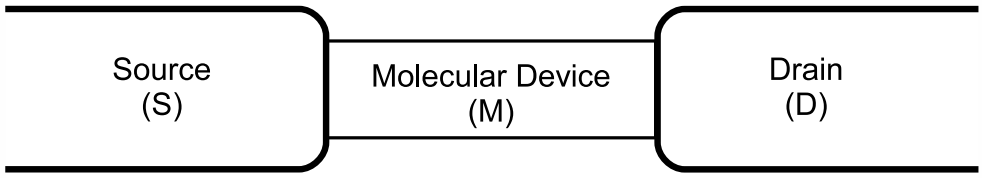

Figure 1-2: Schematic of the conducting molecular contact system. The current is positive when particles travel from the source to the drain, and negative when they travel in the other direction.

in potential producing negative differential resistance [15, 20, 33, 34]. Current has been known to drive dynamics [21, 24, 35], although nuclear motion is outside of the scope of this work. In chapter 4, we will see that open-shell modeling suggests that the up and down spin electrons cooperatively produce spin and charge quasiparticles that travel at different rates [36, 37, 38, 39, 40, 41, 42, 43, 44, 45, 46, 47, 48]. Finally, in chapter 6, we will consider the effects of coulomb blockade [1, 49, 11, 34, 18] in which current is reduced by the energetic cost of charging the quantum conductor in the course of charge transport. Clearly, electronic properties such a resistance arise from a different source and show different behaviors in single molecule devices than in macroscopic devices.

1.1.1 Landauer Formula

The interesting behavior of molecular size conductors was first explained with a new picture of resistance by Landauer [50, 51], and later expanded by Büttiker [52, 53, 54]. We consider the system depicted in Fig. 1-2. At zero temperature, the states in the source are filled according to $f_S(E) = \Theta(\mu_S - E)$, and the drain states are filled according to $f_D(E) = \Theta(\mu_D - E)$. $\Theta(E)$ is the step function in energy, and the parameters μ_S and μ_D are the chemical potentials in the leads. If we are concerned with finite temperatures, we simply replace the step function lead distributions with Fermi functions. For the purposes of the Landauer formula, we initially assume that the contacts are reflectionless. This is not generally the case for molecular devices, but is closely approximated in the case of point contacts. By reflectionless, we mean

that all current carrying states in the device will transmit 100% into the drain. The contact cannot be reflectionless in the other direction because the wires have many more current carrying states than can be accommodated by the device.

Assuming the device is one-dimensional, the current is carried by the momentum states $\psi(k) = e^{ikt}$. If we take into account double filling, the current carried by the state $\psi(k)$ is

$$I_k = \frac{2e}{L}\frac{\hbar k}{m_e} = \frac{2e}{\hbar L}\frac{\partial E_k}{\partial k}, \tag{1.1}$$

where e and m_e are the electronic charge and mass, and L is the length of the device. The right (+) moving states ($k > 0$) are filled by the source and thus filled according to $f_S(E)$. Similarly, the left (-) moving states ($k < 0$) are filled according to $f_D(E)$. As a result, the total current of the one-dimensional conductor with reflectionless contacts is

$$\begin{aligned} I_{1D} &= \frac{2e}{\hbar L}\left(\sum_{k>0}\frac{\partial E_k}{\partial k}\left[\Theta(\mu_S - E_k) - \Theta(\mu_D - E_k)\right]\right) \\ &= \frac{2e}{\hbar L}\left(\frac{L}{2\pi}\int_0^\infty dk\frac{\partial E_k}{\partial k}\left[\Theta(\mu_S - E_k) - \Theta(\mu_D - E_k)\right]\right) \\ &= \frac{2e}{h}\left[\max(\mu_S, E_{k=0}) - \max(\mu_D, E_{k=0})\right]. \end{aligned} \tag{1.2}$$

The multiple of $\frac{L}{2\pi}$ when switching to an integral arises from the need to renormalize to the proper state density when assuming periodic boundary conditions for the device. This result clarifies the source of resistance in ballistic transport. It arises from the limited number of current carrying states in the restricted space of the device. Also, if we consider that $V = \frac{\mu_S - \mu_D}{e}$, we see that the resulting conductance is the conductance quantum. Finally, we note the use of the terms $\max(\mu_{S(D)}, E_{k=0})$. These terms are included to recognize that there is no guarantee that the source or drain chemical potentials are large enough to fill any of the current carrying states on the molecule. If, for example, the device includes a very large potential barrier, no current will flow.

There are a few additional considerations to complete our derivation of the Landauer formula. First, we consider the possibility that the leads are not reflectionless. In the Landauer formula, this is incorporated by a factor of T, the probability that

an electron in the device will transmit to the lead. The other consideration is to remove our 1D conductor requirement. The additional dimensions require us to include additional quantum numbers into our current carrying state definition. As a result, there are multiple states corresponding to each value of k. Each set of possible quantum numbers, independent of k, represents a different *channel* through which to conduct current with conductance given in equation 1.2. Each channel will activate at a different source potential. Including these factors, the Landauer equation for the device conductance is

$$G_C = \frac{2e^2}{h} T M(V), \tag{1.3}$$

where $M(V)$ counts the number of conductance channels that are activated at the potential V. This term is responsible for the steps in the conductance profile. We note that so far T and M are just phenomenological parameters. We will combine them as just one energy dependent transmission function, $T(E)$, that tells how an electron in the source at energy E is transferred to the drain. We will explore the commonly used method to calculate this transmission function in section 1.4.

1.2 Schrödinger Equation

In this work, we will model quantum scale conductance at the level of nonrelativistic quantum mechanics. Thus, we are concerned with systems described by the Schrödinger equation. In atomic units, the Schrödinger equation is

$$i\frac{\partial}{\partial t}\Psi(\mathbf{r},t) = \hat{H}(t)\Psi(\mathbf{r},t), \tag{1.4}$$

where $\hat{H}$ is the *Hamiltonian* or linear energy operator. $\Psi(\mathbf{r},t)$ is the wavefunction describing the system, a complex valued function of the same spatial ($\mathbf{r}$) and temporal (t) degrees of freedom as the system. The probability distribution describing a measurement of the degrees of freedom of the system is given by $P(\mathbf{r},t) = |\Psi(\mathbf{r},t)|^2 = \Psi^*(\mathbf{r},t)\Psi(\mathbf{r},t)$, so the wavefunction is normalized according to $\int d\mathbf{r}\, |\Psi(\mathbf{r},t)|^2 = 1$. The stationary states of the system, those which vary with time only in the overall

phase, are the eigenfunction of the Hamiltonian. This yields the time-independent Schrödinger equation,

$$\hat{H}\Psi(\mathbf{r}) = E\Psi(\mathbf{r}). \tag{1.5}$$

This eigenvalue equation describes time-independent phenomena in nonrelativistic quantum mechanics.

Equation 1.4 gives us a method to determine the time evolution of a wavefunction. We express this time-evolution in terms of the propagation operator $\hat{U}(t, t_0)$ defined by

$$\Psi(t) = \hat{U}(t, t_0)\,\Psi(t_0)\,. \tag{1.6}$$

By integration, we find that

$$\hat{U}(t, t_0) = \hat{T}exp\left\{-i\int_{t_0}^{t} dt'\hat{H}(t')\right\}, \tag{1.7}$$

where $\hat{T}$ is the time ordering operator which dictates the proper expansion for the exponential operator. In the case that $\hat{H}$ is time-independent, or the propagation interval is sufficiently small so that we can consider $\hat{H}$ to be effectively time-independent, the propagator simplifies to

$$\hat{U}(t, t_0) = e^{-i\hat{H}(t-t_0)}. \tag{1.8}$$

In quantum mechanics, measurable quantities are described by linear operators. For example, the energy is described by the linear operator $\hat{H}$. Therefore, we will describe the wavefunction as a linear combination of basis functions:

$$\Psi(\mathbf{r}, t) = \sum_i c_i(t)\Phi(\mathbf{r}). \tag{1.9}$$

We will discuss the specific basis functions we use for quantum chemistry calculations in section 2.1, and here simply state that we use basis functions that are localized with each centered on one of the atoms in our system. The establishment of a basis allows us to describe the wavefunction by a vector of the expansion coefficients c_i,

and each linear operator by a matrix. In Dirac notation, the wavefunction $\Psi(\mathbf{r},t)$ is described by the ket vector $|\Psi(t)\rangle$, and its complex conjugate $\Psi^*(\mathbf{r},t)$ by the bra vector $\langle\Psi(t)|$. The elements of the operator $\hat{A}$ are given by

$$A_{ij} = \langle i|\hat{A}|j\rangle = \int d\mathbf{r}\Phi^*(\mathbf{r})\hat{A}\Phi(\mathbf{r}). \tag{1.10}$$

Throughout this work, we will alternatively use Dirac notation and integral notation as appropriate to the problem.

1.3 Conduction System Definitions

We will now establish some definitions to help us in discussing current carrying systems. A schematic of the systems under examination is shown in Fig. 1-2. As shown in Fig. 1-2, we divide the system into three parts, the source (S) and drain (D) metallic wires, and the molecular device (M). The same system division is common to most single-molecule conduction studies [55, 56, 57, 58, 59, 60]. We will call electrons moving from the source to the drain positive current, and electrons moving in the other direction negative current.

Each atom belongs to one of the three regions, and each basis function is associated with an atom. Therefore, we can also divide the matrix representation of any one-particle system operator analogously. For example, a one-particle Hamiltonian-like operator becomes

$$\hat{H} = \begin{bmatrix} \hat{H}_S & \hat{V}_{SM} & \hat{V}_{SD} \\ \hat{V}_{SM}^\dagger & \hat{H}_M & \hat{V}_{MD} \\ \hat{V}_{SD}^\dagger & \hat{V}_{MD}^\dagger & \hat{H}_D \end{bmatrix}. \tag{1.11}$$

Because each sub-operator in equation 1.11 is formed by selecting a subset of the complete basis, the division is basis-set dependent. For the purposes of associating an electron population to each region, it will be helpful if there is no overlap between regions. We accomplish this by performing the separation in an orthogonalized basis.

We choose the Löwdin symmetrically orthogonalized basis [61, 62] which is given by

$$\tilde{\phi}_i = \sum_j \left(S^{-1/2}\right)_{ij} \phi_j, \tag{1.12}$$

where $\mathbf{S}$ is the overlap matrix with elements defined by

$$S_{ij} = \langle \phi_i | \phi_j \rangle. \tag{1.13}$$

This basis has the benefit among all possible orthogonalized bases of most closely resembling the original basis (ϕ_i) in the sense that $\sum_i \int d\mathbf{r} \left|\tilde{\phi}_i(\mathbf{r}) - \phi_i(\mathbf{r})\right|^2$ is minimized. Thus, we can maintain the same association between basis function and atom when we orthogonalize the basis.

To divide a single-particle operator into Löwdin orthogonalized pieces as in equation 1.11, we first change the basis of the operator matrix:

$$\tilde{\mathbf{H}} = \mathbf{S^{-1/2} H S^{-1/2}}. \tag{1.14}$$

Then we separate the matrix as in equation 1.11. If necessary, we can transform back to our original basis by left and right multiplying by $\mathbf{S^{1/2}}$, but we lose the advantage of the reduced size of the matrix parts.

We will also use the Löwdin basis to define a population operator. The operator to calculate the Löwdin population on the region $\mathbf{R}$ of the system is

$$\hat{n}_R = \sum_{i \in R} |\tilde{\phi}_i\rangle\langle\tilde{\phi}_i|. \tag{1.15}$$

Unless otherwise noted, populations in this work are calculated according to this definition.

1.4 Non-Equilibrium Green's Function Method

1.4.1 Scattering Theory and Green's Functions

Calculating conductance involves predicting the outgoing density as a function of incoming density. Therefore, scattering theory [59, 63] is a natural framework under which to describe conductance. By far, the most common framework used to calculate conductance is the non-equilibrium Green's function (NEGF) method [64, 65, 66, 67, 68, 56] which derives from scattering theory. Scattering theory focuses on the problem of an incoming state which interacts in a small space with a scattering potential to produce an outgoing state. The incoming and outgoing states are described in regions far from the scattering region in which they no longer feel the scattering interaction. Thus it is useful to describe them in terms of free particle states. We will choose an incoming state that is an eigenfunction of the potential free Hamiltonian $\hat{H}_0$ and find the steady state according to the full Hamiltonian $\hat{H}_0 + \hat{V}$. Rearranging the time-dependent Schrödinger equation and assuming a time-independent Hamiltonian, we get the nonhomogeneous differential equation

$$\left(i\frac{\partial}{\partial t} - \hat{H}_0\right)|\Psi(t)\rangle = \hat{V}|\Psi(t)\rangle. \tag{1.16}$$

Using the Green's function method, the solution to 1.16 is

$$|\Psi(t)\rangle = |\Phi(t)\rangle + \int_{-\infty}^{\infty} dt' \hat{G}_0(t,t')\hat{V}|\Psi(t')\rangle, \tag{1.17}$$

where

$$\left(i\frac{\partial}{\partial t} - \hat{H}_0\right)\hat{G}_0(t,t') = \delta(t-t'). \tag{1.18}$$

$|\Phi(t)\rangle$ can be any function for which $\left(i\frac{\partial}{\partial t} - \hat{H}_0\right)|\Psi(t)\rangle = 0$. Although $\hat{G}_0(t,t')$ can vary depending on boundary conditions, we choose the *retarded* Green's operator,

$$\hat{G}_0^R(t,t') = -i\Theta(t-t')e^{-i\hat{H}_0(t-t')}, \tag{1.19}$$

which corresponds to the wave at time t depending only on the wave at $t' < t$. Assuming a stationary state solution, so $|\Psi(t')\rangle = e^{-iE(t'-t)}|\Psi(t)\rangle$, we evaluate the integral by introducing an adiabatic turn-on ($\hat{V} \to \lim_{\eta\to 0^+} \hat{V}e^{(t'-t)\eta}$). The result is the Lippmann-Schwinger equation

$$\begin{aligned} |\Psi\rangle &= |\Phi\rangle + \hat{G}_0^R(E)\hat{V}|\Psi\rangle, \\ \hat{G}_0^R(E) &= \lim_{\eta\to 0^+} \left(E - \hat{H}_0 + i\eta\right)^{-1}. \end{aligned} \tag{1.20}$$

Clearly, $|\Phi\rangle$ must be the incoming wave, because we require $|\Psi\rangle \to |\Phi\rangle$ as $V \to 0$. We make special note of $\hat{G}_0^R(E)$, the retarded, energy-space, Green's operator because it is a very important operator in both scattering theory and conductance calculations. $\hat{G}_0^R(E)$ amplifies the eigenvectors of $\hat{H}_0$ with energy E. If we had chosen instead the *advanced* boundary condition for the time-dependent Green's operator,

$$\hat{G}_0^A(t,t') = i\Theta(t'-t)e^{-i\hat{H}_0(t-t')}, \tag{1.21}$$

we would have found the advanced energy space Green's operator

$$\hat{G}_0^A(E) = \lim_{\eta\to 0^+} \left(E - \hat{H}_0 - i\eta\right)^{-1}. \tag{1.22}$$

We can extend our definition of the Green's function to arbitrary Hamiltonian $\hat{H}$ so

$$\hat{G}^{R(A)}(E) = \lim_{\eta\to 0^+} \left(E - \hat{H} + (-)i\eta\right)^{-1}. \tag{1.23}$$

We will note one more property of the Green's operators that is useful in calculating conductance. We define the operator

$$\begin{aligned} \hat{\rho}(E) &= \frac{G^A(E) - G^R(E)}{2\pi i} \\ &= \lim_{\eta\to 0^+} \frac{\eta}{\pi} \sum_j \frac{|\psi_j\rangle\langle\psi_j|}{(E-E_j)^2 + \eta^2}, \end{aligned} \tag{1.24}$$

where the $|\psi_j\rangle$ are the eigenkets of $\hat{H}$. Recognizing the Cauchy representation of

$\delta(E-E_j)$, we see that $\hat{\rho}(E)$, the spectral operator, extracts from $|\phi\rangle$, the components corresponding to eigenvectors of $\hat{H}$ with eigenvalue E.

1.4.2 Dyson Equation and Self Energies

The Green's operator contains all of the same information as the full Hamiltonian operator. Therefore, like the Hamiltonian, calculating the exact Green's operator can be computationally intractable. However, it may be possible to calculate the Green's function for some related Hamiltonian. We will break our Hamiltonian into a zeroth order Hamiltonian and a perturbing coupling term. Therefore, $\hat{H} = \hat{H}_0 + \hat{V}$, and we can determine the Green's operators, $\hat{G}^{R(A)}(E)$ and $\hat{G}_0^{R(A)}(E)$, corresponding to $\hat{H}$ and $\hat{H}_0$ respectively. Using the Green's operator definition in equation 1.23, it is trivial to verify the Dyson equation,

$$\hat{G}^{R(A)}(E) = \hat{G}_0^{R(A)}(E) + \hat{G}_0^{R(A)}(E)\hat{V}\hat{G}^{R(A)}(E) = \hat{G}_0^{R(A)}(E) + \hat{G}^{R(A)}(E)\hat{V}\hat{G}_0^{R(A)}(E). \tag{1.25}$$

This equation is clearly related to equation 1.20.

In the NEGF formalism, we use the Dyson equation to determine the molecule-molecule Green's operator without evaluating the full matrix Green's function. To do so, we will use the concept of a self energy, a modification to the Hamiltonian used to include additional interactions that are not included in the Hamiltonian. Consider the Hamiltonian of a system divided into two subspaces, A and B. If we consider our unperturbed Hamiltonian to describe A and B in isolation,

$$\begin{aligned} \hat{H}_0 &= \begin{pmatrix} \hat{H}_A & 0 \\ 0 & \hat{H}_B \end{pmatrix}, \\ \hat{V} &= \begin{pmatrix} 0 & \hat{V}_{AB} \\ \hat{V}_{BA} & 0 \end{pmatrix}. \end{aligned} \tag{1.26}$$

From the Dyson equation, we can show that the Green's operator on the space of A

is

$$\begin{aligned}\hat{G}_A^{R(A)}(E) &= \lim_{\eta\to 0^+}\left(E - \hat{H}_A - \hat{\Sigma}_B^{R(A)}(E) + (-)i\eta\right)^{-1}, \\ \hat{\Sigma}_B^{R(A)}(E) &= \hat{V}_{AB}\hat{G}_{0B}^{R(A)}(E)\hat{V}_{BA}.\end{aligned} \tag{1.27}$$

We call $\hat{\Sigma}_B^{R(A)}(E)$ the retarded (advanced) self energy of subspace B. Using the system separation in section 1.3, we will include the lead effects as self energies in the device Green's functions.

1.4.3 Calculating Transmission

With the results from sections 1.4.1 and 1.4.2 in place, we can now derive the NEGF current formula. We will stick to a noninteracting particle description for simplicity and because it is most commonly used. However, the method can be expanded to include electron interactions within the device region [64]. We are solving for conductance within in the system described in section 1.3 with the single-particle Hamiltonian

$$\hat{H} = \begin{bmatrix} \hat{H}_S & \hat{V}_{SM} & 0 \\ \hat{V}_{SM}^\dagger & \hat{H}_M & \hat{V}_{MD} \\ 0 & \hat{V}_{MD}^\dagger & \hat{H}_D \end{bmatrix}. \tag{1.28}$$

This Hamiltonian is identical to that given in equation 1.11 except $\hat{V}_{SD} = \hat{V}_{SD}^\dagger = 0$. There is no direct source-drain coupling, and all current must flow through the device. In the NEGF method, the device region typically includes some metal atoms so that some lead effects are included in the device Hamiltonian. This will be necessary, because the current formula acts entirely within the device space. We refer to the block diagonal portions ($\hat{H}_S$, $\hat{H}_M$, and $\hat{H}_D$) as $\hat{H}_0$ and the coupling blocks as $\hat{V}$.

According to the scattering model, the lead states defined by the spectral operators, $\hat{\rho}_{0S}(E)$ and $\hat{\rho}_{0D}(E)$, are filled according to the Fermi functions $f_{S(D)}(E)$ deep inside the leads. The device conducting states are determined according to the

Lippmann-Schwinger equation here used in a different form,

$$|\psi\rangle = |\phi\rangle + \hat{G}^A \hat{V}|\phi\rangle, \tag{1.29}$$

where $|\psi\rangle$ is an eigenfunction of $\hat{H}$ and $|\phi\rangle$ is an eigenfunction of $\hat{H}_0$. We will first calculate the current due to states originating in the source.

We use a current operator defined according to the change in particle number in the drain,

$$\hat{I} = \frac{e}{\hbar}\frac{d\hat{N}_D}{dt} = \frac{ie}{\hbar}\left(\hat{P}_D\hat{V} - \hat{V}\hat{P}_D\right). \tag{1.30}$$

Using the commutator with respect to $\hat{V}$ only makes it explicit that the block diagonal pieces yield 0 commutator.

We want to calculate the differential current for all of the source originating states $|\psi_i^S\rangle$. Using the source spectral function and equation 1.29 and taking into account double filling, the differential current is

$$dI_S(E) = dE\frac{2ie}{\hbar}Tr\left[\left(1 + \hat{G}^A(E)\hat{V}\right)\hat{\rho}_S(E)\left(\hat{V}\hat{G}^R(E) + 1\right)\left(\hat{P}_D\hat{V} - \hat{V}\hat{P}_D\right)\right] f_S(E). \tag{1.31}$$

Using the Dyson equation, and taking into account that $\hat{V}$ must always couple the device and one lead, we reorganize the expression into the standard NEGF form

$$\begin{aligned} dI_S(E) &= \frac{2e}{h}Tr\left[\hat{\Gamma}_S(E)\hat{G}^R_M(E)\hat{\Gamma}_D(E)\hat{G}^A_M(E)\right] f_S(E), \\ \hat{\Gamma}_{S(D)}(E) &= \hat{V}_{MS(D)}\hat{\rho}_{S(D)}(E)\hat{V}^\dagger_{MS(D)}. \end{aligned} \tag{1.32}$$

Note that all of the operators in equation 1.32 are in the molecule subspace. We calculate the molecular device Green's function $\hat{G}^{R(A)}_M(E)$ using the self energy expression, equation 1.27:

$$\begin{aligned} \hat{G}^{R(A)}_M(E) &= \lim_{\eta\to 0^+}\left(E - \hat{H}_M - \hat{\Sigma}^{R(A)}_S - \hat{\Sigma}^{R(A)}_D - (+)i\eta\right)^{-1}, \\ \hat{\Sigma}^{R(A)}_{S(D)} &= \hat{V}_{MS(D)}\hat{G}^{R(A)}_{0S(D)}\hat{V}^\dagger_{MS(D)}. \end{aligned} \tag{1.33}$$

Analogously, we can calculate the differential current from states originating in

the drain. We get the same expression as 1.32 except the sign is reversed and the Fermi function refers to the drain. The resulting calculated current is

$$I = \frac{2e}{h}\int_{-\infty}^{\infty} dETr\left[\hat{\Gamma}_S(E)\hat{G}_M^R(E)\hat{\Gamma}_D(E)\hat{G}_M^A(E)\right](f_S(E) - f_D(E)). \tag{1.34}$$

By comparison to the Landauer formula, the NEGF method produces an energy dependent transmission function

$$T(E) = Tr\left[\hat{\Gamma}_S(E)\hat{G}_M^R(E)\hat{\Gamma}_D(E)\hat{G}_M^A(E)\right]. \tag{1.35}$$

To end this section, we will comment on the Hamiltonian used in the NEGF method. The NEGF method as presented here can be used with any single-particle Hamiltonian-like operator. In fact, even though the method described here does not include interaction, the Hamiltonian can be derived from a quantum chemistry method that includes interaction. Common approximations for NEGF include semi-empirical [69, 70], *ab initio* [71], DFT [72, 73, 55, 74, 75, 76, 77, 78], and model Hamiltonian [79, 80, 81] methods. Formally, an exact one-particle molecular Green's Function can be developed by including interactions as a self-energy term [82, 59]. Practically, improvements on the single particle method described here can be achieved by generating the Green's operator from the conducting steady state and solving self consistently [59, 57].

1.5 Real Time Propagation Method

While NEGF is the dominant conduction method, the focus of this dissertation is the calculation of quantum scale currents using a real time microcanonical approach. For this section, we assume that we can determine the time-dependent wavefunction $|\Psi(t)\rangle$ of a molecular system including the addition of a one particle potential. We will examine in more detail in chapter 3 a method to determine $|\Psi(t)\rangle$ in interacting electron quantum calculation, and here will just take the ability to calculate $|\Psi(t)\rangle$ as given. In section 1.5.1, we will give an example using the Hückel method in which

propagating a wavefunction is trivial.

The essence of the real time propagation method is the following: We prepare an initial state by determining the ground state under one Hamiltonian, and at time $t = 0$, switch to a different Hamiltonian. Based on the electronic behavior, we determine the transport properties of the device. The initial and final Hamiltonian differ in the addition or removal of a one particle potential operator to the lead Hamiltonians. For some of the early calculations, we switched from one Hamiltonian to the other slowly, but found that such "adiabatic" switching did not significantly change our current-voltage results.

We generally use one of two potential definitions to determine the initial and propagation Hamiltonians. In the *chemical potential* method, we solve for an initial state under the Hamiltonian $\hat{H} - \frac{V}{2}\hat{n}_S + \frac{V}{2}\hat{n}_D$ where $\hat{H}$ is the unperturbed Hamiltonian, and V is the external potential. The operators $\hat{n}_S$ and $\hat{n}_D$ are defined by equation 1.15. The additional operator, $-\frac{V}{2}\hat{n}_S + \frac{V}{2}\hat{n}_D$ increases the electronic density on the source relative to the drain. The system is then propagated under $\hat{H}$ allowing the state to evolve towards equilibrium. This definition resembles the definition in the NEGF and Landauer methods in that the potential is defined in terms of differential filling. The chemical potential method is analogous to the NEGF case in which $\mu_S = \mu_M + \frac{V}{2}$, and $\mu_D = \mu_M - \frac{V}{2}$.

The *voltage* method is the complement to the chemical potential method. In the voltage method, the initial state is determined under the unperturbed Hamiltonian $\hat{H}$, and then propagated under $\hat{H} + \frac{V}{2}\hat{n}_S - \frac{V}{2}\hat{n}_D$. The system starts in equilibrium and is pushed out by the potential that raises the orbital energy in the source and decreases energy in the drain. The analogous NEGF formalism would set

$$T(E) = Tr\left[\hat{\Gamma}_S(E + \frac{V}{2})\hat{G}^R_M(E)\hat{\Gamma}_D(E - \frac{V}{2})\hat{G}^A_M(E)\right], \tag{1.36}$$

where the difference in lead potential comes from a shift in the energies of already filled levels [68].

We note that the spatial voltage profile defined via the Löwdin populations is not

obvious. Other voltage definitions have been considered including step-like potentials [74, 83], ramp potentials [72, 84], and potentials in terms of localized orbitals [55, 75, 77, 78]. All of these methods give qualitatively similar I-V results. A detailed examination of the results of various voltage profiles may prove interesting, but is not pursued in this work. The Löwdin profile is appropriate for our work because it has previously been shown in our group to give consistent treatment of charge transfer[85, 86] and spin states[87].

Reflecting equation 1.30, the current is determined by the changing electronic populations on the system portions defined in section 1.3. Using a population operator such as that in equation 1.15, we define time dependent regional populations

$$n_R(t) = \langle \Psi(t) | \hat{n}_R | \Psi(t) \rangle. \tag{1.37}$$

Thus we calculate the time dependent populations in the source ($n_S(t)$), molecular device ($n_M(t)$), and drain ($n_D(t)$).

We can use these populations to calculate the current. Consider an experiment in which our leads are connected to infinitely large electron reservoirs via reflectionless contacts. We can define the current in terms of changing populations in the reservoirs. We define the current out of the source as

$$I_S = -\frac{dn_S(t)}{dt}. \tag{1.38}$$

Similarly, the current into the drain is

$$I_D = \frac{dn_D(t)}{dt}. \tag{1.39}$$

Although these values would be equal in a true steady state, they are not exactly equal in our numeric calculations. Because we have no reason to choose one or the other lead to determine current, we choose the average of the two. Therefore,

$$I_S = \frac{1}{2}\frac{d\left(n_D(t) - n_S(t)\right)}{dt}. \tag{1.40}$$

In general, we calculate the current smoothed over a time period significantly larger than the time-step of the simulation. This reflects the typically larger time used to make a measurement and prevents rapid oscillations in the calculated current. Although the limits of quantum chemistry methods require us to approximate this experiment with finite reservoirs, we use equation 1.40 to calculate transient currents.

There are several different ways for us to choose a single current value for each propagation. In the projects presented in this work, we have variously chosen:

1. the maximum current within a specified approximately steady-state time period.

2. the average current over that time period.

3. the current calculated from the slope of the linear least-squares fit to $n_D(t) - n_S(t)$ over that same time period.

In the case of a perfect steady state, all three methods give exactly the same result. Each of the three methods has advantages. Method 1 accounts for the fact that different voltages may require different amounts of time to overcome inertia, and experience finite system effects at different times while method 2 keeps current measurement times consistent across all propagations. Method 3 is generally chosen over 2 because it shows less sensitivity to the endpoints of the measurement period.

Finally, we make a note about open shell systems. Through this section, we have focused exclusively on total charge current and will demonstrate our method with a closed-shell example. However, this method is trivially generalizable to open shell examples, in which we see conduction of not only charge, but spin as well. We will explore open shell conduction in more detail in chapter 4 when we compare the relative transport properties of spin and charge quasiparticles.

1.5.1 Hückel Method Example

As an example, we will calculate the I-V curve of a closed shell Hückel chain of 104 sites. The unperturbed one-particle Hamiltonian is

$$\hat{H} = -\sum_{j=1}^{103} \beta_{j,j+1} \left(c_j^\dagger c_{j+1} + c_{j+1}^\dagger c_j \right), \tag{1.41}$$

where $\beta_{j,j+1}$ is the hopping parameter between the jth and $(j+1)$th site. The first 50 sites are the source while the last 50 are the drain, leaving a molecular device of 4 sites. The hopping parameter is β for adjacent sites within the leads or device, and 0.1β between the leads and device. Energies are in units of β, while times are in units of $1/\beta$. We will solve for the system containing $N_e = 104$ electrons (52 up and 52 down spin). The unperturbed Hamiltonian in equation 1.41 is used to propagate in the chemical potential definition and to determine the initial state in the voltage potential method. To construct the perturbed Hamiltonian and calculate densities, we use the number operators

$$\hat{n}_R = \sum_{j \in R} c_j^\dagger c_j. \tag{1.42}$$

Because the electrons in the Hückel method do not interact, the ground state and propagation calculations are much simpler than those described in chapters 2 and 3. The many electron ground state ($t = 0$) in the closed shell Hückel method is determined by diagonalizing the one-particle Hamiltonian and doubly filling the $N_e/2$ lowest energy eigenvectors. Because the electrons do not interact, the single particle Hamiltonian is time independent, and each electron is propagated according to

$$|\psi(t)\rangle = e^{-i\hat{H}t} |\psi(0)\rangle. \tag{1.43}$$

Time dependent values of $n_D(t) - n_S(t)$ are shown in Fig. 1-3a (voltage bias) and 1-3b (chemical potential bias). We determine the currents for use in the I-V curve by linear fitting in the time period of 5.0 to 35.0 time units. In chapter 3 we will examine our method of choosing the steady state period in more detail. The linear

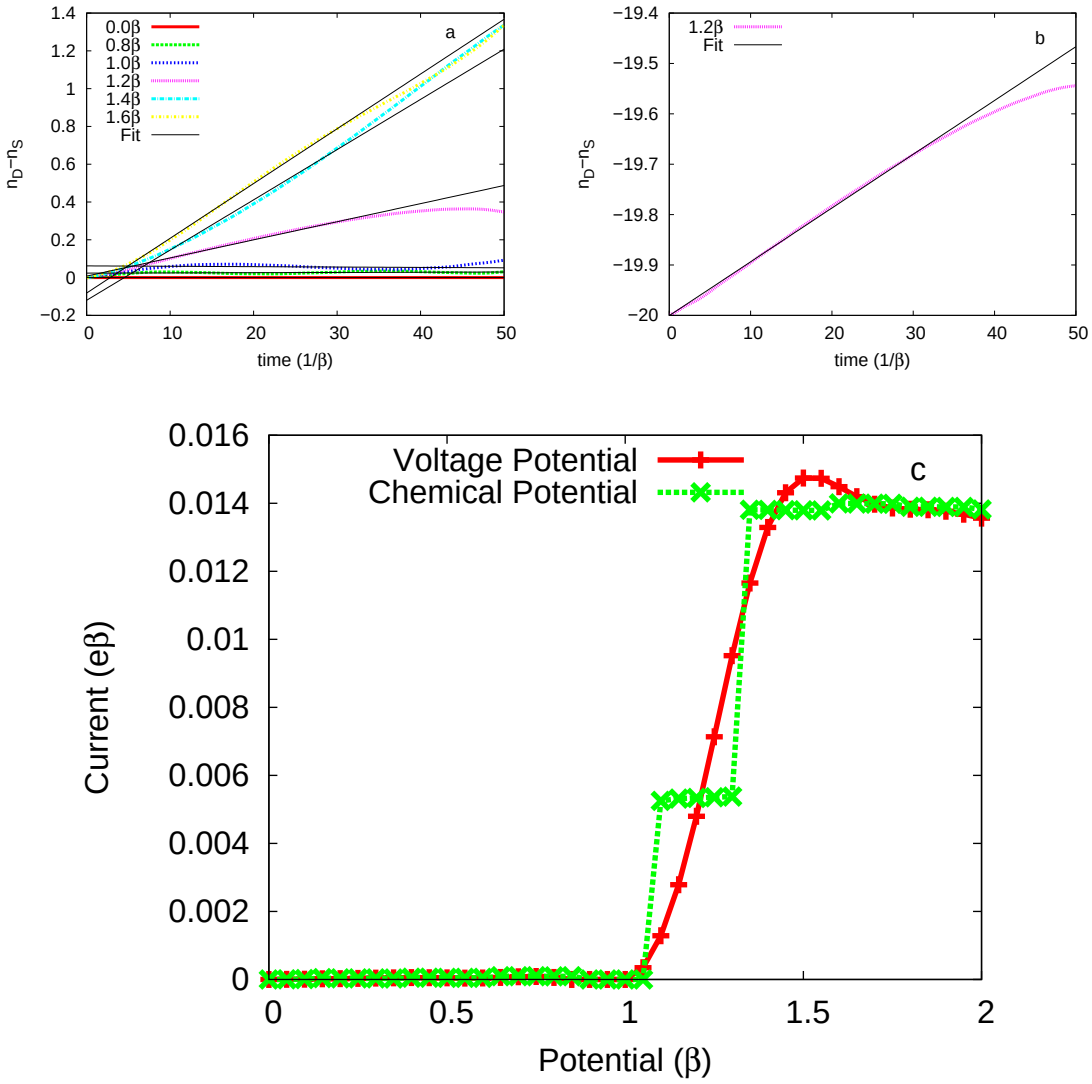

Figure 1-3: I-V calculation results for the Hückel example method. The plots depict (a) $n_D(t) - n_S(t)$ as calculated with the voltage potential method for several potentials (b) $n_D(t) - n_S(t)$ as calculated with the chemical potential method at a potential of 1.2β (only one line is shown for visual clarity), and (c) the resulting I-V curves.

fit lines are included in Fig. 1-3a and b. The resulting I-V curves are shown in Fig. 1-3c.

These I-V curves include several general characteristics of curves that we calculate in the real time method. We notice the lack of conductance until a potential of about 0.5β. This conductance gap results from insufficient potential to overcome the bad gap in the molecular device. The conductance gap decreases with stronger lead-device coupling as the device states are broadened.

The voltage potential and chemical potential demonstrate similar conductance [88], especially at low voltage, but include some differences and model slightly different situations. The most clear difference is the hard step-like nature of the chemical potential method. This results from the tendency of the initial state potential to move whole electrons from the drain to the source. Increasing the lead size creates more, but smaller, steps indicating that at the thermodynamic limit, these current steps will vanish. Also, only the voltage potential method will demonstrate negative differential conductance as the bias changes the alignment of lead and device states during propagation. Finally, at biases too large to properly be described in a finite system, the two methods will show different behavior. The voltage potential will have zero current as there is no alignment between lead and device states within the finite bias creating three essentially uncoupled regions. On the other hand, the chemical potential definition will reach a maximum saturated current because there will be no more electrons to transfer for the initial state. We must be aware of these differences and sources of error when interpreting our real time conduction results.

1.5.2 Advantages and Disadvantages

It is useful to examine the advantages and disadvantages of the real time propagation method relative to the more common NEGF method. The primary disadvantage of the real time propagation technique is computational cost. For the polyacetylene wires that we will study in chapters 3, 4, and 5, a single voltage point may require one or two days of wall-time to propagate on a single processor. The NEGF method can calculate an entire I-V curve in a few hours. Also, the real time propagations

are restricted to finite, closed systems, so the long time dynamics do not reflect the behavior of a real system with *de facto* infinite leads and electron reservoirs.

On the other hand, the real time method includes several advantages, especially when used in conjunction with density functional theory (DFT). Both the NEGF/DFT and time-dependent density functional theory (TDDFT) make use of the Kohn-Sham single-particle Hamiltonian, which we will discuss in chapter 2. While the use of the single-particle Hamiltonian in TDDFT is theoretically well supported, its use in NEGF/DFT is an uncontrolled assumption. Indeed, if the steady state assumption is not accurate, the single-particle operator is time-dependent and the Lippmann-Schwinger equation (1.20) on which NEGF is based is not true. This is not a problem in the real time method, because the single-particle Hamiltonian can vary with the density.

The other advantage that the real time definition has is that it does not require an uncontrolled approximation of the potential when using DFT. In the Landauer picture, the potential is simply the difference between the chemical potentials of the two non-interacting electron reservoirs. Most modern techniques similarly define the potential in terms of the difference in Fermi energies between left- and right-moving electrons [67, 69, 89, 90, 91] or between electrons deep inside each lead [72, 73, 55, 74, 75, 76, 77, 78]. While this is not a problem for exact or wavefunction-based calculations, in the fictitious non-interacting Kohn-Sham system at the heart of modern DFT methods, the energies of orbitals other than the highest occupied have no meaning [92, 93, 94, 95]. Therefore a potential based upon these levels is clearly approximate. On the other hand, the potential in the real time propagation method is based entirely on the applied potential which is, of course, known. With such theoretical advantages, it is reasonable to explore transport behavior within real time TDDFT to determine the important effects impacting electron transport.

Finally, we make a note about comparison of the calculated currents to experimental results. It is a common feature of currents calculated using NEGF/DFT, that the calculated currents for molecular systems are approximately one to two orders of magnitude larger than measured currents. However, these currents show the correct

qualitative response to potential. We will see that the real time method has the same property. We will see in chapter 5, that this property is at least partially a result of approximations in the quantum mechanical parts of the energy equation. It is also possible that the lack of experimentally known geometry may impact our ability to correctly calculate currents. We will also see some indication that the steady state assumption of NEGF may result in some overcalculation, but this effect is unlikely to produce overcalculation of several orders of magnitude. Correcting this error is a large focus of research into conduction calculations.

1.6 Thesis Format

In this thesis, we will examine the electronic transport behavior of single molecule devices using the real time propagation method described in section 1.5, occasionally comparing to the behavior predicted by the NEGF method discussed in section 1.4. The methods discussed in this paper rely heavily upon computational quantum chemistry. Thus, we provide a background on quantum chemistry methods in chapter 2. The remaining chapters examine various aspects of real time electron transport. In chapter 3, we introduce the time-dependent density functional theory (TDDFT) method and examine closed-shell transport in simple polyacetylene model systems. We expand to open-shell transport in chapter 4 and compare the transport properties of spin and charge quasiparticles both on polyacetylene and under a model Hamiltonian. DFT calculations are not exact, because the exact exchange-correlation functional is not known. Therefore, in chapter 5, we examine the effects of exchange and correlation on transport properties. Due to the computational cost of including non-local correlation, we here resort to the use of a model Hamiltonian as well. Finally in chapter 6, we study a realistic system and examine the accuracy of the steady state assumption that is the core of the NEGF method. All equations in this thesis are presented in atomic units ($\hbar = q_e = m_e = 1$) unless otherwise noted.

Chapter 2

Quantum Chemistry Methods

2.1 Basis Sets

The linear nature of the Schrödinger equation allows us to solve quantum mechanical problems within the confines of linear algebra leading to the use of basis sets as described in section 1.2. Typically, when we define the basis in a quantum chemistry calculation, we are describing the three dimensional functions from which single particle wavefunctions are constructed. In quantum chemistry, the two most common types of bases are the plane wave basis, formed from normalized functions of the form $Ce^{i\mathbf{k}\cdot\mathbf{r}}$, and the Gaussian basis.

The work in this thesis is accomplished using a Gaussian basis. The Gaussian basis is constructed using three-dimensional normalized Gaussian basis functions centered on the atomic coordinates. Additionally, Gaussians may be multiplied by real-valued angular functions to give basis functions with a larger angular momentum quantum number. For example, the s and p_x gaussian basis functions are of the form:

$$\begin{aligned}\phi_s^G(x,y,z) &= \left(\frac{8\alpha^3}{\pi^3}\right)^{1/4} e^{-\alpha\left[(x-x_0)^2+(y-y_0)^2+(z-z_0)^2\right]},\\ \phi_{p_x}^G(x,y,z) &= \left(\frac{128\alpha^5}{\pi^3}\right)^{1/4} xe^{-\alpha\left[(x-x_0)^2+(y-y_0)^2+(z-z_0)^2\right]},\end{aligned} \tag{2.1}$$

where (x_0, y_0, z_0) is the location of the atomic center. Each Gaussian basis function

includes a parameter α which controls how diffuse the function is. Unlike for plane-waves, there is no single parameter to adjust the size of the basis set. Instead, a basis set may be augmented by the addition of higher angular momentum basis functions, useful to describe polarized wavefunctions, or functions with reduced values of α, useful for diffuse wavefunctions. Unfortunately, this makes discussing the basis dependence of a result more complicated. In addition, for ease of computation, several Gaussians of the form shown in equation 2.1 are often contracted into a single basis function. Due to the complexity of defining a basis, standard Gaussian basis functions are named and often augmented. The Gaussian basis sets used in this work are STO-3G [96], 6-31G* [97], the minimal basis associated with the Hay-Wadt pseudopotential [98], and the Aldrichs VDZ basis [99] augmented with heavy atom d functions.

The advantage of Gaussian functions is that they closely resemble the atomic hydrogen orbitals, and thus by summation, the molecular orbitals. Therefore, far fewer basis functions are needed to accurately describe the molecular wavefunction and more sophisticated and computationally expensive quantum chemistry methods are possible. Although plane waves are conceptually simpler, this practical advantage has caused Gaussians to become the dominant basis for quantum chemistry studies of molecular systems.

2.2 Variational Principle

Computational quantum mechanics relies upon the variational principle to define a *best* approximation to the ground state of a quantum mechanical system within a reduced search space. The principle states that no normalized wavefunction has a lower expectation energy than the ground state. We can prove this principle by noting that the set of all normalized eigenstates of a Hamiltonian $\hat{H}$ forms a complete orthonormal basis. Therefore, we can write an arbitrary normalized wavefunction as a linear combination of the eigenstates of $\hat{H}$:

$$|\Phi\rangle = \sum_{\alpha} c_{\alpha}|\psi_{\alpha}\rangle, \tag{2.2}$$

where $\sum_\alpha ||c_\alpha||^2 = 1$. Calculating the expectation energy of state $|\Phi\rangle$, we find

$$\begin{aligned}\langle\Phi|\hat{H}|\Phi\rangle &= \sum_{\alpha,\beta} c_\alpha^* c_\beta \langle\psi_\alpha|\hat{H}|\psi_\beta\rangle \\ &= \sum_{\alpha,\beta} c_\alpha^* c_\beta E_\alpha \delta_{\alpha,\beta}, \\ \langle E\rangle &= ||c_0||^2 E_0 + \sum_{\alpha\neq 0} ||c_\alpha||^2 E_\alpha,\end{aligned} \tag{2.3}$$

where the subscript 0 refers to the ground. Note that the eigenbasis here has the same dimensionality (3*number of particles) as the many-particle wavefunction and is not a basis for functions in three dimensional space like the plane-wave and Gaussian bases described in section 2.1. Combining the normalization of $|\Phi\rangle$ with the definition of ground state ($E_0 \leq E_\alpha$) we see that $\langle E\rangle$ is a weighted average of terms greater that or equal to E_0. The *best* approximation is therefore the wavefunction in the solution space that minimizes the expectation energy. This definition becomes invaluable in quantum chemistry methods as the immense size of the solution space of many particle systems requires that we search for the best wavefunction within a subspace restricted by our choice of basis set and quantum chemistry method.

When we apply the variational principle in the solution space of all normalized functions that can be described by an arbitrary (not necessarily complete) basis, we transform our eigenfunction problem into an eigenvector problem. If we consider our solution as a linear combination of basis functions like in equation 2.2, we get an expectation energy of

$$\langle\Phi|\hat{H}|\Phi\rangle = \sum_{\alpha,\beta} c_\alpha^* c_\beta \langle\phi_\alpha|\hat{H}|\phi_\beta\rangle - \epsilon\left(\sum_\alpha c_\alpha^* c_\alpha - 1\right). \tag{2.4}$$

Note that we have replaced ψ with ϕ because we are dealing with an arbitrary basis, not an eigenbasis. For this same reason, we cannot replace out Hamiltonian operator with a scalar energy. We have also added a Lagrange multiplier ϵ to enforce normalization. Optimizing with respect to c_α^*, by setting the derivative of the expectation

energy to 0, we find that

$$\begin{aligned} 0 &= \sum_{\beta} H_{\alpha,\beta} c_{\beta} - \epsilon c_{\alpha}, \\ \mathbf{H}|\Psi\rangle &= \epsilon|\Psi\rangle. \end{aligned} \tag{2.5}$$

Thus, we construct an eigenvector problem from the variational principle and an eigenfunction problem. Such eigenvector equations form the bedrock of quantum chemistry methods.

2.3 Electronic Hamiltonian

2.3.1 All Electron Hamiltonian

We introduced the concepts of the Schrödinger equation and Hamiltonian in section 1.2. Now, we will focus specifically on the many-particle electronic Hamiltonian of a molecular system. If we consider the nuclei to be fixed point charges, then the full electronic Hamiltonian is

$$\hat{H} = -\sum_{\alpha}^{N} \frac{1}{2}\nabla_{\alpha}^{2} - \sum_{\alpha,A}^{\alpha=N,A=M} \frac{Z_A}{r_{\alpha,A}} + \sum_{\alpha,\beta<\alpha}^{N} \frac{1}{r_{\alpha,\beta}}, \tag{2.6}$$

where M is the number of nuclei,N is the number of electrons, and $r_{\alpha,\beta}$ is the distance between the α^{th} and β^{th} particles. The Hamiltonian contains both one and two particle terms with the one particle terms often expressed as the single operator $\hat{h}^{core} = -\sum_{\alpha}^{N} \frac{1}{2}\nabla_{\alpha}^{2} - \sum_{\alpha,A}^{\alpha=N,A=M} \frac{Z_A}{r_{\alpha,A}}$. This is done because the one-particle term is generally easy to treat in a many-electron system. On the other hand, the remaining two-electron term is responsible for the computational complexity of quantum-chemistry methods.

In sections 2.4, 2.5, and 2.6, we will examine methods to attack the complexity caused by the two-electron term. These sections discuss methods of searching for a $3N$-dimensional wavefunction that obeys the known properties of fermions. Those properties are:

1. Normalization - When the square modulus of the wavefunction is integrated over all dimensions, the result is 1.

2. Exchange antisymmetry - exchanging any two electrons changes the sign of the wavefunction.

Thus, a quantum-chemistry ground state method attempts to determine the lowest energy eigenstate of the operator given in equation 2.6 that satisfies the above properties of fermions and lies within a solution subspace defined within the approximations of the method.

2.3.2 Effective Core Potentials

In section 2.3.1, we discussed the full electronic Hamiltonian given in equation 2.6. However, for atoms beyond the first few rows of the periodic table, the large number of electrons causes very large computational cost due to the number of basis functions required to describe them. However, many of these electrons are core electrons which are tightly bound and do not significantly contribute to chemical behavior. Furthermore, an all-electron nonrelativistic treatment of heavy atoms will likely incorporate non-negligible errors by ignoring relativistic effects of the core electrons.

The importance of the core electrons is their effect on valence electrons by shielding them from the nucleus and through Pauli exclusion. Thus, it is reasonable to replace the core electrons by an additional one-electron pseudopotential. The pseudopotentials include parameters that are adjusted to correctly reproduce valence electron structure. Generally, bases are designed with a particular pseudopotential in mind by reducing the large exponent Gaussians in favor of more diffuse functions to model the valence electrons. Thus, the pseudopotential method significantly reduces the size of the basis, and hence the computational cost. In addition, a pseudopotential can model relativistic core electrons without explicitly including relativity in our calculation [100, 101, 102]. In this work, we do not develop pseudopotentials, but use them in chapter 6 to reduce the computational cost in modeling gold contacts. We use the effective core potential designed by Hay and Wadt [98].

2.4 The Hartree-Fock Method

2.4.1 Single-determinant Solution Space

The first *ab initio* many-electron method that we will examine is the Hartree-Fock (HF) Method. The derivation of this method is provided in detail elsewhere [82], so here we provide only the necessary background for this thesis. The HF method seeks the lowest energy eigenstate of equation 2.6 within the subspace of the simplest many-particle functions that obey the fermion property requirements listed in section 2.3.

The solution space of the HF method is the space of all Slater determinant wavefunctions, wavefunctions of the form

$$\Psi\left(\mathbf{r_1}, \mathbf{r_2}, ..., \mathbf{r_N}\right) = \frac{1}{\sqrt{N!}} \begin{vmatrix} \chi_1\left(\mathbf{r_1}\right) & \chi_2\left(\mathbf{r_1}\right) & \cdots & \chi_N\left(\mathbf{r_1}\right) \\ \chi_1\left(\mathbf{r_2}\right) & \chi_2\left(\mathbf{r_2}\right) & \cdots & \chi_N\left(\mathbf{r_2}\right) \\ \vdots & \vdots & & \vdots \\ \chi_1\left(\mathbf{r_N}\right) & \chi_2\left(\mathbf{r_N}\right) & \cdots & \chi_N\left(\mathbf{r_N}\right) \end{vmatrix}, \tag{2.7}$$

where χ_i is the i^{th} single-particle spin-orbital. For the sake of conciseness, we will use the notation

$$|\Psi\rangle = |\chi_1\chi_2 \cdots \chi_N\rangle, \tag{2.8}$$

to indicate a Slater determinant wavefunction. We can see that exchanging two electrons is equivalent to switching two rows, so the wavefunction is antisymmetric to exchange. Additionally, as long as each of the spin-orbitals are normalized, the Slater determinant will be normalized as well.

As we have now introduced a many-electron wavefunction, we will also introduce the density matrix, which contains equivalent information as the filled molecular

orbitals. The density matrix is given by

$$\begin{aligned} \hat{P} &= \sum_{a \ occ.} |a\rangle\langle a|, \\ P_{ij} &= \sum_{a \ occ.} c_i^a c_j^{*a}, \end{aligned} \tag{2.9}$$

and is generally used as the primary description for the electronic, single-determinant, quantum state.

2.4.2 Fock Equation

In section 2.4.1, we constructed the Slater-determinant many-particle wavefunction from normalized spin orbitals. Next, we will tackle the problem of determining the single-electron spin orbitals themselves using a variational approach. We will take as given the number of up ($\uparrow$) and down ($\downarrow$) spin electrons as the Hamiltonian in section 2.3 has no term which couples states of different charge or multiplicity. We start by writing the spin orbitals in terms of the spin basis functions:

$$\chi_a\left(\mathbf{r}, \omega\right) = c_i^a \phi_i\left(\mathbf{r}, \omega\right). \tag{2.10}$$

The spin basis functions are formed by multiplying each spatial basis function by either the up or down spin function. Calculating the expectation energy of a Slater determinant state, we find

$$\begin{aligned} \langle \chi_1 \chi_2 \cdots \chi_N | \hat{H} | \chi_1 \chi_2 \cdots \chi_N \rangle &= \sum_{a \ occ.} \langle \chi_a | \hat{h}^{core} | \chi_a \rangle + \frac{1}{2} \sum_{a,b \ occ.} \left(\langle ab|ab\rangle - \langle ab|ba\rangle \right), \\ E &= \sum_{i,j} P_{ji} h_{ij}^{core} + \frac{1}{2} \sum_{i,j,k,l} P_{ki} P_{lj} \left(\langle ij|kl\rangle - \langle ij|lk\rangle \right), \end{aligned} \tag{2.11}$$

where

$$\langle ij|kl\rangle = \int d\mathbf{r_1} d\mathbf{r_2} d\omega_1 d\omega_2 \chi_i^*\left(\mathbf{r_1}, \omega_1\right) \chi_j^*\left(\mathbf{r_2}, \omega_2\right) \frac{1}{r_{1,2}} \chi_k\left(\mathbf{r_1}, \omega_1\right) \chi_l\left(\mathbf{r_2}, \omega_2\right). \tag{2.12}$$

For the second equation, we have also included the basis set expansion coefficients in terms of the density matrix $\hat{P}$ defined in equation 2.9. Note that the single determinant wavefunction produces two different kinds of energy terms from the electron-electron repulsion operator. The first is of the type $J_{ab} = \langle ab|ab\rangle$ and is called the coulomb term. This term is the classical electrical repulsion between two negatively-charged particles and tends to delocalize the electron density. The second is of the type $K_{ab} = \langle ab|ba\rangle$ and is called exchange. The exchange term has no classical analogue, and tends to partially counteract the coulomb term. In the case that $a = b$, the coulomb and exchange terms exactly cancel, so an electron does not interact with itself.

We have determined the expectation energy of a single determinant wavefunction in terms of the single electron spin orbital expansion parameters c_i^a. According to the variational principle, we can determine the best Slater determinant approximation to the true ground state by constrained minimization of the expectation energy with respect to the expansion coefficients. The imposed constraints are orthonormality of the spin orbitals. We leave the algebra determining the resulting eigenproblem to other sources [82] and here simply present the result. The spin orbitals can be determined by solving

$$\begin{aligned}
\mathbf{F}[\mathbf{P}]\mathbf{c^a} &= \epsilon_a \mathbf{S}\mathbf{c^a}, \\
\mathbf{F}[\mathbf{P}] &= \sum_{i,j} |i\rangle h_{ij}^{core} \langle j| + \mathbf{J}[\mathbf{P}] + \mathbf{K}[\mathbf{P}], \\
\mathbf{J}[\mathbf{P}] &= \sum_{i,j,k,l} |i\rangle P_{lj} \langle ij|kl\rangle \langle k|, \\
\mathbf{K}[\mathbf{P}] &= \sum_{i,j,k,l} |i\rangle P_{lj} \langle ij|lk\rangle \langle k|,
\end{aligned} \tag{2.13}$$

where $\mathbf{S}$ is the overlap matrix of the spin basis, and $\mathbf{F}$ is referred to as the Fock matrix defined from the Fock operator, $\hat{F}$.

Because the Fock operator does not interact with electron spin, it commutes with the electron spin operator, and we can factor the spin orbitals into spatial and spin pieces without approximation. Only Fock matrix elements between spin basis func-

tions with the same spin piece are nonzero, leading to a block diagonal structure. As a result, we can separate both the Fock matrix and density matrix into up and down spin components. The expectation energy with a spin separated density matrix is given by

$$\begin{aligned} E[\mathbf{P}] &= \sum_{i,j} \left(P_{ji}^{\uparrow} + P_{ji}^{\downarrow} \right) h_{i,j}^{core} + E_J[\mathbf{P}] - E_K[\mathbf{P}], \\ E_J[\mathbf{P}] &= \frac{1}{2} \sum_{i,j,k,l} (P_{ki}^{\uparrow} + P_{ki}^{\downarrow})(P_{lj}^{\uparrow} + P_{lj}^{\downarrow}) \, (ij|kl), \\ E_K[\mathbf{P}] &= \frac{1}{2} \sum_{i,j,k,l} (P_{ki}^{\uparrow} P_{lj}^{\uparrow} + P_{ki}^{\downarrow} P_{lj}^{\downarrow}) \, (ij|lk), \end{aligned} \tag{2.14}$$

where the subscripts i, j, k, and l now refer to spatial basis functions. We now use the notation $(ij|lk)$ which is defined analogously to 2.12, but refers to spatial orbitals. The resulting Fock matrices are

$$\begin{aligned} \mathbf{F}^{\uparrow(\downarrow)}[\mathbf{P}] &= \sum_{i,j} \langle i|h_{ij}|j\rangle + \mathbf{J}[\mathbf{P}] + \mathbf{K}^{\uparrow(\downarrow)}[\mathbf{P}], \\ \mathbf{J}[\mathbf{P}] &= \sum_{i,j,k,l} |i\rangle (P_{lj}^{\uparrow} + P_{lj}^{\downarrow}) \, (ij|kl) \, \langle k|, \\ \mathbf{K}^{\uparrow(\downarrow)}[\mathbf{P}] &= \sum_{i,j,k,l} |i\rangle P_{lj}^{\uparrow(\downarrow)} \, (ij|lk) \, \langle k|. \end{aligned} \tag{2.15}$$

The up and down spin states are coupled through the coulomb term, while the exchange term acts only between electrons of the same spin. The restricted energy and Fock matrices are achieved by requiring $\mathbf{P}^{\uparrow} = \mathbf{P}^{\downarrow} = \mathbf{P}$ and apply to the situation that both spins are required to have the same spatial orbitals.

Because $\mathbf{F}$ depends on $\mathbf{P}$, $\mathbf{P}$ must be determined self consistently. The density matrix $\mathbf{P}$ is a self consistent solution if $\mathbf{F}[\mathbf{P}]$ yields the same density matrix that was used to construct it. The self consistent field (SCF) procedure is shown in Fig. 2-1. An initially guessed $\mathbf{P}$ is iteratively improved until self-consistency is achieved. The Hartree-Fock energy is variational, so iterative improvements decrease the total energy. Several methods exist to update the density matrix. The most common method is DIIS [103] which uses past density matrix iterations to improve the guess

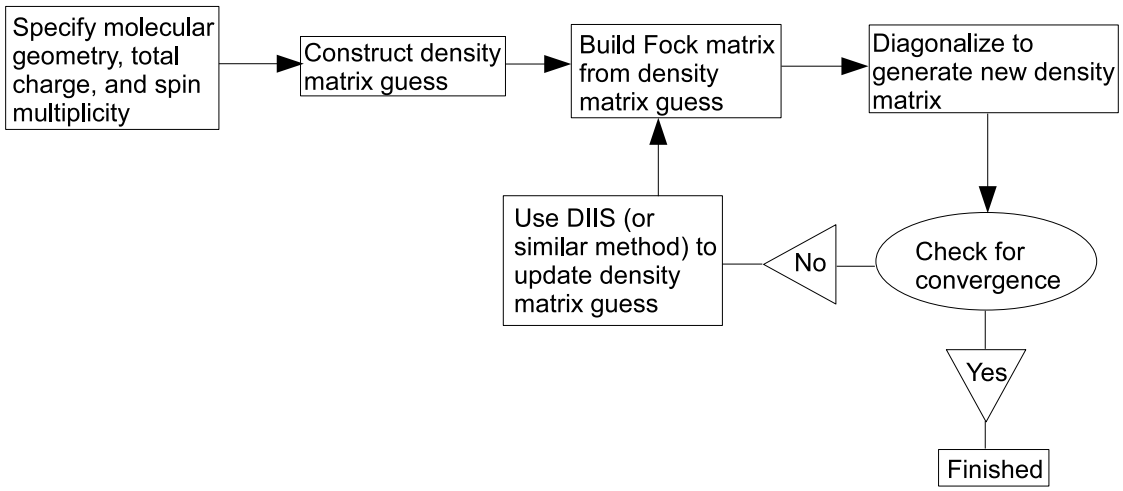

Figure 2-1: Flow chart depicting the self-consistent field procedure.

for the next iteration.

2.5 Correlated Methods

For a given wavefunction in the Slater determinant solution space, Hartree-Fock includes the exact exchange energy. This quantum mechanical decrease in energy is achieved by enforcing antisymmetry through the Slater-determinant state. However, a single determinant wavefunction, or equivalently the mean-field approximation, cannot show correlation energy. By definition, correlation energy is the difference between the lowest energy achieved by a Slater determinant wavefunction, and the minimum energy of the non-relativistic electronic Hamiltonian within the chosen basis. The Slater determinant assumes that the spatial distributions of individual electrons are independent of one another. However, there is no reason to expect this to be the case as electron 2 will tend to redistribute to avoid electron 1. Indeed, the N-electron wavefunction is a complex function of 3N dimensions and, in general, is not separable into a product of 3-dimensional single-electron orbitals. A correlated wavefunction is constructed, not as a single determinant, but as a linear combination of many single determinants. Here we briefly describe the basics of determining correlation through post-Hartree-Fock methods. However, because this thesis does not include any post-

Hartree-Fock calculations we give only a general overview and leave the details to other sources [82].

The conceptually simplest method to achieve correlation is through configuration interaction (CI). In the CI method, the full electronic Hamiltonian (equation 2.6) is expanded in the basis of a reference Slater determinant $|\Psi_0\rangle$ and related excited determinants $|\Psi^{rst\cdots}_{abc\cdots}\rangle$. Here we simplify our discussion by ignoring the use of spin-adapted basis functions to avoid spin contamination [82]. The excited determinant $|\Psi^{rst\cdots}_{abc\cdots}\rangle$ refers to the determinant formed by removing electrons from filled spin orbitals a, b, c, *etc.* and placing them in virtual orbitals r, s, t, *etc.*. The many electron Hamiltonian matrix is determined in the single-determinant basis

We can generally think of the reference determinant as the result of a Hartree-Fock calculation. However, if we are performing a full CI calculation, our reference determinant can be any determinant formed from orthonormalized orbitals. That is because altering the orbitals, while maintaining orthonormalization, is equivalent to simply performing a unitary basis set transformation. Of course, this raises the question of why we perform Hartree-Fock at all, rather than just perform full CI with an arbitrary orthonormalized reference configuration. To answer that question, we consider the size of the basis for a full CI calculation. For a calculation involving K spatial basis functions, N up spin, and M down spin electrons, the number of basis determinants is $\begin{pmatrix} K \\ N \end{pmatrix}\begin{pmatrix} K \\ M \end{pmatrix}$ if we take into account that the Hamiltonian cannot mix states with different total spins. As an example of how quickly this number can grow, a calculation of N_2 (7 up and 7 down spin electrons) with the STO-3G basis set (minimal basis with 10 total basis functions) would be considered a trivial Hartree-Fock calculation for any modern computer. On the other hand, the full CI calculation would involve 14,400 single-determinant basis functions, nearly the limit that can be handled by a typical CPU. Thus, it is clear that full CI is impossible for any but the smallest systems. A reasonable reference determinant, such as that obtained from Hartree-Fock is useful in obtaining useful results from a *truncated* CI-like calculation. Several methods exits to truncate the CI expansion. We will not

examine any of the traditional truncation methods as we do not use them in this work. In chapter 5, we will examine a modified correlation procedure which attempts to select determinants that are important to the problem at hand to form a basis for the correlated calculation. Unfortunately, all wavefunction based correlation methods are very expensive relative to Hartree-Fock. In section 2.6, we will examine density functional theory, a method that can include at least some local correlation at about the same computational cost as Hartree-Fock.

2.6 Density Functional Theory

Density functional theory (DFT)[104] has grown to be one of the most widely used methods to study molecular systems. DFT is based upon the idea that one needs only the three-dimensional electron density, not the 3N-dimensional electronic wavefunction, to describe the electronic state of the system. Depending upon the specific functional chosen, DFT can be more accurate than Hartree-Fock at approximately the same cost. While the most accurate functionals often include parameters that are fit to experiment, thereby disqualifying DFT from being truly *ab initio* in those cases, the practical benefit of accurate DFT methods cannot be denied.

2.6.1 Hohenberg-Kohn Theorems

The theoretical bedrock of density functional theory is the Hohenberg-Kohn theorems. Essentially, the Hohenberg-Kohn theorems state that because all electronic structure problems are identical except for the three-dimensional, single-particle potential on the electrons, the three-dimensional electron density is sufficient to entirely determine the electronic state of the system. Furthermore, the resulting energy functional of the density is variational with respect to the electronic density. We will now examine more rigorously the justification for the Hohenberg-Kohn theorems.

The first Hohenberg-Kohn theorem states that *the external potential* $v(\mathbf{r})$ *is determined, within a trivial additive constant, by the electron density* $\rho(\mathbf{r})$ [105, 104]. The simple proof is by contradiction. We assume contrary to our theorem that we have an

electron density $\rho(\mathbf{r})$ which results from two different potentials $v(\mathbf{r})$, and $v'(\mathbf{r})$. Once we specify the one-electron potential, we have entirely specified our Hamiltonian, and therefore our wavefunction. Thus, we associate with the potential $v(\mathbf{r})$, the Hamiltonian $\hat{H}$, the wave function Ψ, and the ground energy E_0. Likewise, we associate $\hat{H}'$, Ψ', and E_0' with $v'(\mathbf{r})$. Applying the variational principle discussed in section 2.2, we know

$$\begin{aligned} E_0 = \langle\Psi|\hat{H}|\Psi\rangle < \langle\Psi'|\hat{H}|\Psi'\rangle = \langle\Psi'|\hat{H}'|\Psi'\rangle + \langle\Psi'|\hat{H} - \hat{H}'|\Psi'\rangle, \\ E_0 < E_0' + \int d\mathbf{r}\rho(\mathbf{r})\left[v(\mathbf{r}) - v'(\mathbf{r})\right], \end{aligned} \tag{2.16}$$

where we get the second line by realizing that the two Hamiltonians differ only in the one-electron potential. Likewise,

$$E_0' < E_0 - \int d\mathbf{r}\rho(\mathbf{r})\left[v(\mathbf{r}) - v'(\mathbf{r})\right]. \tag{2.17}$$

Combining equations 2.16 and 2.17, we find that $E_0 + E_0' < E_0' + E_0$. This is of course a contradiction. Thus we prove that if $v(\mathbf{r})$ and $v'(\mathbf{r})$, differ by more than an additive constant (so that they result in different ground state wavefunctions), they cannot produce the same electron density. In other words, the electron density determines the one electron potential up to an additive constant, and we have proven the first Hohenberg-Kohn theorem. From here, it is obvious to see that $\rho(\mathbf{r})$ determines $\hat{H}$ and Ψ. Thus $\rho(\mathbf{r})$ entirely determines the electronic state of the system.

The first Hohenberg-Kohn theorem allows us to state that the total energy is a functional of the electron density, which we will call $E[\rho]$. We know the one electron potential energy, so we can separate it to define

$$E_v[\rho] = \int d\mathbf{r}\rho(\mathbf{r})v(\mathbf{r}) + F_{HK}[\rho], \tag{2.18}$$

where $F_{HK}[\rho]$ is the universal functional of ρ for the kinetic and two-electron energies of ρ. The subscript v indicates the explicit dependence of the one-electron potential upon v. This notation is important in determining a variational principle for ρ, which

is the topic of the second Hohenberg-Kohn theorem.

The theorem states that *for a trial density* $\tilde{\rho}(\mathbf{r})$*, such that* $\tilde{\rho}(\mathbf{r}) \geq 0$ *and* $\int d\mathbf{r}\tilde{\rho}(\mathbf{r}) = N$*,*

$$E_0 \leq E_v\left[\tilde{\rho}\right]. \tag{2.19}$$

Note that to understand this theorem, one must understand the meaning of $E_v\left[\tilde{\rho}\right]$. $E_v\left[\tilde{\rho}\right]$ is the energy of the trial density under the predefined potential $v(\mathbf{r})$. Thus, we clarify that $E_{\tilde{v}}\left[\tilde{\rho}\right] = E\left[\tilde{\rho}\right]$, but $E\left[\tilde{\rho}\right] \neq E_v\left[\tilde{\rho}\right]$, because they have different one-electron potentials unless $\tilde{\rho}(\mathbf{r})$ is the correct density corresponding to $v(\mathbf{r})$. To prove this, we remember that the first theorem allows us to associate a wavefunction $\tilde{\Psi}$ with $\tilde{\rho}$ which we can apply to our predefined Hamiltonian $\hat{H}$. By the variational theorem,

$$\begin{aligned} \langle\tilde{\Psi}|\hat{H}|\tilde{\Psi}\rangle &\geq E_v[\rho] \\ E_v\left[\tilde{\rho}\right] &\geq E_v[\rho], \end{aligned} \tag{2.20}$$

and we have proven the second Hohenberg-Kohn theorem. The second theorem provides a path for determining $\rho(\mathbf{r})$ directly from a given potential $v(\mathbf{r})$, which is the problem we regularly tackle with quantum chemistry methods.

2.6.2 Kohn-Sham Method

The disappointing aspect of the first Hohenberg-Kohn theorem is that it has an existence proof, not a construction proof. Thus, we know that $E[\rho]$, or likewise $F_{HK}[\rho]$ exist, but we do not know what they are. Initial attempts were made to apply the energy functional derived for a uniform electron gas. This Thomas-Fermi model, however, suffers from the inability to bind two atoms together [104, 106, 107]. Attempts at corrections based upon the gradient of the density have met with mixed success [108]. Here, we discuss instead the method used in this work, and indeed the method used in the great majority of density-functional research, that of Kohn and Sham. Where previously attempts were focused on approximating $E[\rho]$ directly, Kohn and Sham divided $E[\rho]$ into several pieces to be attacked separately. Following

their lead, we can separate the energy functional as

$$\begin{aligned} E[\rho] &= T_S[\rho] + \int d\mathbf{r}\rho(\mathbf{r})v(\mathbf{r}) + J[\rho] + E_{xc}[\rho], \\ T_S[\rho] &= \sum_i^N \langle\psi_i| - \frac{1}{2}\nabla^2|\psi_i\rangle, \\ J[\rho] &= \frac{1}{2}\int\int d\mathbf{r_1}d\mathbf{r_2}\frac{\rho(\mathbf{r_1})\rho(\mathbf{r_2})}{r_{1,2}}, \\ E_{xc}[\rho] &= T[\rho] - T_S[\rho] + V_{ee}[\rho] - J[\rho], \end{aligned} \tag{2.21}$$

where $V_{ee}[\rho]$ is the full two electron energy and $J[\rho]$ is the classical part of that energy. We have introduced orbitals ψ_i so that we can calculate $T_S[\rho]$, the approximate kinetic energy, using the exact kinetic energy operator. The term $E_{xc}[\rho]$ is the exchange-correlation functional and contains both the nonclassical part of the two-electron energy and the part of the true kinetic energy, $T[\rho]$, not accounted for by $T_S[\rho]$.

Applying the variational principle of 2.19, we find that

$$\begin{aligned} \left[-\frac{1}{2}\nabla^2 + v(\mathbf{r}) + \int d\mathbf{r}'\frac{\rho(\mathbf{r}')}{|\mathbf{r}-\mathbf{r}'|} + v_{xc}(\mathbf{r})\right]\psi_i &= \epsilon_i\psi_i, \\ v_{xc}(\mathbf{r}) &= \frac{\delta E_{xc}[\rho]}{\delta\rho(\mathbf{r})}. \end{aligned} \tag{2.22}$$

Thus, much like we did for Hartree-Fock, we have replaced our interacting many electron energy expression with an eigenvalue problem describing a noninteracting system. Because both sides of the equation depend upon ρ, ρ must be determined self consistently. We have changed our electron density optimization into an orbital optimization problem. Upon determining our orbitals, we can calculate the total density using

$$\rho(\mathbf{r}) = \sum_i^N |\psi_i(\mathbf{r})|^2. \tag{2.23}$$

The orbitals determined do not necessarily reflect the true wavefunction for the solution density. Where Hartree-Fock assumes an approximate form for the wavefunction, and therefore the approximate wavefunction has physical meaning, the Kohn-Sham method instead proposes an approximate eigenvalue problem which is designed

to return the correct total density. This discrepancy between the true wavefunction and the calculated orbitals is the reason that $T[\rho]$ and $T_S[\rho]$ differ.

Upon initial examination, it may be difficult to see the value in the Kohn-Sham method. First of all, while our energy functional $E[\rho]$ is *by definition* exact, it still contains a term, $E_{xc}[\rho]$, that we do not know how to calculate. Additionally, we have relinquished the simplicity of only examining total density by requiring orbitals to calculate kinetic energy. However, we notice that the magnitude of the unknown functional term is significantly smaller than the total energy, so an approximate functional has less impact. Furthermore, the Hohenberg-Kohn theorem and Kohn-Sham method give us a framework in which to examine a range of exchange-correlation functionals. Where Hartree-Fock locked us into exact exchange and no correlation, DFT provides much more flexibility to explore calculation methods. Thus, while we are still constrained to examine orbitals, we have significantly broadened our space for exploration.

2.6.3 Spin Density Functional Theory

As we have now examined a practical method of determining the ground state density given $v(\mathbf{r})$, it is useful to discuss practically dealing with total electron spin. This will be important in chapter 4 when we examine spin conduction as well as charge conduction. Spin density functional theory [109, 110, 104] seeks the ground state electron density in the presence of not only an electric field (giving rise to $v(\mathbf{r})$), but a magnetic field. We will consider here only the case that the magnetic field is everywhere parallel. The direction of the magnetic field will be defined as the z direction. Effectively, we have two different external potentials; one for the up spin density, and one for the down spin density. We will not cover the details as they are a simple extension of sections 2.6.1 and 2.6.2, but we must extend the Hohenberg-Kohn theorems and Kohn-Sham method to systems in the presence of a magnetic field. We must now consider the up and down spin electron densities ($\rho^{\uparrow}(\mathbf{r})$ and $\rho^{\downarrow}(\mathbf{r})$) as the sufficient variables to describe the full quantum mechanical electronic

state. Furthermore, we have separate up and down spin Kohn-Sham equations:

$$\left[-\frac{1}{2}\nabla^2 + v(\mathbf{r}) + \beta_e b(\mathbf{r}) + \int d\mathbf{r}' \frac{\rho^{\uparrow}(\mathbf{r}') + \rho^{\downarrow}(\mathbf{r}')}{|\mathbf{r}-\mathbf{r}'|} + v_{xc}^{\uparrow}(\mathbf{r})\right] \psi_i^{\uparrow}(\mathbf{r}) = \epsilon_i^{\uparrow}\psi_i^{\uparrow}(\mathbf{r}),$$
$$\left[-\frac{1}{2}\nabla^2 + v(\mathbf{r}) - \beta_e b(\mathbf{r}) + \int d\mathbf{r}' \frac{\rho^{\uparrow}(\mathbf{r}') + \rho^{\downarrow}(\mathbf{r}')}{|\mathbf{r}-\mathbf{r}'|} + v_{xc}^{\downarrow}(\mathbf{r})\right] \psi_i^{\downarrow}(\mathbf{r}) = \epsilon_i^{\downarrow}\psi_i^{\downarrow}(\mathbf{r}),$$
$$v_{xc}^{\uparrow(\downarrow)}(\mathbf{r}) = \frac{\delta E_{xc}[\rho^{\uparrow}, \rho^{\downarrow}]}{\delta \rho^{\uparrow(\downarrow)}(\mathbf{r})}, \tag{2.24}$$

where β_e is the Bohr magneton, and $b(\mathbf{r})$ is the strength of the magnetic field. These equations give us a method to determine electronic states in the presence of a magnetic field.

Spin density functional theory is also useful in the case that $b(\mathbf{r}) = 0$. While technically, the exact $E_{xc}[\rho]$ in traditional density functional theory does not require any spin assumption, and should reflect the correct spin from just the total density, known approximations do not have this property. Instead, approximate $E_{xc}[\rho]$ generally assume a closed-shell solution. Open-shell treatment instead relies upon an exchange-correlation functional of the form $E_{xc}[\rho^{\uparrow}, \rho^{\downarrow}]$. Furthermore, like Hartree-Fock, the number of up and down spin electrons are generally specified *a priori* and the constrained state search is performed within the space of the *a priori* determined spin multiplicity. Thus, even when no magnetic field is present, open shell systems are best treated within spin density functional theory.

2.6.4 Functionals

As stated in section 2.6.2, the exchange-correlation functional, $E_{xc}[\rho]$ is not known, and instead must be approximated. In this section, we examine several avenues to approximate this functional. For most of these methods, we consider the exchange ($E_x[\rho]$) and correlation ($E_c[\rho]$) energies separately with the understanding that $E_{xc}[\rho] = E_x[\rho] + E_c[\rho]$. All of the functionals used in this thesis are available in most standard DFT packages except for the range separated hybrid functionals.

Local Density Approximation Local density approximate exchange-correlation

functionals are functionals of the form.

$$E_{xc}[\rho^{\uparrow},\rho^{\downarrow}] = \int d\mathbf{r}\epsilon_{xc}[\rho^{\uparrow}(\mathbf{r}),\rho^{\downarrow}(\mathbf{r})]. \tag{2.25}$$

The exchange-correlation functional is a local functional of the density. The local density approximation (LDA) functional used throughout this work is derived from the uniform electron gas. Dirac [111] presented the exchange piece of the LDA as

$$E_x^{LDA}[\rho^{\uparrow},\rho^{\downarrow}] = \frac{3}{4}\left(\frac{6}{\pi}\right)^{1/3}\int d\mathbf{r}\left(\rho^{\uparrow 4/3}(\mathbf{r}) + \rho^{\downarrow 4/3}(\mathbf{r})\right). \tag{2.26}$$

Unfortunately there is no known exact closed expression for the correlation energy of the uniform electron gas. The standard LDA functional uses a parameterized expression that was fit to the results of Monte Carlo simulations of the uniform electron gas at a number of electron densities. The resulting expressions, referred to as VWN5 are too complicated to be reproduced here, but are available elsewhere [112].

Generalized Gradient Approximation The LDA functional is based upon the uniform electron gas and works best for systems with slowly varying electron density. Molecular and atomic systems, however, can have very heterogeneous densities. The next level of approximation considers variations in the electron density and acts not only on the local density, but on the local gradient as well. As a result, these generalized gradient approximate (GGA) functionals are often referred to as semilocal. These GGA functionals are be of the form

$$E_{xc}[\rho^{\uparrow},\rho^{\downarrow}] = \int d\mathbf{r}\epsilon_{xc}[\rho^{\uparrow}(\mathbf{r}),\rho^{\downarrow}(\mathbf{r}),\vec{\nabla}\rho^{\uparrow}(\mathbf{r}),\vec{\nabla}\rho^{\downarrow}(\mathbf{r})]. \tag{2.27}$$

Although we do not directly use any GGA functionals in this work, we shall give as an example GGA functionals that are incorporated in the hybrid functionals we use. As an example of a gradient approximation for the exchange functional, we give the

Becke88 functional [113]:

$$
\begin{aligned}
E_x^{B88}[\rho^\uparrow, \rho^\downarrow] &= E_x^{LDA}[\rho^\uparrow, \rho^\downarrow] - \beta \sum_{\sigma=\uparrow,\downarrow} \int d\mathbf{r} \rho_\sigma^{4/3}(\mathbf{r}) \frac{x_\sigma^2}{1 + 6\beta x_\sigma sinh^{-1} x_\sigma}, \\
x_\sigma &= \frac{|\nabla \rho_\sigma|}{\rho_\sigma^{4/3}}, \\
\beta &= 0.0042,
\end{aligned}
\tag{2.28}
$$

where $E_x^{LDA}[\rho^\uparrow, \rho^\downarrow]$ is defined in equation 2.26 and β was determined by fitting to the *ab initio* exchange energies of the noble gases. This exchange functional produces the correct asymptotic electron density.

Like for LDA, we will not include the GGA correlation functional used in this work. We use the LYP correlation functional (E_c^{LYP}) [114] which is generated by gradient expansion of the local kinetic-energy density. The gradient expansion is used to convert a second-order Hartree-Fock based correlation energy [115] into a density functional.

Hybrid Functionals The exchange functionals examined so far are both local and approximate. However, the Hartree-Fock method includes exchange exactly as calculated in equation 2.14. This expression requires orbitals, but we are already calculating Kohn-Sham orbitals to calculate the kinetic energy. Thus it seems reasonable to apply the Hartree-Fock exchange energy expression to the Kohn-Sham orbitals. We once again consider the exchange and correlation energies separately, but use the exact exchange functional:

$$
\begin{aligned}
E_x^{HF}[\rho^\uparrow, \rho^\downarrow] &= -\frac{1}{2} \int \int d\mathbf{r_1} d\mathbf{r_2} \left[\frac{\left|\rho^{\uparrow\uparrow}(\mathbf{r_1}, \mathbf{r_2})\right|^2}{r_{1,2}} + \frac{\left|\rho^{\downarrow\downarrow}(\mathbf{r_1}, \mathbf{r_2})\right|^2}{r_{1,2}} \right], \\
\rho^{\sigma\sigma}(\mathbf{r_1}, \mathbf{r_2}) &= \sum_{a \ occ.} n_a^\sigma \psi_a^\sigma(\mathbf{r_1}) \psi_a^{\sigma *}(\mathbf{r_2}).
\end{aligned}
\tag{2.29}
$$

The Kohn-Sham equations then become

$$\begin{aligned}
&\left[-\frac{1}{2}\nabla^2 + v(\mathbf{r}) + \beta_e b(\mathbf{r}) + \int d\mathbf{r}' \frac{\rho^{\uparrow}(\mathbf{r}') + \rho^{\downarrow}(\mathbf{r}')}{|\mathbf{r}-\mathbf{r}'|} + v_c^{\uparrow}(\mathbf{r})\right]\psi_i^{\uparrow}(\mathbf{r}) \\
&\qquad\qquad - \int d\mathbf{r}' \frac{\rho^{\uparrow\uparrow}(\mathbf{r},\mathbf{r}')}{|\mathbf{r}-\mathbf{r}'|}\psi_i^{\uparrow}(\mathbf{r}') = \epsilon_i^{\uparrow}\psi_i^{\uparrow}(\mathbf{r}), \\
&\left[-\frac{1}{2}\nabla^2 + v(\mathbf{r}) - \beta_e b(\mathbf{r}) + \int d\mathbf{r}' \frac{\rho^{\uparrow}(\mathbf{r}') + \rho^{\downarrow}(\mathbf{r}')}{|\mathbf{r}-\mathbf{r}'|} + v_c^{\downarrow}(\mathbf{r})\right]\psi_i^{\downarrow}(\mathbf{r}) \\
&\qquad\qquad - \int d\mathbf{r}' \frac{\rho^{\downarrow\downarrow}(\mathbf{r},\mathbf{r}')}{|\mathbf{r}-\mathbf{r}'|}\psi_i^{\downarrow}(\mathbf{r}') = \epsilon_i^{\downarrow}\psi_i^{\downarrow}(\mathbf{r}), \\
&\qquad\qquad v_c^{\uparrow(\downarrow)}(\mathbf{r}) = \frac{\delta E_c[\rho^{\uparrow},\rho^{\downarrow}]}{\delta\rho^{\uparrow(\downarrow)}(\mathbf{r})}.
\end{aligned} \tag{2.30}$$

Equation 2.30 is no longer the Kohn-Sham method, because the effective exchange potential is not local. Instead we can refer to this as Hartree-Fock Kohn-Sham (HFKS) [104] method. Indeed, traditional Hartree-Fock can be considered an HFKS method with $E_c[\rho^{\uparrow},\rho^{\downarrow}] = 0$.

Other than traditional HF, we do not use any methods with 100% exact exchange. Instead, we use an example of a hybrid functional. Hybrid functionals mix traditional local and semilocal expressions with the exact exchange method. The hybrid functional we use in this work is B3LYP [116]. This method calculates the xc energy according to the equation

$$\begin{aligned}
E_{xc}^{B3LYP} = (1-a_0)E_x^{LDA} + a_0 E_x^{HF} + a_x(E_x^{B88} - E_x^{LDA}) \\
+ a_c E_c^{LYP} + (1-a_c)E_c^{LDA},
\end{aligned} \tag{2.31}$$

where $a_0 = 0.2$, $a_x = 0.72$, and $a_c = 0.81$. These parameters were determined for a similar set of functionals by fitting a series of energy calculations [113]. The B3LYP functional has since become a standard for molecular calculations with the ability to calculate bonding energies to near chemical accuracy.

The B3LYP optimized parameters clearly do not result in 100% exact exchange, thus introducing errors in the exchange energy. This indicates that there is a systematic error in the approximate correlation energy. The error introduced into the exchange energy must then partially counteract the correlation error.

Range-Separated Hybrid Functionals The hybrid functionals discussed above include several parameters to mix the approximate xc methods. However, there is little reason to believe that the optimized parameters should be the same at all electron separations, especially if the approximate functionals are more or less accurate at those separations. Indeed, it is common to use different parameters for different applications. Range-separated hybrid functionals [117] are generated by separating the Coulomb operator into a long-range and short-range piece:

$$\frac{1}{r} = \frac{1 - a(r)}{r} + \frac{a(r)}{r}, \tag{2.32}$$

where $a(r)$ is a function that increases monotonically from 0 to 1 as r goes from 0 to ∞. The exchange-correlation functional then becomes

$$E_{xc} = (1 - a(r))E_x^{Short}c + a(r)E_x^{Long}c. \tag{2.33}$$

In this work, we make use of the long-range corrected LDA (LC-LDA) functional which combines the short range LDA functional with long range Hartree-Fock exchange with $a(r) = \text{erf}(\omega r)$ [118]. We set $\omega = 0.5$ Å, because that value was previously shown to work well [119, 120]. We use this functional to separate the effects of short and long range exact exchange because it has no short range exact exchange but the correct long-range asymptotic behavior. This functional includes no long-range correlation because HF has no correlation, and LDA includes only local correlation.

2.6.5 DFT Inaccuracies

DFT calculates the electronic energy including both exchange and correlation at similar computational cost to Hartree-Fock. Thus it is significantly less costly than correlated post Hartree-Fock methods. However, this reduced computational cost is instead paid in accuracy. In this section, we will examine some of the systematic errors in DFT calculations.

Lack of Derivative Discontinuity So far we have considered only densities that

represent an integer number of electrons. The microstate of a system can include only an integer number of electrons, so we can achieve non-integer densities only in the grand canonical ensemble. Our ensemble density matrix is

$$\hat{\Gamma} = \sum_n \sum_i p_{ni} |\psi_{ni}\rangle\langle\psi_{ni}|. \tag{2.34}$$

We are going to focus exclusively on the 0 temperature case, so we need only consider the ground state density for each integer number of particles. Furthermore, it can be shown as a result of the always positive concavity of the energy as a function of electron number that the minimum energy, n-electron density matrix is

$$\begin{aligned} \hat{\Gamma} &= (1 - \Delta n)\mathbf{P}_{\lfloor n \rfloor} + \Delta n \mathbf{P}_{\lfloor n \rfloor + 1}, \\ \Delta n &= n - \lfloor n \rfloor, \end{aligned} \tag{2.35}$$

where $\lfloor n \rfloor$ is the greatest integer less than or equal to n. We leave the proof of this minimum energy result to other source [104, 92]. The corresponding energy is

$$E_v(n) = (1 - \Delta n)E_v(\lfloor n \rfloor) + \Delta n E_v(\lfloor n \rfloor + 1). \tag{2.36}$$

This energy expression indicates that there should be a discontinuity in the chemical potential $\left(\mu = \frac{\partial E}{\partial n}\right)$ as a function of n. However, the local and semilocal approximate exchange-correlation functionals do not reflect this property, often resulting in incorrect charge transfer properties in asymmetric bonds [92]. Furthermore, the lack of derivative discontinuity has been shown to affect transport properties because conducting state energies and populations vary too smoothly and significantly impact the predicted band gap [121, 122].

Self Interaction Error Another source of inaccuracy present in DFT is the presence of self-interaction error (SIE). This is the property of most approximate functionals that an electron will interact with its own density. The source of this error can be illustrated by examining the Hartree-Fock energy equation 2.11. In this equation, the coulomb energy summation includes terms of the form $\langle aa|aa\rangle$,

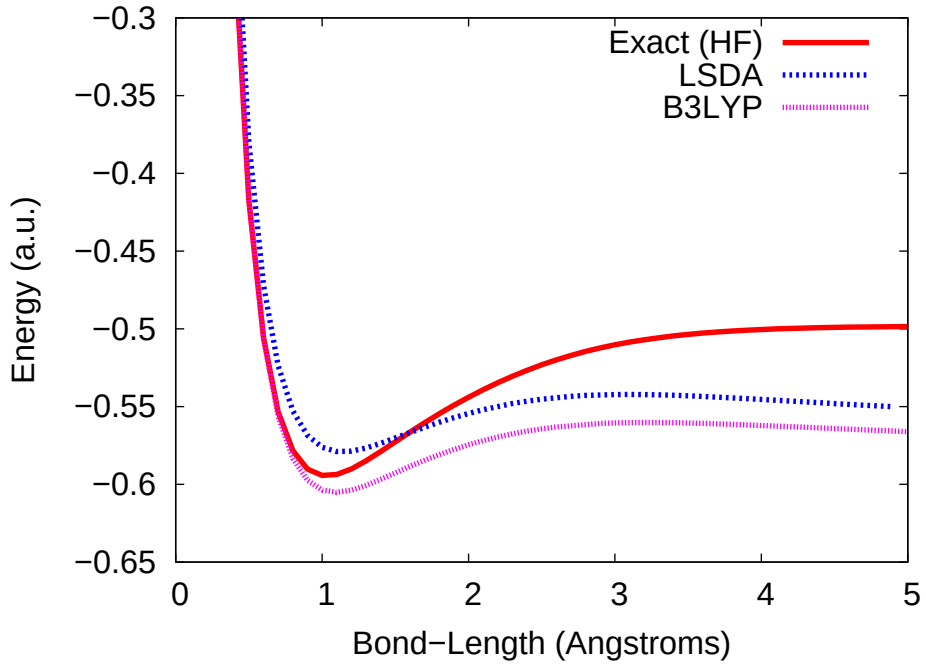

Figure 2-2: Dissociation energy curves of H_2^+ calculated using Hartree-Fock, LDA, and B3LYP. The HF calculation is exact within the basis set (6-311+G**) approximation for this system.

which represents the Coulombic repulsion between an electron and itself. In the Hartree-Fock method, the exchange summation includes terms to exactly cancel these artifactual repulsions. However, when an approximate exchange functional is used, these self-interaction terms do not exactly cancel.

As an example of self-interaction error, we plot the H_2^+ dissociation curve as calculated by Hartree-Fock, LDA, and B3LYP in Fig. 2-2. Because there is only one electron and thus no correlation, the Hartree-Fock result is exact. Furthermore, all three methods include the same one-electron piece, and so differ only in an artificial two-electron energy. The differences between the Hartree-Fock and other methods is entirely due to self-interaction. One common effect of self-interaction is an increase in electron delocalization. Several studies have also indicated that self-interaction significantly increases calculated conductances [123, 122, 124].

Lack of Nonlocal Correlation In the post Hartree-Fock wavefunction methods, correlation is the property introduced when switching from a single determi-

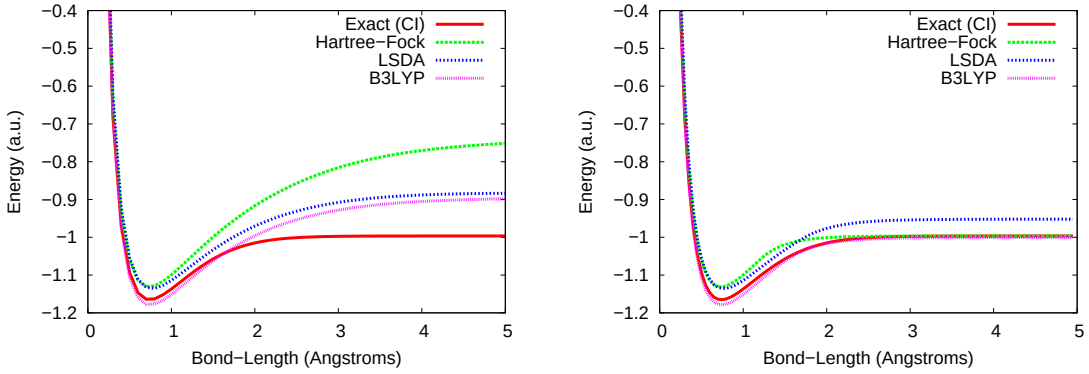

Figure 2-3: Dissociation energy curves of H_2 calculated using CI, Hartree-Fock, LDA, and B3LYP. CI is exact within the chosen basis set (6-31+G**) for this system. The approximated methods are calculated with a restricted (left) and unrestricted (right) density.

nant wavefunction to a linear combination of determinants. Although in principle, the Kohn-Sham exchange-correlation potential contains the exact correlation energy, common local and semilocal approximations do not correctly account for nonlocal correlation. Even the nonlocal piece of B3LYP is devoted to exchange energy.

In Fig. 2-3, we show the dissociation curve of H_2 to illustrate the effects of correlation. The difference between HF and the exact results is due entirely to correlation. Due to the variational principle, nonlocal correlation will only lead to a decrease in energy, so the CI calculated energy will always be below that calculated by HF. LDA and B3LYP reaches lower energies due to errors in the exchange and local correlation terms. Physically, correlation decreases the energy by allowing electrons to avoid one another. The restricted single-determinant methods, by definition, do not allow the electrons to avoid one another. The unrestricted calculation allows the electrons to avoid one another by localizing each on a different atom, but this localization carries an energy cost, especially at short distances with large coupling between atomic orbitals. Only the CI method can minimize the energy by allowing both electrons to delocalize, but still avoid one another. In chapter 5, we will examine the impact of nonlocal correlation on currents.

2.6.6 Time-Dependent DFT

So far, we have focused upon ground state, or time-independent phenomena. Excited state, or time-dependent behavior can be examined under time-dependent density functional theory (TDDFT). Where ground state DFT is based upon the Hohenberg-Kohn theorems, TDDFT derives from the Runge-Gross theorem [125]. This theorem states the following:

> For every single-particle potential $v(\mathbf{r}, t)$ which can be expanded into a Taylor series with respect to the time coordinate around $t = t_0$, a map $G : v(\mathbf{r}, t) \rightarrow n(\mathbf{r}, t)$ is defined by solving the time-dependent Schrödinger equation with a fixed initial state $\Phi(t_0) = \Phi_0$ and calculating the corresponding densities $n(\mathbf{r}, t)$ This map can be inverted up to an additive merely time-dependent function in the potential.

In other words, the density determines the time-dependent potential up to a time-dependent constant of space, and therefore determines the wavefunction up to a phase factor. Although the proof of this theorem is more involved than that of the Hohenberg-Kohn theorem and thus beyond the scope of this work, the proof structures are similar. The proof relies on the Hamiltonian varying only in the single-particle potential. Two different potentials are assumed and shown by contradiction to produce different time-dependent densities. The same work provides another theorem much like the variational principle of the second Hohenberg-Kohn theorem. In this case, the correct time dependent density is shown to be a stationary point of the quantum mechanical action integral,

$$A[\rho] = \int_{t_0}^{t_f} dt \langle \Psi(t) | i\frac{\partial}{\partial t} - \hat{H} | \Psi(t) \rangle, \tag{2.37}$$

which is a functional of the density.

Finally, Runge and Gross present an extension of the Kohn-Sham formalism to time-dependent conditions. Like the time-independent KS equations, the TDKS is a Schrödinger-like equation with an effective potential in place of the nonclassical

two-electron terms. Thus,

$$\left[-\frac{1}{2}\nabla^2 + v(\mathbf{r},t) + \int d\mathbf{r}' \frac{\rho(\mathbf{r}',t)}{|\mathbf{r}-\mathbf{r}'|} + v_{xc}(\mathbf{r},t)\right]\psi_i(\mathbf{r},t) = i\frac{\partial}{\partial t}\psi(\mathbf{r},t),$$
$$v_{xc}(\mathbf{r},t) = \frac{\delta A_{xc}[\rho]}{\rho(\mathbf{r},t)}, \tag{2.38}$$

where $A_{xc}[\rho]$ is the exchange-correlation action. In this work, we treat $A_{xc}[\rho]$ in the adiabatic approximation [126] so v_{xc} is determined from the functionals created for ground state calculations. This approximation is most appropriate in the case of small time-dependent changes in the potential. We do not examine the adiabatic approximation further as it has been shown to describe low-lying excited states well [127, 128] and we are mostly concerned with states within the voltage potential.

TDDFT is most often used in a linear response [129] framework. However, a linear treatment is inappropriate in a number of applications such as calculating Rydberg states [130, 131, 132] and charge transfer states [133, 134, 135] in which the excited state varies significantly from the ground state. This is due to the local nature of exchange-correlation functionals. The difficulty in treating charge-transfer states is especially concerning regarding the ability of linear response TDDFT to treat transport. However, we treat TDDFT in a fully non-linear real time propagation framework. We will describe in chapter 3 the numerical method we use to solve the full TDDFT equations.

2.7 Pariser-Parr-Pople Model Hamiltonian

A major drawback of the electronic structure methods explored in this chapter is their computational cost. To save on computational cost and increase the ease of exploration, it is often beneficial to perform calculations on model systems that maintain the necessary physics while significantly reducing the degrees of freedom in the simulation. For example, to demonstrate the basic physics of quantum scale conductance in section 1.5.1, we used the Hückel model Hamiltonian. Such semi-empirical calculations can also reduce the computational cost by replacing *ab initio* matrix elements,

that must be calculated, with adjustable parameters.

The Hückel model reflects the conjugated π system of single-molecule conductors which contribute only one orbital per atom to the extended π system. However, the Hückel system lacks the electron-electron interaction necessary for any but the most superficial examinations. In this thesis, we make use of the Pariser-Parr-Pople (PPP) semi-empirical model [136, 137]. This model places one basis function on each atom like the Hückel model, but also includes electron-electron interaction described by the Mataga-Nishimoto [138, 139] formula. Neglecting nuclear-nuclear interaction, the Hamiltonian takes the form:

$$\begin{aligned} \hat{H} &= \sum_{j,k} \sum_{\sigma=\uparrow,\downarrow} \beta_{jk} \hat{c}^{\dagger}_{j,\sigma} \hat{c}_{k,\sigma} - \sum_{j,k}^{N} \Gamma_{j,k} \hat{n}_j + \frac{1}{2} \sum_{j,k} \Gamma_{j,k} \hat{n}_j \hat{n}_k, \\ \Gamma_{j,k} &= \left(r_{j,k} + \frac{1}{g_{jk}} \right)^{-1}. \end{aligned} \tag{2.39}$$

In these equations, the summation indices j and k refer to atomic site. The operator $\hat{n}_j \equiv \left(\hat{c}^{\dagger}_{j,\uparrow} \hat{c}_{j,\uparrow} + \hat{c}^{\dagger}_{j,\downarrow} \hat{c}_{j,\downarrow} \right)$ is the number operator on the j^{th} site. The terms in equation 2.39 from left to right are, the kinetic energy operator, the electron-nuclear attraction, and the electron-electron repulsion. Note that the electron interaction energy has the correct limits; $\Gamma_{jj} = g_{jj}$, and $\Gamma_{jk} \to \frac{1}{r_{jk}}$ as $r_{jk} \to \infty$. The parameters in the model Hamiltonian are the bond distances (r_{jk}), the site-to-site hopping parameter (β_{jk}), and the same site electronic interaction strength (g_{jk}). The value of r_{jk} is fixed by geometry. This leaves the values of β_{jk} and g_{jk} to be set as parameters. Although Mataga and Nishimoto suggested values for these parameters for some common atomic environments, we will instead fit them to the TDDFT results we are modeling.

We use an unrestricted Hartree Fock (single determinant) prescription for the

wavefunction analogous to section 2.4, which yields the energy:

$$
\begin{aligned}
E\left[\mathbf{P}\right] &= -\sum_{j,k}\beta_{jk}\left(P^{\uparrow}_{j,k}+P^{\downarrow}_{j,k}\right)-\sum_{j,k}^{N}\Gamma_{j,k}\left(P^{\uparrow}_{j,j}+P^{\downarrow}_{j,j}\right)+E_J\left[\mathbf{P}\right]-E_K\left[\mathbf{P}\right],\\
E_J\left[\mathbf{P}\right] &= \frac{1}{2}\sum_{j,k}^{N}\Gamma_{j,k}\left(P^{\uparrow}_{j,j}+P^{\downarrow}_{j,j}\right)\left(P^{\uparrow}_{k,k}+P^{\downarrow}_{k,k}\right),\\
E_K\left[\mathbf{P}\right] &= \frac{1}{2}\sum_{j,k}^{N}\Gamma_{j,k}\left(P^{\uparrow}_{j,k}P^{\uparrow}_{k,j}+P^{\downarrow}_{j,k}P^{\downarrow}_{k,j}\right),
\end{aligned}
\tag{2.40}
$$

where $\mathbf{P}$ is the one particle density matrix with separate up and down spin parts, and E_J and E_K are the Coulomb and exchange energies, respectively. Variationally solving for the orbital coefficients, we find the single particle up and down spin Fock operators:

$$
\begin{aligned}
\hat{F}^{\uparrow(\downarrow)}\left[\mathbf{P}\right] &= -\sum_{j,k}\beta_{jk}\hat{c}^{\dagger}_{j,\uparrow(\downarrow)}\hat{c}_{k,\uparrow(\downarrow)}-\sum_{j,k}^{N}\Gamma_{j,k}\hat{n}_j+\hat{J}\left[\mathbf{P}\right]-\hat{K}^{\uparrow(\downarrow)}\left[\mathbf{P}\right],\\
\hat{J}\left[\mathbf{P}\right] &= \sum_{j,k}^{N}\Gamma_{j,k}\left(P^{\uparrow}_{k,k}+P^{\downarrow}_{k,k}\right)\hat{n}_j,\\
\hat{K}^{\uparrow(\downarrow)}\left[\mathbf{P}\right] &= \sum_{j,k}^{N}\Gamma_{j,k}P^{\uparrow(\downarrow)}_{j,k}\hat{c}^{\dagger}_{j}\hat{c}_{k}.
\end{aligned}
\tag{2.41}
$$

Like the full electron methods, only the exchange piece differs between the up and down spin Fock operators. Hence the exchange piece affects electrons of each spin separately, while the Coulomb piece affects the total distribution.

The methods described in this chapter represent the present available means to calculate the quantum nonrelativistic electronic state from first principles. In the next chapter we will describe our method to examine electronic conductance using real time simulations under the techniques described in this chapter.

Chapter 3

Real Time TDDFT Propagation

Note: The bulk of this chapter has been published in Ref. [140].

In section 1.5, we discussed in general a method to treat conduction in a real-time propagation framework. To make use of this method in a quantum chemistry framework, it is necessary to develop a procedure to propagate the state described in quantum chemistry. Our purpose in this chapter is to establish the TDDFT propagation method and demonstrate it's utility on a polyacetylene model system. In a method first published in [140], we turn our attention to TDDFT discussed in section 2.6.6. TDDFT, in principle, gives an exact treatment of excited electronic states [141] as opposed to the traditional NEGF/DFT method which uses the DFT single-particle operator to approximate for the exact many-particle Hamiltonian. The method in this chapter builds upon previous works regarding the formal basis for TDDFT conduction simulations [142, 143, 144] and practical techniques [84, 145, 83, 146].

3.1 TDKS Propagation Theory

We propagate the electronic state using the time-dependent Kohn-Sham (TDKS) formalism in which we obtain an effective one-particle Schrödinger equation (2.38) for the KS orbitals

$$\hat{H}[\rho]_{KS}(t)|\psi_a\,(t)\rangle = i\frac{\partial}{\partial t}|\psi_a(t)\rangle, \tag{3.1}$$

where $\rho(t) \equiv \sum_{a\ occ} |\psi_a(t)|^2$ is the time dependent density. By formal integration, we solve 3.1 to find

$$\begin{aligned} |\psi_a(t+dt)\rangle &= \hat{U}(t+dt)|\psi_a(t)\rangle, \\ \hat{U}(t+dt) &\equiv \hat{T}\exp\left\{-i\int_t^{t+dt} dt'\hat{H}_{KS}(t')\right\}, \end{aligned} \tag{3.2}$$

where we write the solution in terms of a time-step dt in anticipation of our numerical method. The operator $\hat{T}$ is the time ordering operator defined in equation 1.6. We make the adiabatic approximation [126] for $\hat{H}_{KS}[\rho](t)$ in that the KS Hamiltonian becomes $\hat{H}_{KS}[\rho(t)]$, depending only on the density at time t. Thus, $\hat{H}_{KS}[\rho](t)$ is defined, according to equation 2.22, as

$$\hat{H}_{KS}(t) = -\frac{1}{2}\nabla^2 + v_{ext}(t) + v_{Jxc}(\rho(t)), \tag{3.3}$$

where $v_{ext}(t)$ includes any external potential, and $v_{Jxc}(\rho(t))$ includes exchange, correlation, and Coulombic effects. The external potential may include explicit time dependence while v_{Jxc} is implicitly time dependent through the density.

Although the TDKS equation is written in terms of KS orbitals, we work instead in terms of the one-particle density matrix defined in equation 2.9. This allows us to generalize our treatment to ensemble states and leads to more elegant equations. The propagation equation 3.2 becomes

$$\mathbf{P}(t+dt) = \hat{U}(t+dt,t)\mathbf{P}(t)\hat{U}^\dagger(t+dt,t) \tag{3.4}$$

Note that $\mathbf{P}$ is defined in terms of the KS orbitals, the eigenfunctions of the noninteracting reference system, and is not the true interacting system one-particle density matrix.

3.2 Numerical Propagation Methods

To numerically solve the TDKS, we require a stepping method in which, for each step, we (1) construct $\hat{U}(t+dt,t)$ and (2) propagate the density matrix from t to $t+dt$. The stepping method maintains time ordering between subsequent steps. However, unless time-ordering and propagator unitarity are properly maintained within the steps, we will need to use impractically short time-steps. This can be accomplished using the Magnus expansion [147]. Formally, the propagator can be expressed as the (time-unordered) exponential of a series of nested commutator integrals:

$$\begin{aligned}
\hat{T}exp\left\{-i\int_t^{t+dt} dt'\hat{H}_{KS}(t')\right\} &= exp(\hat{\Omega}_1+\hat{\Omega}_2+\hat{\Omega}_3+\cdots),\\
\hat{\Omega}_1 &= -i\int_t^{t+dt} d\tau \hat{H}_{KS}(\tau),\\
\hat{\Omega}_2 &= \int_t^{t+dt} d\tau_1\int_t^{\tau_1} d\tau_2[\hat{H}_{KS}(\tau_1),\hat{H}_{KS}(\tau_2)],\\
\hat{\Omega}_3 &= i\int_t^{t+dt} d\tau_1\int_t^{\tau_1} d\tau_2\int_t^{\tau_2} d\tau_3([\hat{H}_{KS}(\tau_1),[\hat{H}_{KS}(\tau_2),\hat{H}_{KS}(\tau_3)]]\\
&\quad +[[\hat{H}_{KS}(\tau_1),\hat{H}_{KS}(\tau_2)],\hat{H}_{KS}(\tau_3)]).\\
&\quad \vdots
\end{aligned} \tag{3.5}$$

Following the work of Blanes *et al.*[148, 149], the numerical evaluation of the propagator is be performed through Gauss-Legendre quadrature of the integrals defining $\hat{\Omega}_i$ coupled to a predictor-corrector scheme.

We will describe application of the numerical evaluation to 2^{nd} order in dt. Higher order evaluations were examined, but empirical results indicated that the increase in allowable step size did not justify the larger number of $\hat{H}_{KS}$ evaluations needed. To second order, the Gauss-Legendre quadrature gives:

$$\begin{aligned}
\hat{U}(t+dt,t) &= exp(\hat{\Omega}_1)+O(dt^3),\\
\hat{\Omega}_1 &= -idt\hat{H}(t+dt/2)+O(dt^3).
\end{aligned} \tag{3.6}$$

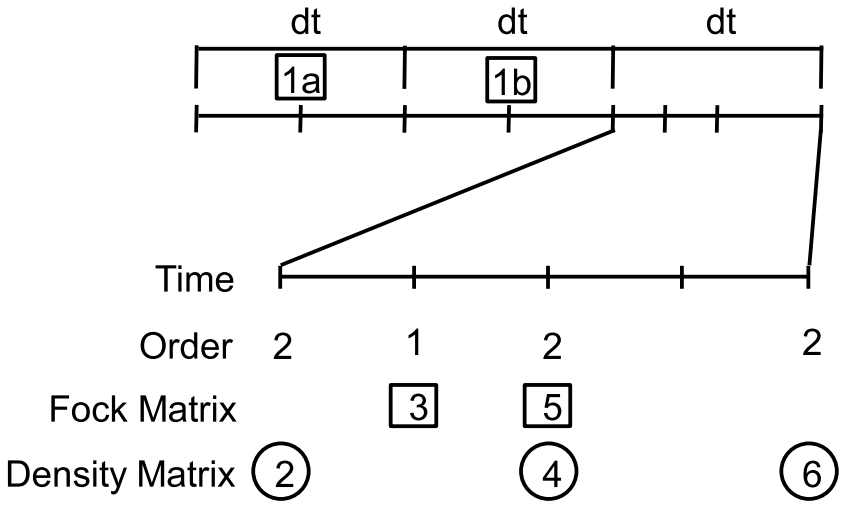

Figure 3-1: Predictor-corrector routine for the 2^{nd} order Magnus integrator. The order row shows the time order (in dt) to which the matrices in the same column are correct.

This equation indicates that to propagate from t to $t + dt$, we need to evaluate $\hat{H}_{KS}(t + dt/2)$.

We obtain $\hat{H}_{KS}(t + dt/2)$ through a predictor-corrector scheme. In this scheme, we linearly extrapolate $\hat{H}_{KS}$ into the time-step interval from its past values and construct and approximate propagator. Then $\hat{\mathbf{P}}$ is propagated into the interval and used to construct a corrected $\hat{H}_{KS}$ and propagator for the full time-step.

In detail, the 2^{nd} order algorithm is illustrated in Figure 3.2. The component steps are:

1. (Predictor) $\hat{H}_{KS}$ matrices stored from previous time steps, 1a and 1b, are used to extrapolate $\hat{H}_{KS}$ matrix 3 to order $O(dt)$: $\hat{H}_{KS}(3) = -\frac{3}{4}\hat{H}_{KS}(1a)+\frac{7}{4}\hat{H}_{KS}(1b)$.

2. (Predictor) Using 3, the density matrix 2 is propagated to 4 using Eq. 3.6. This is correct to $O(dt^2)$.

3. (Corrector) Density matrix 4 is used to compute the $\hat{H}_{KS}$ matrix 5 .

4. (Propagation) $\hat{H}_{KS}$ matrix 5 is used to propagate the density matrix 2 to density matrix 6 using Eq. 3.6. This is correct to $O(dt^2)$.

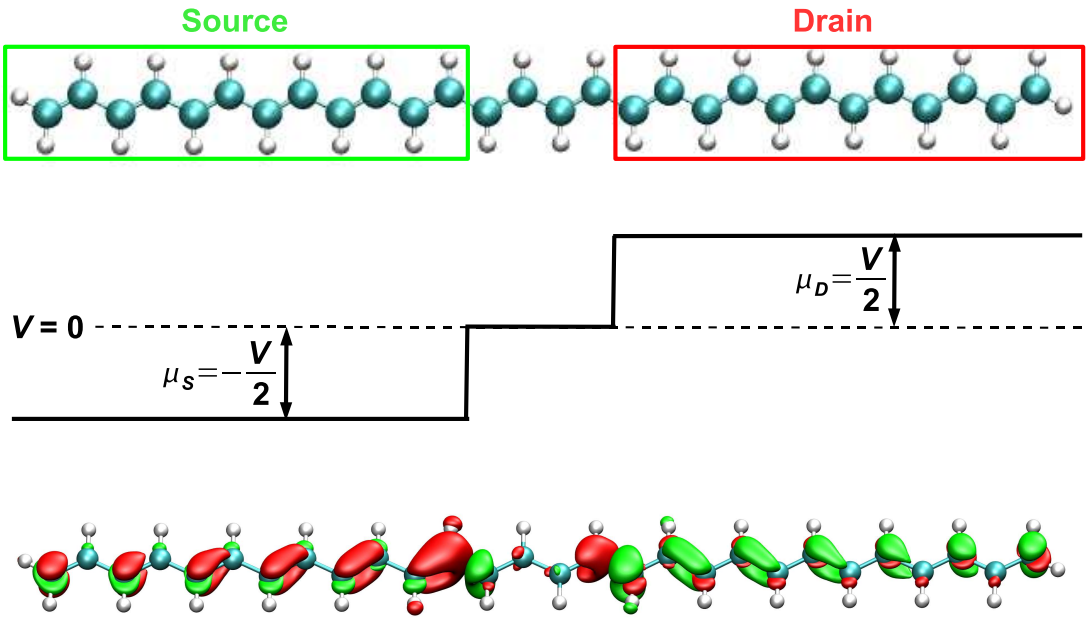

Figure 3-2: (top) Source-wire-drain geometry for *trans*-polyacetylene with lead length of $N = 12$ with the source and drain labeled. With larger N, the source and drain length increase, but the device length remains the same. (mid) Chemical potential under which the initial state is determined for potential V in the chemical potential method. (bottom) Resulting electronic state of the polyacetylene for any time $t < 0$ before the potential is removed at $t = 0$. Red indicates electron accumulation and green indicates electron depletion

5. (Update) For the next step, $\hat{H}_{KS}$ matrix 1b becomes 1a, $\hat{H}_{KS}$ matrix 5 becomes 1b, and density matrix 6 becomes 2. Other matrices are discarded, and the process starts again from step 1.

3.3 Molecular Wire Conductance

We apply the TDDFT real time method with second order Magnus method to model the conductance of a four-carbon segment of a *trans*-polyacetylene wire. The four-carbon segment is the molecular device, and the leads will be modeled by the polyacetylene wires extending to the right and left of the device. Although in principle, the leads should be semi-infinite, the limitations of our method require us to restrict

our attention to finite systems of the form C_NH_{N+1}-C_4H_4-C_NH_{N+1} with the assumption that the leads must be chosen large enough to represent the thermodynamic limit. The system structure with $N = 12$ is shown in Fig. 3-2. For this chapter, we generally choose $N = 23$ and perform a few $N = 48$ calculations to demonstrate convergence with respect to system length. We primarily use the chemical potential method discussed in section 1.5. Figure 3-2 includes a schematic of the potential under which we determine the initial state, and a depiction of the electronic state for $t < 0$. The current is calculated by equation 1.40 which in finite difference form becomes

$$I(t) = \frac{(n_D(t + \Delta t/2) - n_S(t + \Delta t/2)) - (n_D(t - \Delta t/2) - n_S(t - \Delta t/2))}{2\Delta t}. \quad (3.7)$$

.

The methods discussed in sections 3.1 and 3.2 are general to any Gaussian basis and exchange-correlation potential that can be determined from the one-particle density matrix. For this calculation, we choose B3LYP [116] and the 6-31G* [97] basis set. The quantum chemistry calculations were performed in a modified version of NWCHEM [150]. We use a time-step of 24.2 attoseconds (1.0 a.u.).

3.3.1 Average Currents

We begin with a study of $C_{50}H_{52}$ using a chemical potential method defined in section 1.5. We note that although the chemical potential and voltage methods, as defined in 1.5, make use of a sudden change in the Hamiltonian, test calculations indicate that a more gradual transition does not significantly affect the IV results as long as the transition is fast enough so that the transition is complete before finite lead effects occur. The transient currents calculated using a Δt of one time-step is shown in the left of Fig. 3-3. We can see that the currents show a general increasing trend with chemical potential and that the current pinches within about 2.5 fs. This rather short turn-off is not surprising, because our "device" has essentially perfect coupling to the leads, and so the electronic density is able to equilibrate quickly.

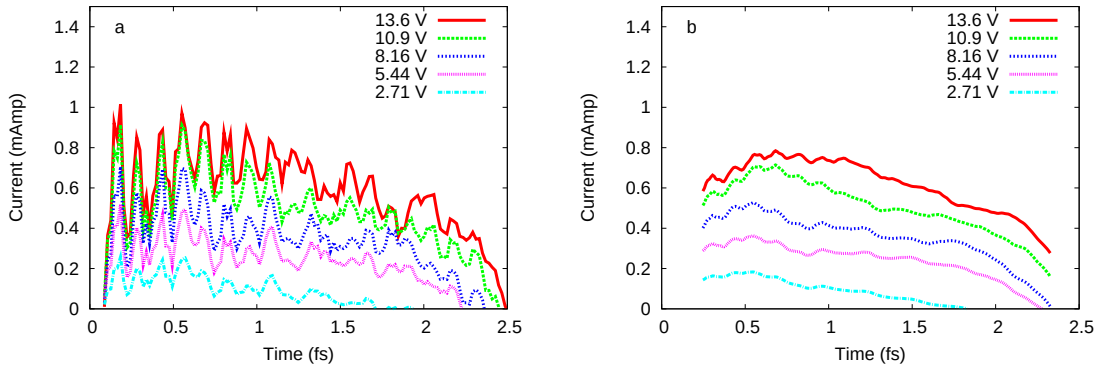

Figure 3-3: (left) Transient current through the central four carbons in $C_{50}H_{52}$ at a series of different initial chemical potentials. The current increases with voltage and includes large, persistent fluctuations. (right) Transient currents smoothed over a time window of width $\Delta t = 0.36$ fs. The currents are now more visible and are converged with respect to time step. The current decays at long times due to partial equilibration of the leads.

Although we can see a trend in the currents, the large fluctuations make assigning a single current difficult. However, we can overcome this difficulty by realizing that experimental measurements are made over a much coarser timescale than our simulation time-step. If we instead choose $\Delta t = 0.36$ fs, the transient currents become much smoother as in the right of Fig. 3-3. Thus, equation 3.7 corresponds to the imaginary experimental device that counts the difference in electrons between the source and drain reservoirs twice with a time resolution of Δt. The device approximates the current via the mean value theorem and thus ignores fluctuations that occur on a timescale faster than Δt.

The time-averaging procedure suppresses the rapid current oscillations and reveals a near steady state in the current. With this smoothing, we can reasonably assign a current to each propagation. We choose the maximum smoothed current under the belief that the current increases to approximately the steady state before equilibration shuts the current off. With this method, we realize that the steady state is reached very quickly (faster than 1 fs), an observation mirroring that made for a gold wire [83]. Like the rapid equilibration, this is a result of the perfect lead-device coupling.

Interpreting the maximum smoothed currents in Fig. 3-3 as the true steady state

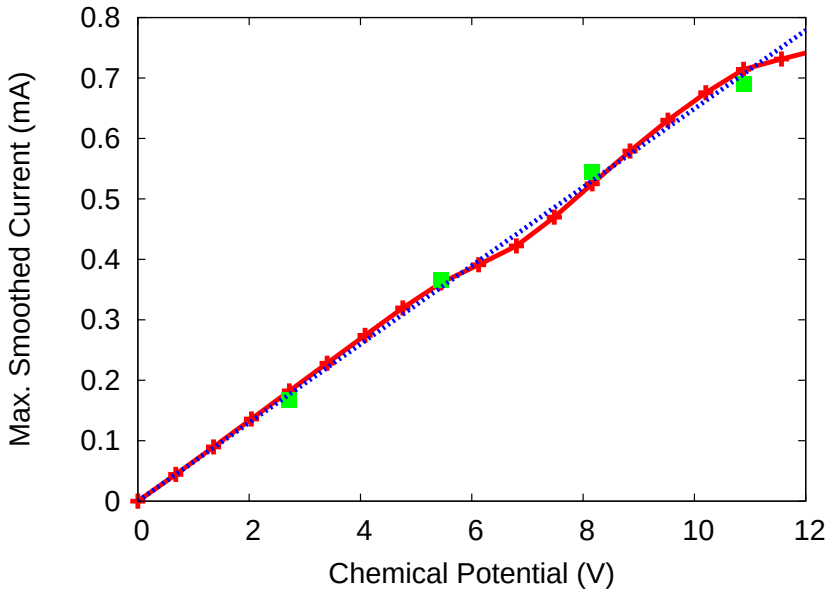

Figure 3-4: Maximum smoothed current through the central four carbons of $C_{50}H_{52}$ (red pluses) and $C_{50}H_{52}$ (green squares) as a function of chemical potential bias. The agreement between these methods demonstrates convergence with respect to lead length. The blue dotted line is a linear fit to the $C_{50}H_{52}$ data and returns a conductance of $\approx 0.85G_0$.

currents, we calculate the I-V curve shown in Fig. 3-4. The current increases nearly linearly until it begins to level off at large bias due to saturation of the current carrying states. Fitting the nearly ohmic I-V results perhaps surprisingly returns a conductance of less than the conductance quantum ($G_0 \approx 77.5\ \mu S$). The calculated conductance is instead about $0.85G_0$. In section 3.3.2, we will establish that this is not an effect of the finite wire length.

Even though we are probing potential differences much larger than the separation between molecular eigenstates, we do not see evidence of a stair-step conductance profile as suggested by the Landauer formula. Indeed, due to the very strong coupling between the leads and device, it is not correct to interpret this result simply in terms of the device states as suggested by the original Landauer picture. Instead, we must consider that the device conduction states are broadened by the leads, and thus the conduction is occurring through the superposition of broadened device states. The stair-step conductance pattern is smeared to produce a linear I-V profile. The

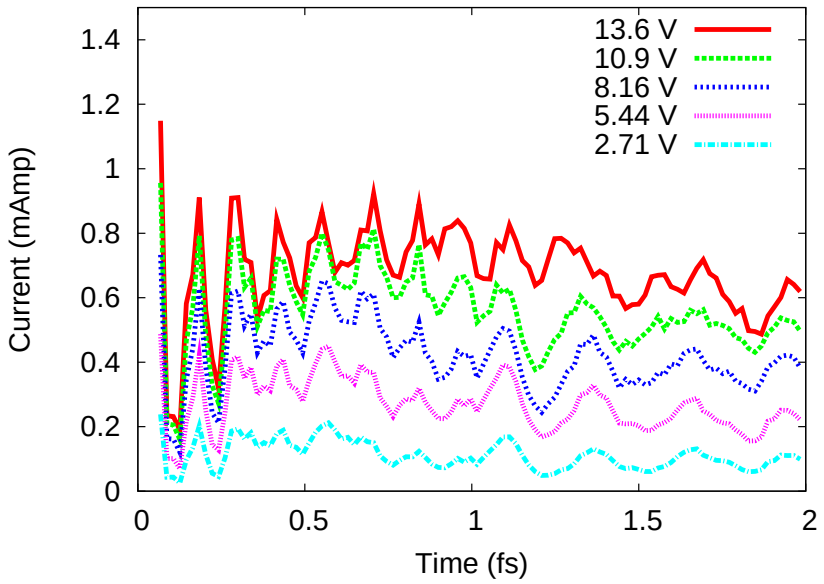

Figure 3-5: Transient current through the central four carbons in $C_{100}H_{102}$ at a series of different chemical potentials. The current fluctuations persist, but the steady-state current lasts longer indicating only the current "shut-off" is a finite lead effect

numerical value of the conductance reflects the density of available conducting states. This study does not rule out the possibility that the reduced conductance relative to G_0 is a finite basis effect.

3.3.2 Comparison to Long Wire Results

Because we are representing an infinite system with a finite model, it is worth examining which of our results can be explained by finite system effects. To that end, we present analogous calculations with $C_{100}H_{102}$ with the same device size as our $C_{50}H_{52}$ calculations. The transient current results are shown in Fig. 3-5, and several I-V points are included in Fig. 3-4. Clearly the current fluctuations are still present with the longer leads, and are therefore not a finite size effect. Furthermore, because the fluctuations occur with larger oscillation periods than the time step, we assert that they are not simply noise due to the numerical integration method. The current fluctuations are characteristic of some physical process in the wire, and may indicate the effect of bound electronic states [151] about the device.

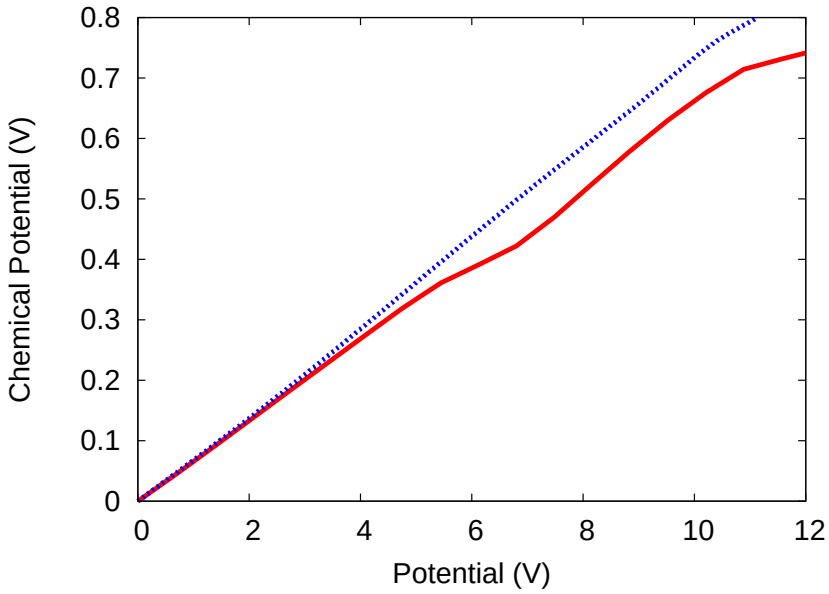

Figure 3-6: Maximum smoothed current through the central four carbons in $C_{50}H_{52}$ as a function of chemical potential bias using real time TDDFT (red solid line) and an NEGF approach described in the text (blue dotted line). The two calculations are nearly identical at low bias and differ somewhat at higher biases due to the lack of self-consistency in the NEGF results.

In terms of the steady state current, Fig. 3-4 indicates that the I-V results remain the same with the larger leads. Therefore in the $C_{50}H_{52}$ calculation, we have converged to the thermodynamic limit in terms of maximum current reached. The current does not shut off as early in the longer wire calculation indicating that indeed the current shut-off is a finite wire effect caused by equilibration of the initial chemical potential difference.

3.3.3 Comparison to NEGF

It is important to note that the current-voltage results from the present approach are completely equivalent to the NEGF formalism [142], insofar as the dynamics above approximate a true steady state of the infinite system. Therefore, a comparison between DFT-NEGF and real-time DFT predictions of the current voltage curves for polyacetylene provide an additional reality check for these calculations. To this end, we have used the simple scheme of applying a Lorentzian broadening to the

leads to obtain conductance results out of finite polyacetylene chains [76]. To be precise, we transform $\hat{H}_{KS}$ into the Löwdin orthogonalized basis and partition the molecule in precisely the same manner as in the time dependent simulations. We then add a constant imaginary part, $\epsilon = .055$, to the diagonal of $\hat{H}_{KS}$ in each lead effectively broadening the lead states and approximating the state continua of infinite wires. The value of ϵ was chosen to maximize the current making the NEGF current analogous to the time dependent results above (which charted the maximum smoothed current versus voltage). The current is then computed using the NEGF technique outlined in section 1.4. This approach does not compute the current self-consistently, because $\hat{H}_{KS}$ is calculated using the equilibrium electron density. However, this simple technique should suffice for the purposes of comparison, particularly at low bias where the self-consistent density should resemble the ground state.

The NEGF results for $C_{50}H_{52}$ are presented in Fig. 3-6 along with the real-time TDDFT results from the previous section. Clearly, the two techniques agree almost quantitatively at low bias and give qualitatively similar results at larger biases. Presumably, a large fraction of the difference at large bias can be accounted for by the lack of self-consistency in the NEGF calculations; as the bias increases, the non-equilibrium density will deviate more significantly from the equilibrium result, leading to larger self-consistency corrections.

Taken together the NEGF results and long wire calculations strongly indicate that our real-time simulations are accessing the open-system limit for this process: the conductance curve does not change appreciably if we increase the lead size (Fig. 3-5 and the results agree with a simple NEGF calculation (Fig. 3-6) in the low-bias limit. We therefore conclude that these relatively short wires are capable of mimicking the transport properties that would be observed in an a wire attached to much larger (practically infinite) leads. It seems likely that similar conclusions hold for the more experimentally relevant case of molecular junctions, namely, that by simulating the conductance of a molecule attached to large but finite metallic leads, it should be technically feasible to approximate the infinite-lead results with a finite system.

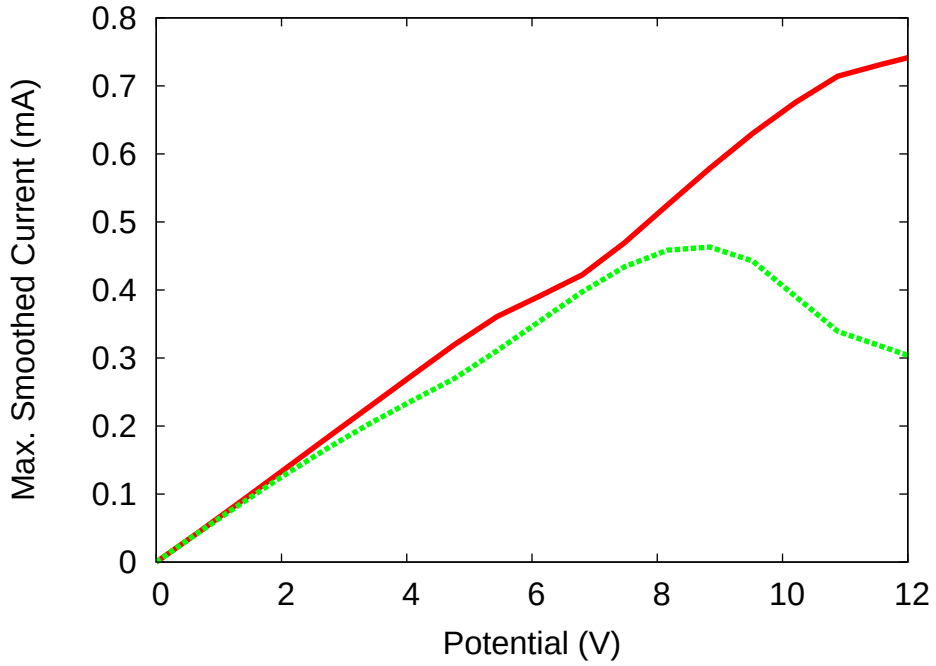

Figure 3-7: Maximum smoothed current through the central four carbons in $C_{50}H_{52}$ as a function of chemical potential bias (red solid line) and voltage bias (green dashed line). The results are very similar at low bias. At larger bias (4 V), the finite width of the valence band causes the voltage bias current to drop off.

3.3.4 Comparison to Voltage Bias

We examine the I-V curve calculated under a voltage bias method to compare with the chemical potential bias calculations we have been studying. Where the chemical potential bias method requires the potential in Fig. 3-2 to be turned *off* at $t = 0$, the voltage bias method requires the opposite potential to be turned *on* at $t = 0$. The current-bias results using both the chemical potential and voltage biases are shown in Fig. 3-7. Clearly, the low bias results are very similar for the two methods as expected. At higher biases (4 V), the voltage bias calculation shows negative differential resistance. This results from the finite width of the π band which prevents the band line-up at larger voltages and is an artifact of the finite basis set. The chemical potential bias produces no such band misalignment, and thus shows no negative differential resistance. We do, however, expect the chemical potential current to level off as the available valence states in the source become saturated at very large

bias.

3.4 Conclusions

In this chapter, we have demonstrated real-time TDDFT simulations of charge transport through a molecular wire at finite bias. In doing so, we have established the local basis set TDDFT method that will be used through the remainder of this thesis. Using *trans*-polyacetylene, we have performed quantitative finite-bias calculations of quantum scale conductance, that show good agreement with the NEGF method in the strong coupling limit. Additionally, we have established some general results of real-time transport. We have demonstrated that the conducting device shows oscillations in transient current which are not artifacts of the stepping procedure. These oscillations require the transient current to be time-averaged to produce a reasonable result for the steady state current. We have verified that for polyacetylene, the currents are converged with respect to lead sized with leads consisting of 23 carbon atoms. Additionally, the long wire calculations verify that the current oscillations are not finite size effects or the result of the numerical integration, but represent a real physical behavior of the system. These oscillations may be a source of inaccuracy in the NEGF/DFT method which relies upon a steady state assumption.

In the remaining chapters we will further explore real time dynamics in systems undergoing electron transport and examine some questions left unanswered in this chapter. We will extend this method to open-shell systems, explore the effects of the various available approximate exchange-correlation functionals, further examine the current oscillations demonstrated here, and apply this TDDFT method to more chemically and technologically relevant systems.

3.5 Acknowledgements

The work in this chapter was performed in collaboration with Chiao-Lun Cheng who is first author on Ref. [140].

Chapter 4

Spin-Charge Separation in Open-Shell Propagations

Note: The bulk of this chapter has been published in Ref. [152].

In this chapter we focus on the phenomenon of spin charge separation in simple molecular wires, namely the fact that the net rates of spin and charge flow through low dimensional systems need not be the same [36, 37, 38, 39, 40, 41, 42, 43, 44, 45, 46, 47, 48]. On the technological side, this effect could be exploited in spintronic devices. On the more fundamental side, spin-charge separation in molecular wires has been of theoretical interest for decades, both in the quantum chemistry community and the solid state community. Within the solid state community, spin-charge separation in low dimensional systems was first proposed by Haldane as a consequence of the Luttinger Liquid model [36]. Several Hubbard Hamiltonian calculations have demonstrated that in one-dimensional systems, spin and charge waves travel at different rates, with charge generally moving more rapidly than spin [37, 38, 39]. These calculations indicate that the dynamics of the up and down spin electrons work together to create effectively independent charge and spin dynamics.

For the specific case of conducting polymers, spin and charge behavior have been studied extensively in the static limit. Work has focused on the creation of spin *or* charge density waves in conjunction with the formation of a soliton, or perturbation of the bond length alternation, in polyacetylene. Solitons were initially described by

Su *et. al.* [153] and further studied by Bredas and Silbey [154, 155, 156, 157, 158] among others [159, 160, 161, 162, 163, 164] using semiempirical calculations. Solitons in polyacetylene cause either spin or density waves depending on the charge of the molecule. In general, it was discovered that the spin density waves are more localized than the charge density waves [156, 157]. While the initial studies examined systems with only spin density waves or charge density waves, recent theoretical [165] and experimental [166, 167, 168, 169, 170, 171] studies have demonstrated both types in coexistence.

Within the transport community, the effects of spin on charge conductance have also come under scrutiny [172]. It has been recognized that spin-restricted calculations can give vastly different currents than spin-unrestricted ones [173, 77], and it is thought these differences may explain at least some part of the hundredfold discrepancy between the theory and experiments for metal-molecule-metal junction conductance. Furthermore, several studies have indicated the importance of the nonlocal exchange interaction in calculating molecular conductance [123, 124, 174, 121, 122, 175]. These DFT studies indicate that the self-interaction error produced by lack of exact exchange and the resulting charge delocalization greatly enhance conductance.

In this chapter, we study the dynamics of spin-charge separation in simple polyacetylene wires using real-time propagation of the quantum wavefunctions. We study both the charge and spin transport due to fundamental interest in the problem and as a test case to examine the impact of various DFT approximations on each type of transport. Our primary results are obtained with TDDFT, but we also resort to a simple PPP model Hamiltonian in order to interpret our results and determine which effects are real and which are artifactual. We find that spin and charge can have significantly different rates of transport, even through these simple molecular wires and neglecting soliton effects. Further, we find that electron-electron interaction and self-interaction error (SIE) have profound impact on the results even at a qualitative level. In particular, we find that the large SIE present in existing density functionals radically changes the spin current characteristics of these wires. Finally, we discuss the implications of these findings for future simulations.

4.1 Methods

4.1.1 Systems

As in chapter 3 [140], we focus on the polyacetylene molecular wire $C_{50}H_{52}$ as a simple example of a conjugated molecule that supports electron transport. The system division mirrors Fig. 3-2 in that the central four carbon atoms are defined as the device giving a source–device–drain division of $C_{23}H_{24}$–C_4H_4–$C_{23}H_{24}$. We use the 6-31g* basis set and either Hartree-Fock (which contains 100% exact exchange but no correlation) or the B3LYP functional (which contains some correlation but only 20% exact exchange). All DFT calculations were performed using a local version of Q-Chem [176]. Unlike in chapter 3, we simulate the cation ($C_{50}H_{52}^{+}$) and the anion ($C_{50}H_{52}^{-}$) rather than the neutral chain. Since these chains now contain an *odd* number of electrons the system will have a net spin polarization and we can independently consider the rates of spin and charge transport through the wire as the voltage is applied.

4.1.2 Real-Time Density Functional Conductance Simulations

The all-electron conductance is calculated in the real-time propagation method (section 1.5) with TDDFT (chapter 3). Because we have previously describe this method, we here describe only the details that change for this chapter.

The primary difference between this chapter and chapter 3 is the use of open- rather than closed-shell quantum chemistry methods. The TDKS equation (3.1) for the open shell system becomes

$$\begin{aligned} \hat{H}\left[\rho^{\uparrow},\rho^{\downarrow}\right]_{KS}^{\uparrow}\psi_a^{\uparrow}(t) &= i\hbar\frac{\partial\psi_a^{\uparrow}(t)}{\partial t}, \\ \hat{H}\left[\rho^{\uparrow},\rho^{\downarrow}\right]_{KS}^{\downarrow}\psi_a^{\downarrow}(t) &= i\hbar\frac{\partial\psi_a^{\downarrow}(t)}{\partial t}, \end{aligned} \tag{4.1}$$

where $\rho^{\uparrow(\downarrow)}(t) = \sum_{a\ occ.}\left|\psi_a^{\uparrow(\downarrow)}(t)\right|^2$. The details of the numerical propagation scheme remain the same save for the fact that we must apply the scheme to both spin den-

sity matrices. Equation 4.1 propagates each spin channel separately (i.e. it is spin unrestricted) and the propagations are coupled, because the effective Hamiltonians depend on both the ↑ and ↓ densities simultaneously. We examine properties that can be described using the total density difference ($N_{tot}(t)$) and spin density difference ($M_{spin}(t)$) in the source and drain. We define $N_{tot}(t)$ and $M_{spin}(t)$ as

$$N_{tot} = \left(n_S^{\uparrow} + n_S^{\downarrow}\right) - \left(n_D^{\uparrow} + n_D^{\downarrow}\right), \tag{4.2}$$

$$M_{spin} = \left(n_S^{\uparrow} - n_S^{\downarrow}\right) - \left(n_D^{\uparrow} - n_D^{\downarrow}\right), \tag{4.3}$$

where the variables $n_S^{\uparrow}(t)$, $n_D^{\uparrow}(t)$, $n_S^{\downarrow}(t)$, and $n_D^{\downarrow}(t)$ are the up (↑) and down (↓) spin analogues of the time dependent populations (equation 1.37) with the Löwdin population definition. While we previously calculated only charge current, we here calculate transient currents both for total charge ($I_{tot}(t)$) and spin ($I_{spin}(t)$) according to the open shell analogue of equation 3.7,

$$I_{tot}\left(t\right) = \frac{N_{tot}\left(t + \Delta t/2\right) - N_{tot}\left(t - \Delta t/2\right)}{2\Delta t}, \tag{4.4}$$

$$I_{spin}\left(t\right) = \frac{M_{spin}\left(t + \Delta t/2\right) - M_{spin}\left(t - \Delta t/2\right)}{2\Delta t}, \tag{4.5}$$

where N_{tot} and M_{spin} are defined by equations 4.2 and 4.3. For this chapter, $\Delta t = 0.48$ fs, which is close to the value chosen in chapter 3. We use the maximum current definition from that chapter to choose a single current for each propagation as well.

While the potential in this chapter is defined according to a chemical potential bias, we often describe the initial state of the system by population distribution rather than potential profile. The initial state of the system is determined by constrained DFT [85, 86]. We want to control the values of N_{tot} and M_{spin} defined in equations 4.2 and 4.3. For each of $n_S^{\uparrow}$, $n_D^{\uparrow}$, $n_S^{\downarrow}$, and $n_D^{\downarrow}$ in the above equations, we can define an associated operator - $\hat{n}_S^{\uparrow}\left(\mathbf{r}\right)$, $\hat{n}_D^{\uparrow}\left(\mathbf{r}\right)$, $\hat{n}_S^{\downarrow}\left(\mathbf{r}\right)$, $\hat{n}_D^{\downarrow}\left(\mathbf{r}\right)$ - that measures the appropriate number of electrons using the Becke weight definition. This is similar to equation 1.15. We use a different population definition here only due to software availability. We define operators $\hat{N}_{tot}\left(\mathbf{r}\right) \equiv \hat{n}_S^{\uparrow}(\mathbf{r}) + \hat{n}_S^{\downarrow}(\mathbf{r}) - \hat{n}_D^{\uparrow}(\mathbf{r}) - \hat{n}_D^{\downarrow}(\mathbf{r})$ and $\hat{M}_{spin}\left(\mathbf{r}\right) \equiv \hat{n}_S^{\uparrow}(\mathbf{r}) -$

$\hat{n}_S^{\downarrow}(\mathbf{r}) - \hat{n}_D^{\uparrow}(\mathbf{r}) + \hat{n}_D^{\downarrow}(\mathbf{r})$ and associate with each a Lagrange multiplier - $\frac{V_{tot}}{2}$ or $\frac{V_{spin}}{2}$. The factor of $\frac{1}{2}$ makes our potential definition consistent with our previous chapters and Fig. 3-2. Our desire is to find an initial state that has a prescribed set of N_{tot} and M_{spin} values. We enforce this by extremizing

$$W\left[\rho, V_{tot}, V_{spin}\right] = E\left[\rho\right] - \frac{V_{tot}}{2}\left(\int \hat{N}_{tot}(\mathbf{r})\rho(\mathbf{r})d\mathbf{r} - N_{tot}\right) - \frac{V_{spin}}{2}\left(\int \hat{M}_{spin}(\mathbf{r})\rho(\mathbf{r})d\mathbf{r} - M_{spin}\right), \quad (4.6)$$

where $E\left[\rho\right]$ is the DFT energy functional (equation 2.18), and each subsequent term enforces one of the particle number constraints. Due to the conjugate relationship between the numbers and their Lagrange multipliers we can use either a chemical potential (e.g. V_{tot}) or a number (e.g. N_{tot}) as our independent variable in what follows. In choosing initial conditions, we choose systems with integer values of N_{tot} and M_{spin}.

4.1.3 Empirical Model Hamiltonians

To interpret our results, we found it useful to fit our TDDFT data to simple, parameterized, semiempirical Hamiltonians representing the conjugated π backbone of our molecule. These techniques have been used extensively to study charge transport in organic molecules in the past[69, 70, 177, 178, 179]. The difference here is that in our calculations, the model parameters are determined *post hoc* from the DFT data. Thus, the model Hamiltonian is tailored to give a charge transfer energy landscape that is as close as possible to the TDDFT results. The goal is to develop a simplified system that displays similar behavior to the DFT simulations described above. However, by reducing the number of degrees of freedom, we are able to perform calculations *much more quickly* allowing us to test, for example, a larger range of voltages, and to better understand the physics involved.

We use the Pariser-Parr-Pople (PPP) Hamiltonian [136, 137] with electron-electron interaction defined by the Mataga-Nishimoto [138, 139] formula as described in sec-

tion 2.7. To model the 50 carbon chain under study, we set the site-site separation as $r_{j,k} = r_0 |j - k|$ where $r_0 = 2.647$, the carbon-carbon separation in benzene. The number of sites is $N = 50$, and we model the anion or cation by considering 51 or 49 electron systems respectively. We allow only adjacent site hopping ($\beta_{jk} = \beta(\delta_{j+1,k} + \delta_{j-1,k})$) and use only one on-site electron repulsion parameter for all sites ($g_{jk} = g$). The values of β and g are set as parameters.

We calculate currents in the PPP model using a method analogous to that used for our TDDFT calculations: An initial nonequilibrium state is prepared in the presence of independent chemical potentials on the leads, and the potentials are released at time $t = 0$. The system is propagated via time dependent HF,

$$\begin{aligned} \hat{F}^{\uparrow}[\mathbf{P}]\,\psi^{\uparrow}(t) &= i\hbar\frac{\partial\psi^{\uparrow}(t)}{\partial t}, \\ \hat{F}^{\downarrow}[\mathbf{P}]\,\psi^{\downarrow}(t) &= i\hbar\frac{\partial\psi^{\downarrow}(t)}{\partial t}, \end{aligned} \tag{4.7}$$

where $\hat{F}^{\uparrow}[\mathbf{P}]$ and $\hat{F}^{\downarrow}[\mathbf{P}]$ are the Fock operators from equation 2.41. This equation is very similar to TDKS (equation 4.1). The propagation is performed with the second order Magnus method [140], populations $\{n_S^{\uparrow}(t), n_S^{\downarrow}(t), n_D^{\uparrow}(t), n_D^{\downarrow}(t)\}$ are determined by the Löwdin definition, and currents are determined by equations 4.4 and 4.5.

Several variations of the Hamiltonian and parameters will be useful in what follows. In particular, we will introduce self-interaction error (SIE), described in section 2.6.5, into the PPP model (PPP-SIE). SIE arises when coulomb repulsion is not exactly canceled by an approximate exchange interaction, so there is always some residual SIE in a functional like B3LYP. To introduce analogous SIE into the PPP model, we multiply the exchange component of the PPP energy (equation 2.40) by a_X =0.5 so that the exchange and Coulomb pieces no longer cancel. Additionally we performed PPP model calculations in the Hartree (PPP-Hartree, $a_X = 0$) and Hückel ($g \to 0$) approximations which neglect, respectively, all exchange and all electron-electron repulsion.

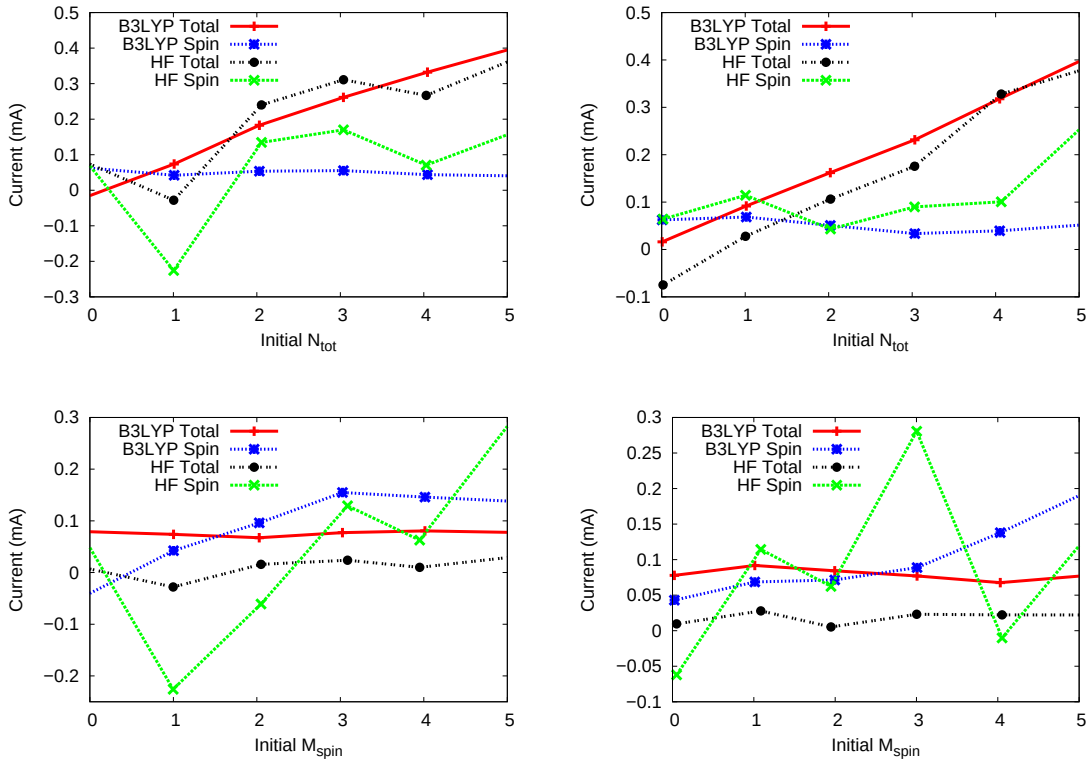

Figure 4-1: Plot of I_{tot} and I_{spin} as a function of initial N_{tot} and M_{spin} as determined using B3LYP or HF for the anion (left) and cation (right) case. The value of the fixed initial M_{spin} or N_{tot} is set to 1.0. B3LYP produces more linear current profiles than HF due to a reduction in exact exchange. Likewise, spin current profiles are less linear than charge current profiles because spin is more sensitive to exact exchange.

4.2 Results

4.2.1 Real-Time TDDFT Currents

In Figure 4-1 we present the TDB3LYP and TDHF spin and charge currents as a function of initial N_{tot} with fixed initial $M_{spin} = 1$ and as a function of initial M_{spin} with fixed initial $N_{tot} = 1$. We choose to present currents as a function of initial distribution to directly compare charge and spin behavior even though this choice does not allow a direct calculation of conductance. Focusing first on the DFT results, we see that the charge current increases nearly linearly with the initial N_{tot}. Under the same circumstances, spin current is nearly constant showing only very small dependence on initial N_{tot}. Also as expected, the spin current generally increases

with increased initial M_{spin}. However, for spin the trend is much less linear than it is for charge. We see non-zero spin currents for initial $M_{spin} = 0$. Although this is initially surprising, we must remember that the propagation is not beginning from an equilibrium initial state because $N_{tot} \neq 0$, so some spin motion can be expected. Finally, just as N_{tot} weakly influenced spin current, so M_{spin} has little effect on the charge current.

The B3LYP results in Figure 4-1 agree with known properties of spin-charge separation. For the case of $M_{spin} = N_{tot} = 1$, the charge current is larger than the spin current. This occurs despite the fact that the initial charge and spin differences are equivalent. Similarly, the total current for a particular value of N_{tot} is larger than the spin current for that value of M_{spin}. For example, for $M_{spin} = N_{tot} = 1$ we have $I_{tot}/I_{spin} = 1.7$ for the anion and $I_{tot}/I_{spin} = 1.3$ for the cation. This behavior has been shown previously in correlated systems [37, 38, 39]. In correlated calculations, one measures charge and spin wave velocity in the Hubbard model to give $v_{tot}/v_{spin} = 1$ with no onsite electron-electron interaction ($g = 0$) and $v_{tot}/v_{spin} \approx N_e$ with large onsite electron-electron interaction ($g \geq 10\beta$) where N_e is the number of electrons. As we will see in section 4.2.2, the B3LYP propagation is best modeled with $g = 3.4\beta$. Thus, the charge-spin current ratio falls between the zero electron-electron repulsion and the large repulsion limit as we expect.

Turning our attention to the Hartree-Fock calculated currents, we note that both the spin and charge currents calculated with the Hartree-Fock functional fluctuate more as a function of particle number than those calculated with B3LYP. We will see in section 4.2.3 that these fluctuations result from exact exchange in the HF functional. While the nonmonotonic nature of the data makes determining trends for the spin currents impossible with the data available, the charge currents approximately follow the trends established by B3LYP. We note that, while previous investigations have demonstrated the effect of HF exchange on the *magnitude* of the current predicted at low bias[123, 122, 124, 180], to our knowledge this is the first example of the effect of HF exchange on the qualitative shape of the current-bias curve.

4.2.2 Obtaining Model Hamiltonian Parameters

We have empirically fit the PPP model parameters, β and g, to reproduce the equilibrium behavior of DFT under various chemical potential biases. The parameters are adjusted until the two methods show approximate agreement for the values of N_{tot} and M_{spin} over the range $-8 < V_{tot} < 8$ and $-1.5 < V_{spin} < 1.5$. Note that we are using PPP as an interpretive tool, rather than a quantitative analysis technique. Thus, we adjust β and g by visual inspection and do not concern ourselves with numerical fitting. The fitting for two different parameters is aided by the empirical observation that g primarily influences the slope of the N_{tot} versus V_{tot} plot while only β affects the slope of M_{spin} versus V_{spin}. The parameters chosen are $\beta = 0.16$ and $g = 0.55$. These values are not too far off the values of $\beta = 0.0878$ and $g = 0.398$ suggested by Mataga and Nishimoto[139]. The charge and spin number versus potential plots for the cation and anion are shown in Figure 4-2. Clearly the parameters chosen give the correct overall slope to these plots. Furthermore, the step-like nature of HF is reproduced by PPP. However, the B3LYP results show smooth dependence of N_{tot} on V_{tot} while PPP and HF produce steps. We note that the step-like behavior of PPP was not influenced in any way by the parameter choice.

The reason for the differences between PPP and B3LYP is relatively simple: for PPP one is using an SIE-free Hartree-Fock (HF) prescription for the energy, while B3LYP includes spurious self-interaction terms. This distinction is important because it has been shown that SIE can have a profound effect on charge transfer, current dynamics and spin states [181, 121, 87]. The same is true in this case, as artificially reducing the exchange term in PPP by 50% (PPP-SIE) improves agreement with B3LYP in the static, potential-dependent N_{tot} and M_{spin}. The PPP-SIE method produces nearly linear results for total density, and step behavior for the spin density in agreement with B3LYP. We have run similar calculations with PPP-Hartree (0% exact exchange) and find near-linear particle number versus potential behavior for *both* charge and spin. On the other hand, Figure 4-2 shows that full PPP (100% exchange) produces steps for both total and spin density. Only with *partial* cancellation of the

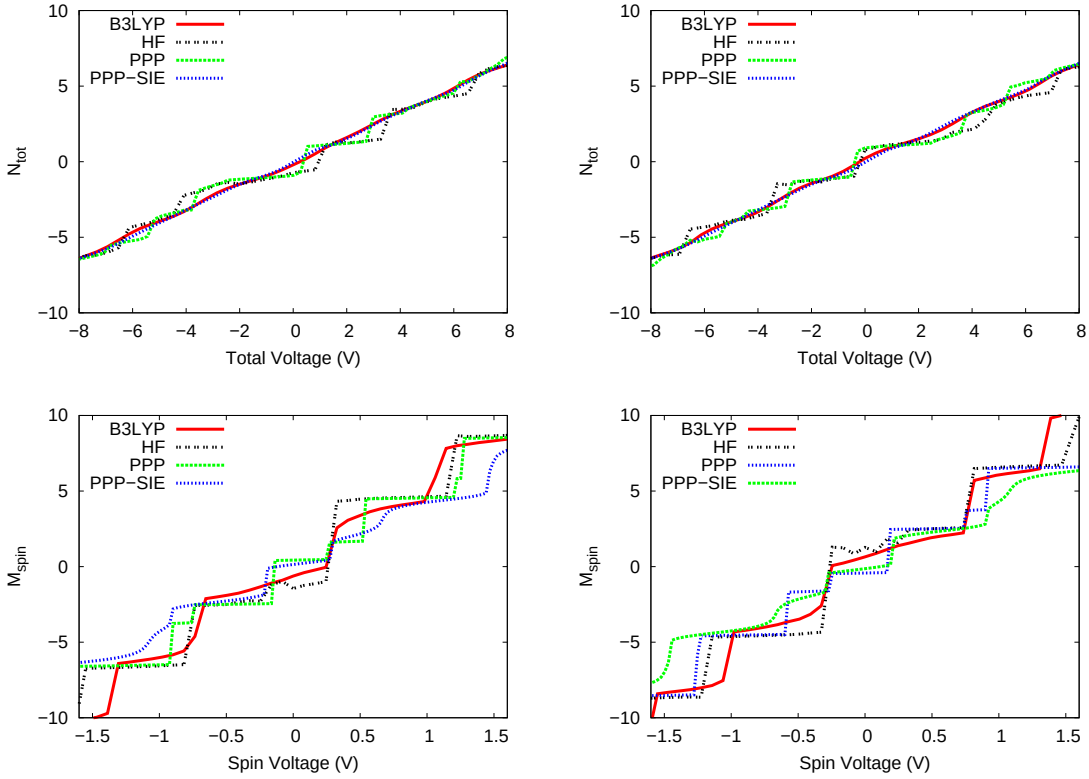

Figure 4-2: Dependence of N_{tot} upon V_{tot} with $V_{spin} = 0.272V$ and M_{spin} upon V_{spin} with $V_{tot} = 1.36V$ for the anion (left) and cation (right) as predicted by B3LYP, PPP, and PPP-SIE. The stair-step nature of the N_{tot} and M_{spin} profiles increases with decreasing exact exchange and the spin profiles are more step-like than charge profiles.

SIE (as with PPP-SIE) can we obtain qualitative agreement with the B3LYP data.

The self-interaction induced smoothing of the N_{tot} versus V_{tot} steps has previously been reported by Baer et al for weakly coupled subsystems [182] and is known to reflect the tendency of SIE to favor for charge delocalization. Here we see that these steps persist even in a molecular wire that is strongly coupled to the leads. Steps also occur for spin distribution, reflecting *spin* localization as well. The small amount of exact exchange in B3LYP predicts the unusual situation of spin *localization* together with charge *delocalization*. This unusual localization-delocalization situation is closely coupled to the transport predictions of the previous subsection [180].

4.2.3 Model Hamiltonian Currents

The PPP current versus number plots are shown in Figure 4-3. As expected from the static calculations in Section 4.2.2 the full PPP currents resemble those calculated by HF while PPP-SIE gives much better qualitative agreement with B3LYP. In addition to PPP-SIE ($a_X = .5$), PPP-Hartree (a_X=0) and Hückel ($g \rightarrow 0$) results are also included in Figure 4-3. We first examine the charge currents. With PPP-SIE, charge currents increase essentially monotonically while the PPP calculated current profile fluctuates. Furthermore, we notice that PPP-Hartree and PPP-SIE agree almost quantitatively for charge currents. This suggests that below a certain threshold (i.e. with less than 50% exchange), exchange has little impact on charge current. From the comparison of Hückel and PPP-Hartree we also see that removing the Coulomb interaction significantly reduces charge current, so that a non-interacting picture of these wires is inadequate.

Considering spin properties, we see that for PPP-SIE, there is only one small region of non-monotonic behavior (in the anion spin current plot at initial $M_{spin} = 1$). On the other hand, PPP produces fluctuating spin current profiles such that even determining a trend is difficult. Meanwhile, the spin current plots are nearly identical for PPP-Hartree and Hückel propagation. Thus, we see that the exchange interaction is much more important than the Coulombic interaction in determining spin transport. The importance of the exchange piece over the Coulomb piece can be

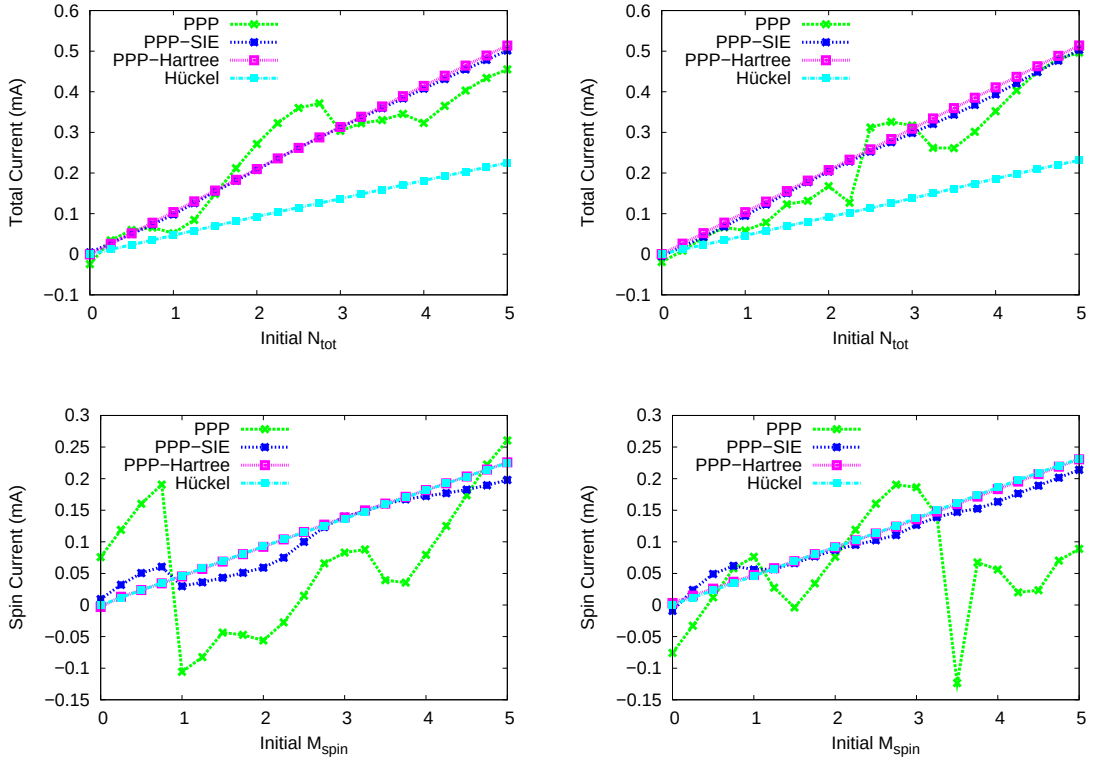

Figure 4-3: Maximum total and spin currents plotted against initial N_{tot} and M_{spin} respectively as calculated by PPP, PPP-SIE, PPP-Hartree, and Hückel propagation for the anion (left) and cation (right). The unvaried initial N_{tot} or M_{spin} is held to 1.0. The model results qualitatively mirror the all-electron results when the fraction of exact exchange is adjusted to reflect the DFT exchange-correlation functionals.

explained by realizing that the coulomb interaction acts between any two electrons regardless of spin while the exchange interaction only acts between electrons of the same spin. Thus, changing the spin density while allowing the charge density to remain the same by switching an up and down spin electron will change exchange energy, but not Coulomb. We thus see that the phenomenon of spin-charge separation is inextricably linked to the description of electronic exchange. The deep connection between spins and currents in TDDFT has been addressed previously in a completely different context [183, 184].

Examining the time series data (not shown) reveals that a major source of the erratic current behavior in PPP and HF is that these full exchange propagations do not always relax towards symmetric charge and spin distributions. As an example, for the anion with initial $N_{tot} = M_{spin} = 1$, Hartree-Fock predicts relaxation towards $N_{tot} \approx 1$ and $M_{spin} \approx 2.3$ resulting in near 0 charge current and negative spin current as shown in Figure 4-1. This unusual behavior does not occur with B3LYP or PPP-SIE. The tendency of exact exchange methods to relax towards broken symmetry charge or spin densities is likely related to the step-like behavior of the N_{tot} and M_{spin} dependence on $V_{tot/spin}$ in that both seem to indicate local minima in the electronic potential energy surface other than the symmetric distribution. Indeed, such charge and spin localization are known to be favored by exact exchange.

4.3 Discussion

Note that the PPP model is computationally inexpensive, so we can perform analogous calculations on much longer wires, allowing us to approach the thermodynamic limit. To demonstrate this, we show in Figure 4-4 the PPP-SIE calculated current versus potential plots for the carbon chains of length 50, 100, and 200 with a fixed molecule segment of 4 sites. We have chosen potential rather than number as our independent variable because the former is size intensive, facilitating the comparison of different length chains. For both the charge and spin plots, the slopes remain the same with increasing chain length, converging to a junction conductance of about

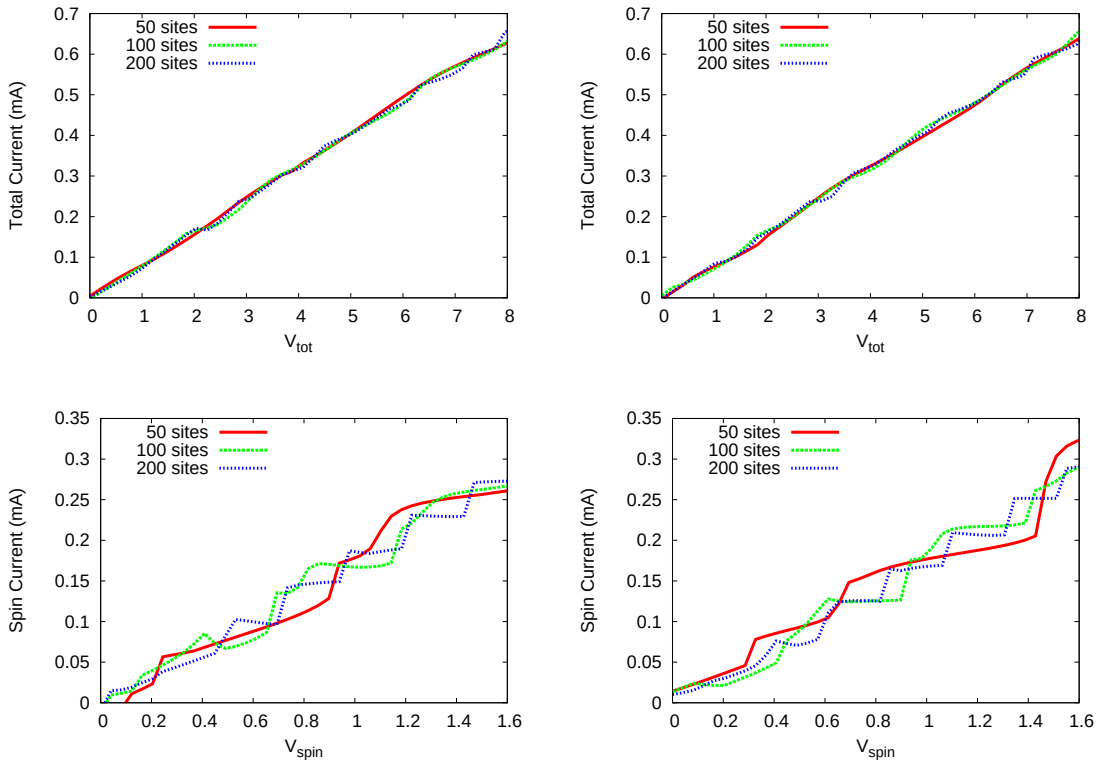

Figure 4-4: Maximum total and spin currents plotted against initial V_{tot} and V_{spin} respectively as calculated by PPP-SIE, for chains of length 50, 100, and 200 sites. The fixed initial potentials are $V_{spin} = 0.272V$ for the total current plots and $V_{tot} = 1.36V$ for the spin current plots. These calculations indicate the ease with which we can approach the thermodynamic limit in the model system.

$0.5G_0$ for charges, but $1.2G_0$ for spins, in qualitative agreement with previous simulations [140]. We thus see the unusual fact that while an *individual* spin moves more slowly than an individual charge by a factor of $I_{charge}/I_{spin} \approx 1.3 - 1.7$ (vide infra) yet the molecular conductivity for spins is higher because less potential needs to be applied to separate spins as opposed to charges.

Another interesting point is that increasing chain length produces more closely spaced steps in the IV plot. This can be explained by considering that an increase in chain length means that a given potential transfers more whole electrons from one side to the other creating more steps. These results suggest that one may regain a smooth spin IV curve in the infinite chain limit. We could easily repeat these calculations using any of our PPP methods, but at the moment we simply wish to demonstrate that large chain calculations are possible with the model Hamiltonian used in this study.

The TDDFT calculations presented in this paper suggest that for one-dimensional systems, charge and spin do indeed behave as separate quasiparticles. This separation is seen most clearly in that, for B3LYP, charge transport occurs more quickly than spin transport from analogous initial states in agreement with the results of correlated, real time model system simulations [37, 38, 39]. Hartree-Fock shows large fluctuations in the current profiles for charge and spin, making it difficult to assess which quasiparticle travels more quickly. Similarly, spin and charge show different particle number versus potential behavior as seen in Figure 4-2. Both the greater step behavior in Figure 4-2 and reduced transport properties of spin relative to charge relate to the greater localization of spin over charge demonstrated in studies of density waves caused by solitons [156, 157]. The tendency of charge to delocalize increases the probability of partial charges on the right and left leads of the system. Furthermore, the same forces that cause electrons to delocalize also cause charge to travel more quickly than spin.

We have demonstrated real-time transport calculations in which DFT with the B3LYP functional and Hartree-Fock produce qualitatively different results. This presents an interesting exploration opportunity because density functional theory and Hartree-Fock both present certain advantages for predicting transport. It is well

known that Hartree-Fock is free of self-interaction-error. Several previous studies have indicated that removing SIE may also significantly reduce electron transport across a molecular device [123, 122, 124]. Given the often one to two orders of magnitude overestimate of charge currents from existing DFT calculations, one would thus be tempted to conclude that a method like HF might offer some distinct advantages. On the other hand, Hartree-Fock clearly lacks important pieces of the Hamiltonian. The single-determinant picture includes no correlation, while modern density functionals contain at least an approximate correlation energy. These semilocal correlation functionals allow modern DFT to predict energies with surprising accuracy, even in the presence of SIE. The cancellation of errors which leads to accurate equilibrium properties in DFT may also contribute to accuracy in transport simulations. Specifically, it is known that describing density of state alignment between the leads and device is very important in describing transport properties [174]. Furthermore, recent studies [123] indicate that Hartree-Fock greatly overestimates the HOMO-LUMO gap resulting in artificially reduced conductance properties, while B3LYP provides more consistent energy gaps, potentially leading to more reliable currents. In order to resolve which method is actually closer to reality for these systems, one would really need to perform correlated *ab initio* calculations. Such simulations are outside the scope of this work, but would certainly advance the field.

The questions posed in regards to the impact of exchange and correlation on modeling transport are critical due to the large difference between theory and experiment in these studies. Numerous potential sources of this difference exist. Those sources include self-interaction-error from less than 100% exact exchange as discussed in this chapter or correlation effects. Additionally, recent theoretical evidence [185] indicates the powerful impact that contact atomic geometry can have on the electronic transmission function, and therefore conductance. NEGF methods may also develop errors in the use of an equilibrium single particle Fock matrix as a substitute for the non-equilibrium many particle Hamiltonian. With all these potential sources of error, it is necessary to clarify the impact of each of these approximations.

Our work clarifies the differences in *both* charge and spin behaviors when calculated

with 100% exact exchange (Hartree-Fock, PPP) compared to calculations with less than 100% exact exchange (B3LYP, PPP-SIE). With exact exchange, we see results associated with localization, while introducing SIE tends to favor delocalized, partial charge and spin states. In particular, we see that localization effects are enhanced in spin transport simulations relative to charge transport. We propose this sensitivity of spin transport properties can act as a measure of how well exchange properties are described by a particular method.

4.4 Conclusions

We have analyzed real-time spin and charge currents through polyacetylene wires using TDDFT. Our calculations agree that spin and charge do indeed behave as separate particles, with charges moving faster than spins by a factor of between 1.3 and 1.7. We find that the spin dynamics in particular are critically sensitive to the nonlocal exchange interaction, as TDB3LYP and TDHF show qualitatively different behavior for the spin dynamics. The former shows a smooth, essentially monotonic increase in spin current as the initial M_{spin} is increased, while the latter shows fluctuational and even negative currents as a function of M_{spin}. Meanwhile, the charge currents are primarily modulated by the strength of the classical Coulomb repulsion. We find empirically that the TDB3LYP dynamics can be well-reproduced by a simple PPP model if we artificially introduce some self-interaction error into the PPP model by reducing the amount of nonlocal exchange by 50%. Conversely, PPP without SIE reproduces the fluctuating behavior of TDHF. Thus, we see that methods with 100% exact exchange give qualitatively different results as regards spin/charge separation from those with some amount of self-interaction. The enhanced influence of the exchange force on the shape of the spin current-voltage curve has not previously been noted and we propose that this could be a powerful tool for calibrating exchange-correlation functionals for transport calculations.

These results call into question the accuracy of using existing functionals for the prediction of currents in open shell systems and may help explain the erroneously

large currents predicted in metal-molecule-metal junctions. Few functionals include 100% exact exchange which seems to significantly impact charge and especially spin transport. On the other hand, Hartree-Fock, which includes exact exchange, does not include correlation. It is unclear how the inclusion of both exact exchange and correlation will impact our transport results, but the two effects together may give much better agreement with experiment than we have so far seen in single-molecule charge transport calculations. In chapter 5, we will study in more detail the influence of the choice of functional, and hence the degree of SIE, on currents.

4.5 Acknowledgements

The work in this chapter was performed in collaboration with Chiao-Lun Cheng who is an author on Ref. [152].

Chapter 5

Importance of Non-local Exchange and Correlation

In the previous chapters [140, 152], we used real-time TDDFT to study transport in molecular wires using common approximations to the exchange-correlation (xc) functional. We have demonstrated, in agreement with several other studies [123, 124, 174, 121, 122, 175], the sensitivity of both spin and charge currents to the choice of xc functional. Unfortunately, common approximations in TDDFT do not form a convergent hierarchy, so that it is not possible to say with certainty that one functional gives uniformly better results than another. Thus, the wide variety of predictions obtainable with standard TDDFT makes it practically impossible to identify which functionals, if any, give an accurate description of transport. This ambiguity is particularly acute given that simulations and experiments in this field often disagree by one to two orders of magnitude [121, 122]. The situation can be ameliorated by using wavefunction-based techniques [71], but because the microcanonical picture requires such calculations be performed on the entire molecule+leads system - often containing several hundred atoms - correlated *ab initio* investigations along these lines are simply not feasible. One is thus left with significant uncertainty as to the best way to simulate electron transport in molecular junctions.

In this chapter, we critically examine a number of approximate microcanonical simulations to determine which ingredients are required to obtain electron transport

dynamics. We focus on a single model system(see Fig 5-1), but vary the model chemistry under which it is described.. First, we simulate the conductance using a variety of semilocal and hybrid density functionals and find that the predicted current-voltage curves depend *only* on the fraction of non-local Hartree-Fock exchange included in the functional. The presence or absence of semi-local correlation has a negligible effect on the system at any bias. This is consistent with the fact that, at zero bias, the resistance only depends on the infinite-ranged part of the xc potential [122, 56]. To assess the impact of non-local wavefunction-based correlation on transport, we make use of the computationally simple Pariser-Parr-Pople (PPP) model Hamiltonian described in section 2.7. We then employ the generator coordinate method (GCM) to rapidly incorporate non-local correlation within the model space. We find that non-local correlation has a negligible effect on transport in the ballistic regime, but significantly increases the transport gap. This behavior is not reproduced by any of the semilocal xc functionals we have tested. We therefore conclude that, at a fundamental level, non-locality is required in both the exchange *and* correlation functionals if one wants to obtain an accurate description of transport. The article concludes with some discussion of the physical implications of these results.

5.1 System and Methods

All the calculations presented in this article concern the model junction depicted in Figure 5-1. This molecule closely resembles the *trans*-polyacetylene studied in chapters 3 and 4. Like the previous chapters, the leads are represented by long conjugated *trans*-polyenes, this time containing 48 carbon atoms each. However, the molecular device is a *trans*-butadiene residue, connected to the leads via two saturated CH_2 segments. Unlike chapters 3 and 4, the system is designed in such a way that the coupling of the molecular device to the leads is rather weak. The conjugation is interrupted by the CH_2 groups, leading to poor overlap of the π orbitals. Although the chain of C–C σ-bonds is not interrupted, the electrons in the σ-orbitals are typically much less mobile.

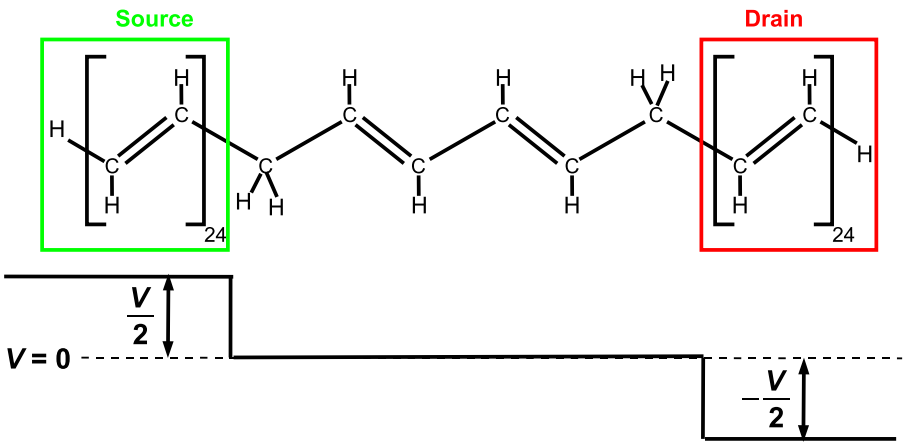

Figure 5-1: Chemical structure representation of the model system and the voltage bias. The saturated linking groups destroy the planar nature of the system, so the full geometry is not shown.

In this chapter, we make use of the *voltage* bias definition of the time-dependent potential in which the ground state of the unperturbed system is subjected to a Löwdin population defined potential bias for times $t \geq 0$. The potential profile corresponding to a voltage V, shown in Fig. 5-1, is opposite to the chemical potential in Fig. 3-2. Like in previous chapters, we record the time-dependent charge difference between the drain and source leads $(n_D(t) - n_S(t))$ and use it to determine current via equation 1.40. However, for this chapter, rather than choose the maximum smoothed current, we use the slope of the linear fit to $n_D(t) - n_S(t)$ in the steady-state region. The charge-difference dynamics in 5.1 indicate that the steady state lasts much longer than in chapter 3. As long as the leads are chosen to be large enough, it is only at much longer times that the current through the wire reverses itself (e.g. around 15 fs in Figure 5.1 rather than 2 fs in chapter 3). We can see this by comparing the dynamics to the linear fit line which is fit over 1 to 5 fs. The longer steady state result from the weakened coupling reducing that rate at which the charge difference can equilibrate. We can see that like the current method in chapters 3 and 4, there is some statistical uncertainty in choosing the current of these finite systems. For example, in Figure 5.1 one would obtain a slightly different current if one fitted from 5 fs to 10 fs than if one fitted from 1 fs to 5 fs and neither result could be considered wrong. It has been shown

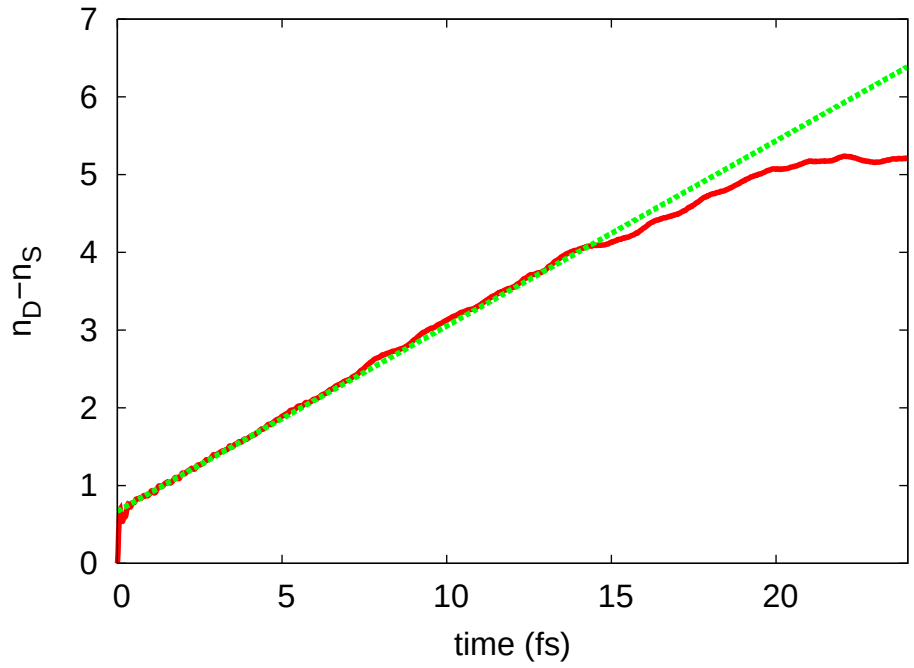

Figure 5-2: Time dependent charge difference between the drain and source in the model junction. The system begins in the ground state and a bias is applied at time zero. After a transient period of a few hundred attoseconds, a quasi-steady state is achieved. This steady state lasts until the charge in the leads is depleted at around 15 fs. Steady state currents can be obtained from the linear fit slope of $n_D - n_S$ vs. t as illustrated by the broken line. These results are with TD-LDA and a voltage bias of 5.44 V, but similar physics prevails for all methods in this article.

recently [83, 140, 186] that with existing computational resources, these numerical uncertainties can be minimized so that the currents obtained in this microcanonical picture are a faithful representation of the true steady state currents. Further, the use of a linear fit rather than a maximum current or average current method should help to limit current dependence upon local oscillations or chosen endpoints.

The entire current-voltage profile is obtained by performing propagations at several potentials and separately fitting each to determine current. This procedure was previously illustrated in Fig. 1-3. At this point it is important to realize that the only *uncontrolled* approximation we make in this procedure relates to the level of electronic structure theory we use to determine and propagate the initial state. The focus of what follows, then, is the impact of approximations to the electronic structure on the predicted currents. In particular, we will focus on determining the correct I-V curve for our model wire and establish what level of theory one needs to employ to get the right answer.

5.2 Real-Time Density Functional Conductance Simulations

The real time density propagation is performed via second order Magnus numerical solution to the TDKS as described in sections 3.1, and 3.2[140]. Calculations were performed on a local version of Q-Chem [176].

All practical DFT methods for molecular conductance rely on common approximations to the exchange-correlation (xc) energy. The particular choice of the xc functional has been shown to dramatically affect the results of conductance calculations [121, 182, 123, 173, 174, 187]. This existing work has primarily been focused on the low-bias behavior, but two important conclusions can be drawn. First, the self-interaction error (SIE) present in commonly employed local and semilocal xc functionals is extremely harmful for conductance simulations. As a direct consequence of SIE, semilocal functionals erroneously predict metallic transport even in insulating

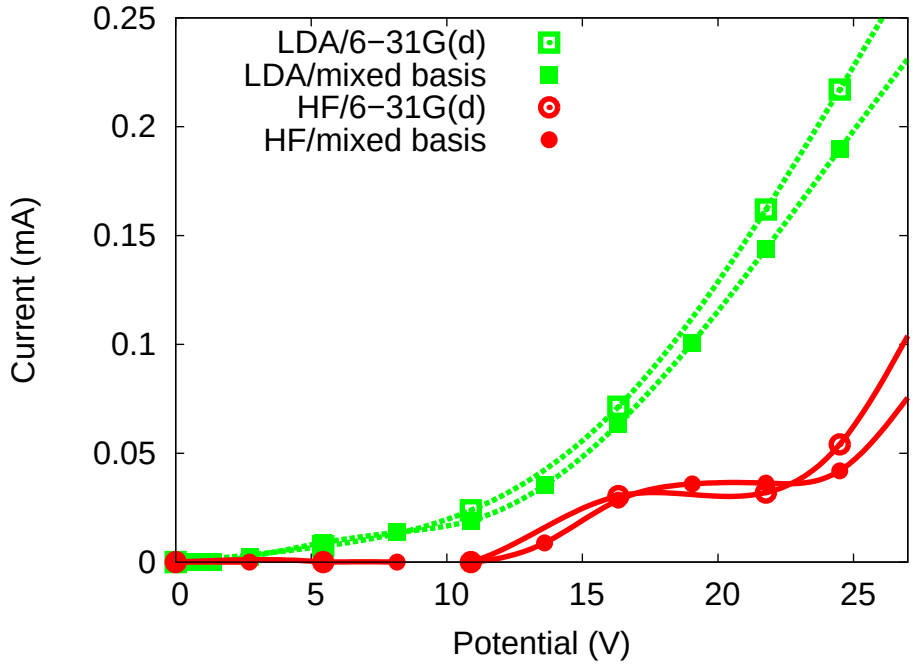

Figure 5-3: Comparison of the I-V curves obtained using the 6-31G* basis set on the entire system with the I-V curves obtained using a mixed basis set (STO-3G on the leads, 6-31G* elsewhere).

molecules in weak contact with the leads [121, 174, 187]. At the same time, it can be shown that at zero bias the xc contribution to the conductance depends only on the induced shift in v_{xc} infinitely deep in the leads [122, 56]. For a semi-local functional, this shift must be zero because the density deep in the leads is unaffected by the effective bias. Thus, at low bias, one expects a semilocal correction to v_{xc} to have negligible effect on the transport. In order to address these issues, we have performed real time TDDFT simulations on the model junction with a variety of functionals that differ in the ways they incorporate non-locality and SIE.

For the test system shown in Fig. 5-1 and using the methodology described in Section 5.1, we compute the I-V curves using four different electronic structure methods: 1) the local density approximation (LDA) 2) a global hybrid of LDA with 50% of the Hartree-Fock-type exchange, which we call "Half&Half" 3) Hartree-Fock (HF) theory and 4) long-range corrected LDA (LC-LDA) which combines the short-range LDA exchange[117, 118] with the long-range HF exchange. In LC-LDA, the standard error

function is used to split the Coulomb operator into short- and long-range parts, and the range-separation parameter $\omega = 0.5$ Bohr^{-1} is used which has been shown to work well in many cases [119, 120]. The LDA, Half&Half, and LC-LDA xc functionals all include the uniform electron gas correlation functional of Vosko, Wilk and Nusair[112] commonly known as VWN5.

We have optimized the geometry of the junction with B3LYP/6-31G*. To save time in the conductance simulations, most of our calculations use the minimal STO-3G[96] basis set for the leads and a larger 6-31G* [97] basis set for the molecular device and the CH_2 groups. Since our model system does not directly simulate any real-world experimental setup, the minimal basis set should suffice for the description of the leads, which simply serve as a source and a drain of electrons. To assess the effect of the choice of the basis set for the leads, we have performed a few calculations using 6-31G* for the entire system and compared them to the calculations using the mixed basis described above. The results, given in Fig. 5-3, show that the qualitative shapes of the I-V curves are not affected by the choice of the leads' basis set. As we replace 6-31G* by STO-3G on the leads, we observe a decrease in the current at larger voltages. This can be explained by the fact that the STO-3G basis set is more restricted and less diffuse, which effectively results in weaker coupling.

Fig. 5-4 compares the I-V curves obtained with four electronic structure methods. LDA predicts a nonzero current even for very small applied voltages ($v \approx 2.5$ V). The Half&Half hybrid gives nonzero fit current only for $V > 5.4$ V. HF and LC-LDA yield nonzero current only for $V > 10.8$ V. The I-V curve obtained with LC-LDA is very similar to the HF result, both qualitatively and quantitatively. These results are consistent with the band gap predictions for an *isolated* butadiene molecule obtained with the various functionals. LDA predicts a very small gap (4.1 eV), Half&Half predicts a much larger gap (7.9 eV), and HF and LC-LDA predict the largest gaps (12.0 and 11.5 eV, respectively). One expects this, because in both situations the reduction of the gap is linked to the presence of SIE in the approximate exchange correlation functionals [92, 93, 94, 121].

Fig. 5-4 clearly illustrates a well-known[121] problem of LDA: in the weakly-

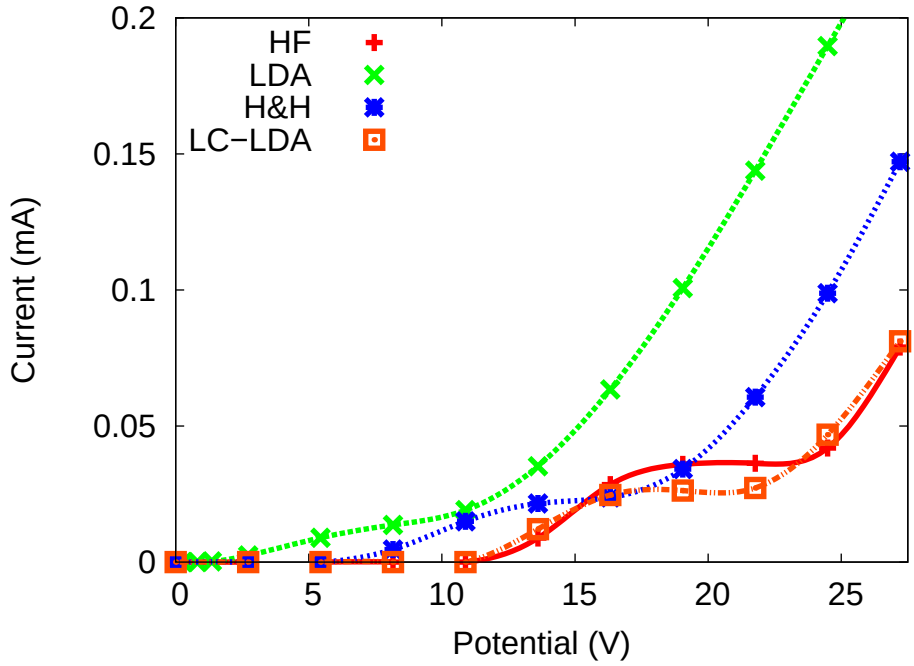

Figure 5-4: The I-V curves computed with four different methods. The STO-3G basis set is used for the leads and 6-31G* for the rest of the model system.

coupled limit, LDA gives too large currents at low voltage biases. This problem is attributed to the SIE and lack of the proper derivative discontinuity. The Half&Half hybrid yields an I-V curve that is shifted halfway in-between the LDA and HF curves (see Fig. 5-4). This is expected since the Half&Half exchange functional is a linear combination of LDA and HF exchange. LC-LDA hybrid combines LDA and HF in a very different way, preserving the correct long-range behavior of the exchange potential. As evidenced by the results in Fig. 5-4, this correct long-range behavior is crucial for proper description of the electronic transport in a molecular device weakly coupled to the leads. Finally, we note that LC-LDA includes local correlation, whereas HF has none. Inclusion of local correlation appears to have very little effect on the conductance at any bias. Taken together, these observations essentially extend the conclusions of Refs. [122, 56] to finite bias: at any value of V it is only the *non-local* portion of the xc functional that influences the charge transport. In commonly used functionals, only the exchange has a non-local component, and so the exchange plays a decisive role in the transport predictions

5.3 Model Hamiltonian Conductance Simulations

5.3.1 The PPP Model Hamiltonian

Because the conductance curves show such a strong variability with the choice of xc functional, it is not possible to conclusively determine the correct form of the I-V curve from the data above. Among the four methods represented in Fig. 5-4, one might consider the LC-LDA and HF results to be the most realistic since HF and LC-LDA are free (or nearly free) of SIE. But neither of these include any effects of non-local correlation, and it is entirely possible that the effects of non-local correlation counteract all or part of the non-local exchange contribution. To put it another way, it is possible that a semi-local functional might actually give a better prediction through cancellation of errors between SIE and the missing part of the correlation energy. To settle this uncertainty, one would like to perform wavefunction-based simulations of the conductance. Unfortunately, with commonly used quantum chemistry techniques (e.g. MP2 or CCSD) this is not computationally feasible for a junction of this size. However, if we first map the dynamics onto a model Hamiltonian we can vastly reduce the number of degrees of freedom, making highly accurate wavefunction predictions possible.

Toward this end, we attempt to reproduce the conductance results of the full TDDFT and TDHF dynamics with those generated by the PPP [136, 137, 138, 139] model (sections 2.7 and 4.1.3). We have shown in chapter 4 [152] that, given the proper parameters, PPP can do an excellent job of reproducing the real time conduction predictions obtained in more sophisticated TDDFT simulations.

In the PPP picture, one models the π electrons by including only the p_z orbitals on each carbon atom in the conjugated chain. Thus, for our junction we will have $N = 48 + 4 + 48 = 100$ orbitals in the model space. The PPP Hamiltonian is given in equation 2.39. We set $r_{j,k} = 2.647\,|j-k|$, $g_{jk} = 0.55$ and fix the adjacent hopping parameter $\beta_{j,j+1}$ to the constant value $\beta_0 = 0.16$ as long as j and $j+1$ both belong to either a lead or the molecule. All non-adjacent hopping parameters are zero. These values were shown in chapter 4 to reproduce the TDDFT predictions of both charge

and spin dynamics of conjugated carbon chains quite well [152]. Meanwhile, if j belongs to the molecule and $j+1$ to a lead (or vice versa), the hopping parameter is reduced by a factor of 0.15 to $\beta_{Gap} = 0.024$. This reflects the reduced overlap between the p_z orbitals separated by a saturated CH_2 unit. Reasonable variations in the magnitude of of β_{Gap} have little effect on the shape of the I-V curve, but have a significant impact on the magnitude of the overall current.

5.3.2 Non-local Exchange in the PPP model

In order to be sure that the PPP model contains the proper physics, one would like to obtain PPP-based models that reproduce the different TDDFT results above (LDA, Half&Half, HF, LC-LDA). We determine the PPP-HF effective one-electron Hamiltonian according to the Hartree-Fock method to give equation 2.41. Currents are obtained strictly analogously to TDDFT by the slope of the quasi-steady state linear fit of $N(t)$ in the closed shell equivalent of equation 4.7.

In order to obtain analogs for the various density functionals within the PPP model, we begin with the working hypothesis that only the non-local part of the xc functional matters. On this basis, one would conclude that LDA - which has no non-local xc part - should be represented by an effective Hamiltonian of the form of Eq. 2.41 with the non-local exchange term removed (PPP-LDA). Continuing along this line of thought, one obtains PPP-Half&Half by multiplying the exchange term by $\frac{1}{2}$ and PPP-LC by multiplying Γ_{jk} in the exchange term by $\mathrm{erf}(0.5 r_{jk})$. The reader will recognize PPP-HF, PPP-LDA, and PPP-Half&Half as the methods PPP, PPP-Hartree, and PPP-SIE from chapter 4 here renamed to clarify their relationships to the all-electron methods. On the one hand, these are drastic approximations because one neglects all the effects of local exchange and correlation. On the other hand, this picture is certainly consistent with the results of the previous section and previous work [122, 56, 121, 174, 187, 152] and so one anticipates it may be effective.

Fig. 5-5 compares the I-V curves calculated using the PPP models described above with those calculated using TDDFT with various functionals. We note that, like the TDDFT methods, the PPP results show a gap between $V = 0$ and the

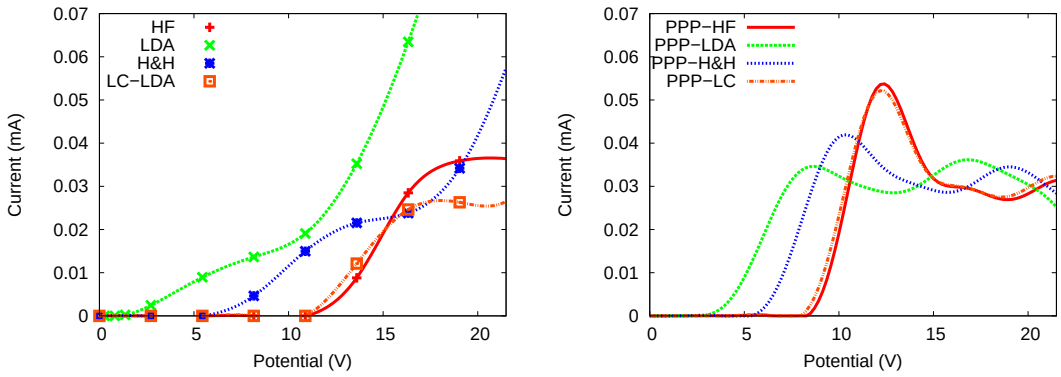

Figure 5-5: Current-voltage plots calculated using several all electron (left) and PPP (right) methods. Analogous all electron and PPP method pairs are given the same color and line type. The conductance gap shows the same trend with respect to nonlocal exchange for the PPP and all-electron calculations.

first appearance of current. Furthermore, the change in the size of gap with the amount of exact exchange mirrors the result calculated with all-electron methods. We find the largest conductance gap with 100% exact exchange methods (HF) and the smallest gap with methods that include no exact exchange (LDA). The 50% exact exchange methods (Half&Half) show an intermediate gap. Finally, like the all electron results, the long range corrected method (LC-LDA) is quantitatively very similar to PPP-HF. We note that in each case, the all electron methods show a monotonic increase in current after turn-on, while the PPP results tend to saturate. This difference is likely due to the absence of any orbitals besides the p_z orbitals in the PPP calculations. While unimportant at low biases, the σ orbitals will play a significant role at higher bias, leading ultimately to a discrepancy between the methods for large values of V. Finally, we note that the quantitative differences between the PPP and TDDFT(TDHF) turn-on voltages could be adjusted somewhat by changing the electron repulsion parameter g.

Overall, the strong qualitative agreement between the PPP model and the TDDFT results points toward two conclusions. First, it provides further evidence that non-local exchange dominates the conductance behavior of these functionals. We have completely neglected local xc-contributions to obtain the PPP-LDA, PPP-Half&Half and PPP-LC results. The fact that these are even remotely correct suggests that the

local contributions are small compared to the dominant HF exchange contribution. Second, these results strongly suggest that the PPP model, while simple, contains enough physics to describe influence of exchange and correlation on transport in these junctions.

5.3.3 Correlated Conductance of the PPP model

Now that we have validated our model Hamiltonian and examined the importance of non-local exchange, we would like to answer the question: what effect does non-local correlation have on the conductance? We will address this point using a time-dependent version of the generator-coordinate method (GCM). The GCM was first introduced by Wheeler and Hill to describe correlation in nuclear matter [188, 189]. More recently, the GCM has been used to make connections between DFT and wavefunction-based approaches to correlation [190, 191]. For a time independent problem, the fundamental idea is to write the target wavefunction, Ψ, as a linear transformation of a continuous set of states:

$$|\Psi\rangle = \int c(\eta)|\Phi(\eta)\rangle d\eta. \tag{5.1}$$

Here $|\Phi(\eta)\rangle$ is some approximate wavefunction and the variable η could be any continuous parameter that deforms Φ. In order to determine the optimal ground state Ψ, one solves the Wheeler-Hill (WH) equation for the coefficients, $c(\eta)$:

$$\int \left[\hat{H}(\eta;\eta') - E\hat{S}(\eta;\eta')\right] c(\eta')d\eta' = 0, \tag{5.2}$$

where $H(\eta;\eta') \equiv \langle\Phi(\eta)|\hat{H}|\Phi(\eta')\rangle$ and $S(\eta;\eta') \equiv \langle\Phi(\eta)|\Phi(\eta')\rangle$ are the matrix representations of the Hamiltonian and overlap, respectively. The GCM can also be used to describe correlated dynamics [191]. Here one writes the time-dependent GCM wavefunction, $\Psi(t)$, as

$$|\Psi(t)\rangle = \int c(t;\eta)|\Phi(\eta)\rangle d\eta, \tag{5.3}$$

where the time evolution of the coefficients, $c(t;\eta)$, is governed by the time-dependent WH (TD-WH) equation:

$$\int \left(\hat{H}_b(\eta;\eta') - i\frac{\partial}{\partial t}\hat{S}(\eta;\eta') \right) c(t;\eta')d\eta' = 0. \tag{5.4}$$

The physical picture in the GCM model is that, while the approximate $\Phi(\eta)$ may not provide an accurate picture of either the ground state Ψ or $\Psi(t)$, one expects that the set of all $\Phi(\eta)$ will provide a *good basis* for expanding the true solutions. For example, while each $\Phi(\eta)$ might be a single determinant, the correlated state Ψ can in principle involve an *infinite* number of determinants.

In practice, Eq. 5.2 is discretized by choosing a fixed set of deformations $\{\eta_i\}$. The WH equation is then equivalent to a nonorthogonal configuration interaction (CI) calculation in the space spanned by the states $|\Phi_i\rangle \equiv |\Phi(\eta_i)\rangle$:

$$\mathbf{H}\cdot\mathbf{c} = E\mathbf{S}\cdot\mathbf{c}. \tag{5.5}$$

The Hamiltonian matrix, $\mathbf{H}$, has elements $H_{ij} \equiv \langle\Phi(\eta_i)|\hat{H}|\Phi(\eta_j)\rangle$ and the overlap matrix , $\mathbf{S}$, is defined by $S_{ij} \equiv \langle\Phi(\eta_i)|\Phi(\eta_j)\rangle$. Meanwhile, the TD-WH equation can be rearranged to:

$$i\frac{\partial}{\partial t}\mathbf{c}(t) = \mathbf{S^{-1}}\cdot\mathbf{H}\cdot\mathbf{c}(t), \tag{5.6}$$

which can be integrated using standard numerical integration techniques. Like any CI method, GCM is exact if enough discrete deformations are included. In practice, the GCM with even a few η_i can describe correlated ground state properties extremely well [190].

In our case, we want to describe the wavefunction as a function of two obvious deformation parameters: potential bias (V) and time (τ). Thus we write the time dependent GCM wavefunction in terms of the group parameter $\eta = \{V, \tau\}$:

$$|\Psi(t)\rangle = \int c(t;\eta)|\Phi(\eta)\rangle d\eta = \int c(t;V,\tau)|\Phi(V,\tau)\rangle dV d\tau. \tag{5.7}$$

Here, $|\Phi(V,\tau)\rangle$ is an approximate (e.g. HF or DFT) wavefunction propagated for a time τ in a potential bias V. We can then determine the ground state in the absence of the potential by the analogous WH equation:

$$\int \left(H(V,\tau;V',\tau') - ES(V,\tau;V',\tau')\right) c(0;V',\tau')dV'd\tau' = 0. \tag{5.8}$$

Here $H(V,\tau;V',\tau') \equiv \langle\Phi(V,\tau)|\hat{H}|\Phi(V',\tau')\rangle$ and $S(V,\tau;V',\tau') \equiv \langle\Phi(V,\tau)|\Phi(V',\tau')\rangle$. Given that the system starts in the ground state (Eq. 5.8) we can also follow the time evolution in the presence of a bias potential, V_b, by solving the TD-WH equation:

$$\int \left(H_b(V,\tau;V',\tau') - i\frac{\partial}{\partial t}S(V,\tau;V',\tau')\right) c(t;V',\tau')dV'd\tau' = 0, \tag{5.9}$$

where $H_b(V,\tau;V',\tau') \equiv \langle\Phi(V,\tau)|\hat{H}+\hat{V}_b|\Phi(V',\tau')\rangle$ is the matrix representation of the Hamiltonian in the presence of the bias. To be clear, in the above equation t and V_b correspond to the physical time and physical bias potential in the simulation, while V,τ,V' and τ' correspond to the deformation parameters used as generator coordinates. It is important to recognize that this realization of TD-GCM does not assume that TDDFT or TDHF provides a good picture for the dynamics. Rather, one assumes that the TDDFT/TDHF wavefunctions with different biases and evolved for different times provide a good *basis* for expanding the true time-dependent wavefunction. In this respect, the present formulation of time dependent GCM is somewhat more flexible than previous versions [191]. Like the canonical version, the TD-GCM is exact if enough determinants are included in the expansion.

TD-GCM provides a powerful and flexible means of examining explicit non-local correlation effects on electron dynamics. Here, we perform microcanonical transport simulations using the above TD-GCM formalism as follows. 1) The integral form for the wavefunction (Eq. 5.7) is discretized in both time, τ_i, and potential, V_j. Because there are 100 orbitals and 50 electrons in our PPP model of the junction, a complete CI calculation would require approximately $\binom{100}{50}^2 \approx 10^{28}$ determinants. Clearly it is impossible to include even a small fraction of these states in our TD-GCM space. At

this point, the choice of basis states in TD-GCM becomes significant: the TDDFT evolution used to generate the basis states naturally selects only configurations that are important to the dynamics. In practice, we find that ≈ 30 time points and ≈ 300 biases (for a total of only $30 \times 300 \approx 10^4$ determinants) gives essentially converged results. We also find that faster convergence is achieved if different potentials are applied to the $\uparrow$ and $\downarrow$ electrons ($V_j^{\uparrow} \neq V_j^{\downarrow}$) in a spin-unrestricted fashion. We suspect this relates to the difficulty of representing open shell singlet configurations in terms of closed shell basis states. 2) We solve for the lowest eigenvector of $\mathbf{H}$ (Eq. 5.5) and use this as the initial state for all subsequent propagation. To solve the eigenvalue problem, we first transform to an orthogonal basis by pre- and post-multiplying by $\mathbf{S}^{-1/2}$. 3) The time evolved coefficients, $\mathbf{c}(t)$, under the bias, V_b, are obtained from Eq. 5.6 by constructing the time evolution operator $\mathbf{U}(t) \equiv exp\left[-i(\mathbf{H} + \mathbf{V_b})t\right]$ in the orthogonalized basis. 4) Using the thus computed $\mathbf{c}(t)$ one computes the time evolution of $N(t)$. A linear fit of $N(t)$ versus t in the quasi-steady state region gives the predicted current I for the present bias. 5) Steps 3&4 are repeated for several voltages to generate an I-V curve.

Using the above prescription for the PPP model of the junction in Figure 5-1, we obtain the GCM results shown in Figure 5-6. For comparison, the PPP results from Fig. 5-5 are also reproduced in Figure 5-6. The GCM results in this figure were obtained from a basis of 560 potentials with $-27\ V < \frac{V^{\uparrow}+V^{\downarrow}}{2} < 27\ V$, $-2.7\ V < \frac{V^{\uparrow}-V^{\downarrow}}{2} < 2.7\ V$ and 32 times, τ, with $-24\ fs < \tau < 24\ fs$. There are a total of 17,920 determinants, but the results are not appreciably different if the GCM space is reduced by 50%. Further, the basis selecting propagation in this example was performed with PPP-HF, although similar results could be obtained with other functionals. The striking feature of the TD-GCM results is that the transport gap is actually somewhat *larger* than that predicted by TDHF. This trend is opposite the effect predicted by any of the semilocal xc functionals. Those functionals tend to significantly *narrow* the gap if less than 100% long range exact exchange is included, and have negligible impact otherwise. Thus, none of the commonly used functionals provides an appropriate treatment of electron correlation in these junctions. This

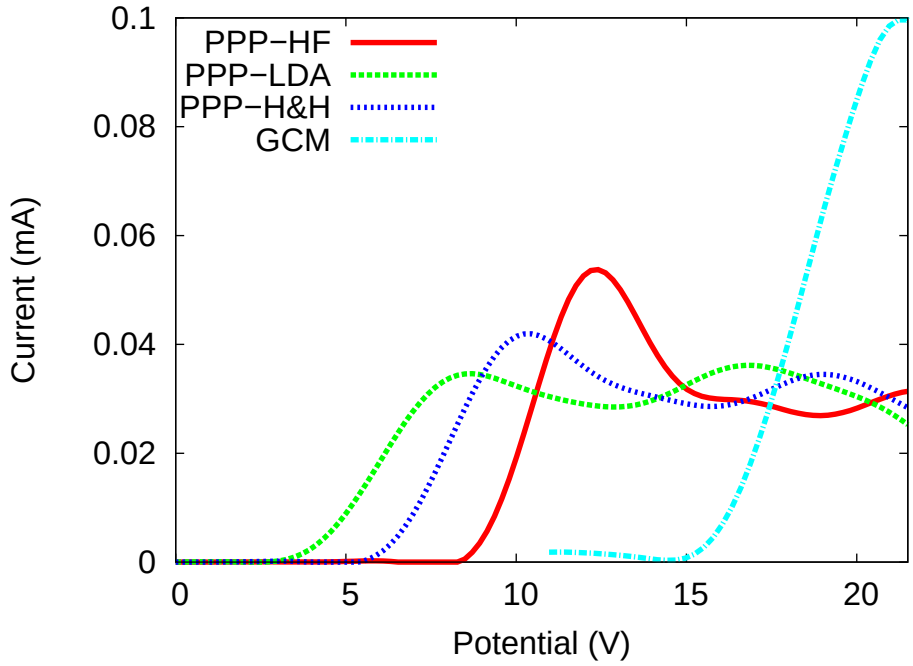

Figure 5-6: Current-voltage plots calculated using several PPP methods. The non-local correlation present in the GCM calculations results in qualitative changes in the current including a near doubling of the conductance gap.

trend in the transport gap is at odds with the typical expectation for band gaps: usually, while semilocal functionals severely underestimate gaps [93, 94], 100% non-local exchange overestimates them [192]. We attribute the unusual behavior in this case to the fairly large U value of $g = .55\ a.u.$ (15.0 eV) in these polyethylene wires, which places the system very near a Mott insulator transition [193]. In a Mott insulator, every site becomes strictly singly occupied in the ground state and only the spin on each site varies: $\mid \uparrow\downarrow\uparrow \ldots\rangle$. In order to induce transport in the Mott regime, one site must become doubly occupied, which incurs a penalty of g relative to the all-singly occupied configuration. Thus, if our system were a true Mott insulator the gap would be $\frac{g}{e} = 15.0\ V$, which is actually quite close to the transport gap predicted in the GCM calculations. Thus we conclude that, in the GCM calculations, the transport gap is larger because the correlated ground state is more Mott-like than the HF one.

The second obvious feature of the GCM results is that after the gap is overcome,

the currents are somewhat larger in the correlated calculations. We note that there is a fair bit of uncertainty in the correlated currents because the N vs. t plots for GCM are much less linear than they are for HF. An example of this is illustrated in Fig. 5-7. Clearly, the GCM results show long-time oscillation superimposed on a generally linear trend. The persistent oscillation in $N(t)$ might be evidence of a long-lived quasi-bound state on the molecule [151], but we have not been able to verify this possibility. In any case, the variation of $N(t)$ makes precise estimation of the true steady-state current difficult. We have chosen to use the short-time data (e.g. the first 2.5 fs in Fig. 5-7) to tabulate the currents in Fig. 5-6, since this avoids any potential complications from finite-size effects at long times. If we had instead chosen to average over a long time interval (e.g. over the first 6 fs in Fig 5-7) the overall currents would be smaller - similar in magnitude to the HF results, in fact. However, if we fit over the longer interval, the computed GCM transport gap also becomes even larger (17 V) because the oscillations tend to wash out any directed charge flow when the current is small. Thus, while the GCM result in Fig. 5-6 should be viewed as somewhat imprecise, one conclusion is unavoidable: nonlocal correlation shifts the I-V curve opposite the direction predicted by semilocal DFT.

5.4 Conclusions

In this chapter we have examined the impact of common approximations to exchange and correlation on the simulation of electron transport through molecular junctions. We use the prototypical device shown in Figure 5-1 as a model system, and employ the microcanonical picture of *real time* electron transport to study the conductance with various approximations to the electronic structure. The microcanonical picture has the advantage that it is in principle exact for any formalism, such as TDDFT, that produces the exact density. Real-time TDDFT simulations with different approximate *xc* functionals reveal that only the non-local Hartree-Fock exchange has any significant impact on transport - the choice of local functional has only a marginal effect. These observations are consistent with previous results concerning the zero-bias

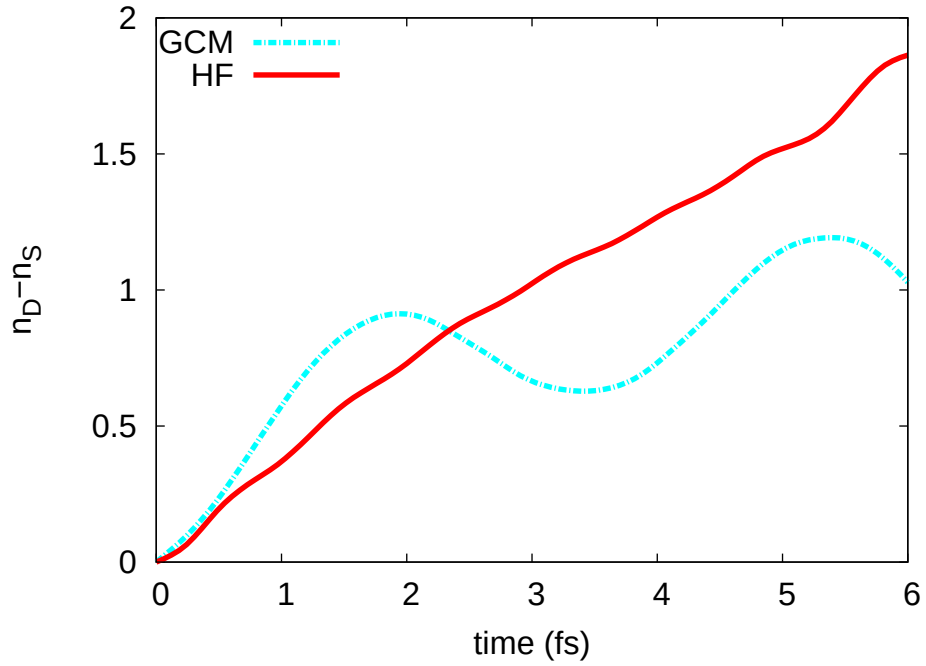

Figure 5-7: Time-dependent lead charge difference in TD-GCM and TDHF calculations at a fixed bias of 20 V. The correlated results show persistent oscillations not present in the uncorrelated results.

conductance of a junction [122, 56]. In order to examine the influence of non-local *correlation* on transport, we first map the molecular junction onto a PPP model Hamiltonian. We demonstrate that appropriately parametrized PPP dynamics provide a reasonably faithful description of the TDDFT charge currents obtained with different *xc* functionals. Meanwhile, because of the simplicity of the PPP model, the complicated effects of non-local correlation can be easily incorporated using the generator coordinate method. We find that non-local correlation actually tends to widen the transport gap in our model junction, whereas all commonly used approximate *xc* functionals narrow the gap. Thus, conductance could be something of a worst-case scenario for semilocal *xc* functionals, which are most successful when there is a partial cancellation between nonlocal exchange and nonlocal correlation. In the particular model studied here, these two nonlocal energy components shift the gap in the *same* direction, so that partial neglect of one of these terms is bound to lead to large errors.

Our work has a number of implications in the ongoing search for accurate meth-

ods for predicting molecular electron transport properties. First, our results strongly suggest that most existing approximate functionals significantly overestimate the current in molecular devices because they do not contain 100% exact exchange. Typical metal-molecule-metal junction experiments are performed in the tunneling regime, which corresponds to the low bias region in this paper. In this situation, nearly all the functionals predict low currents, but the ones with larger transport gaps will produce *exponentially smaller* currents. We find that by far the dominant factor in determining the transport gap is the non-local HF exchange term. Second, our results show that non-local correlation has a much smaller effect on the current in the *ballistic* regime, where the bias is large enough to push an electron on or off the molecule.

Moving forward, our findings suggest several avenues for future research. First, it should be noted that all our conclusions have been drawn from a single test system. It will be very interesting to see how these results change, or if they change at all, for a more realistic molecular junction such as the Gold-BDT-Gold junction that is used as a common test case of molecular transport. We will explore this system in chapter 6. Second, our findings argue for increased investigation of non-local density functionals in conductance simulations. We have here demonstrated that a fully non-local exchange model - as in LC-LDA - can provide a significant improvement in DFT transport predictions. It would be extremely interesting to explore the analogous influence of truly non-local *correlation* methods. For example, one would expect that a method like GW-BSE [194] or EOM-CC [195] should significantly improve DFT transport predictions. A more computationally practical approach might be given by TD current DFT [196, 197], where at least some degree of density non-locality can be encoded by the local current [198, 199, 124]. It is our expectation that investigations along these lines will lead to advances both in the accurate prediction of electron transport and the accurate description of electronic structure using wavefunction- and density-based techniques.

5.5 Acknowledgements

The work in this chapter was performed in collaboration with Oleg Vydrov.

Chapter 6

Dynamic Coulomb Blockade in a Metal-Molecule-Metal Junction

When examining conductance through systems, such as organic molecules, in which electronic motion is hindered relative to metals, we must consider coulomb blockade. Coulomb blockade, a term borrowed from the study of quantum dots [49] refers to the small conductance caused by the energetic cost of adding or removing an electron from the molecular device in the process of conduction [18, 6]. As a result of this energy cost, theoretical results have suggested that within the coulomb blockade regime, conductance is especially sensitive to the charge on the molecular device [200, 185, 201, 202].

Closely related to molecular charge and coulomb blockade is the application of a gate potential. While the current is driven by a voltage applied within the metallic leads, a gate voltage is applied to the conducting device to alter it's conductance properties. By shifting the energies of the molecule states, the gate voltage can either mimic or induce charging of the device making gating a natural method to study charging effects. Single-molecule gate voltage experiments have been performed [203, 204, 6], however the difficulty in constructing three terminal devices using a molecule as small as benzene-1,4-dithiol (BDT), the device under examination in this chapter, makes obtaining reliable results difficult. Theoretical studies [205, 206] of gating effects are not hindered by such issues, so we here apply a gate voltage to

examine charging effects.

Recall from section 1.4 that NEGF, the most common method to calculate quantum scale conductance, assumes a steady state conduction picture. However, derivations performed by Stefanucci [151] suggest that the conducting electronic state undergoes current and density oscillations in the presence of bound states. Likewise in chapter 3, we demonstrated rapid fluctuations of the transient current in a polyacetylene model system. In this case, a steady-state assumption is inappropriate.

In this chapter, we apply our real-time DFT propagation method to the gold-BDT-gold system. We calculate the current-voltage behavior for small potentials using each of three exchange-correlation methods, LDA, B3LYP, and Hartree-Fock, to examine conductance in the coulomb blockade regime. In addition to the current-voltage behavior, we also examine dynamic transport and molecular charge behavior in the LDA method to examine the applicability of the steady-state assumption. Finally, we calculate currents under a gate voltage to examine in more detail the charge effects on transport.

6.1 System and Method

The system geometry under study is a BDT molecule covalently bound to the 111 face between two Au_{114} clusters in the FCC position. We construct the geometry by reflection symmetry on portions of a previously optimized geometry[207] for phenylthiol chemisorbed to a gold surface. We replicate the gold layers in the 111 reciprocal direction to produce an elongated wire structure. The system geometry is included as appendix A. We choose a structure elongated in the direction of electron transport (Z) to allow sufficient density of momentum states in the Z-direction and sufficient time before reflection at the wire ends manifests in the current. The electrons are described by the Hay-Wadt pseudopotential and minimal basis [98] on the gold atoms and the Aldrichs VDZ basis [99] augmented with heavy atom d functions on all other atoms. Quantum chemistry calculations are performed using a development version of Q-Chem [176]. The system is divided into source, molecular device, and electron

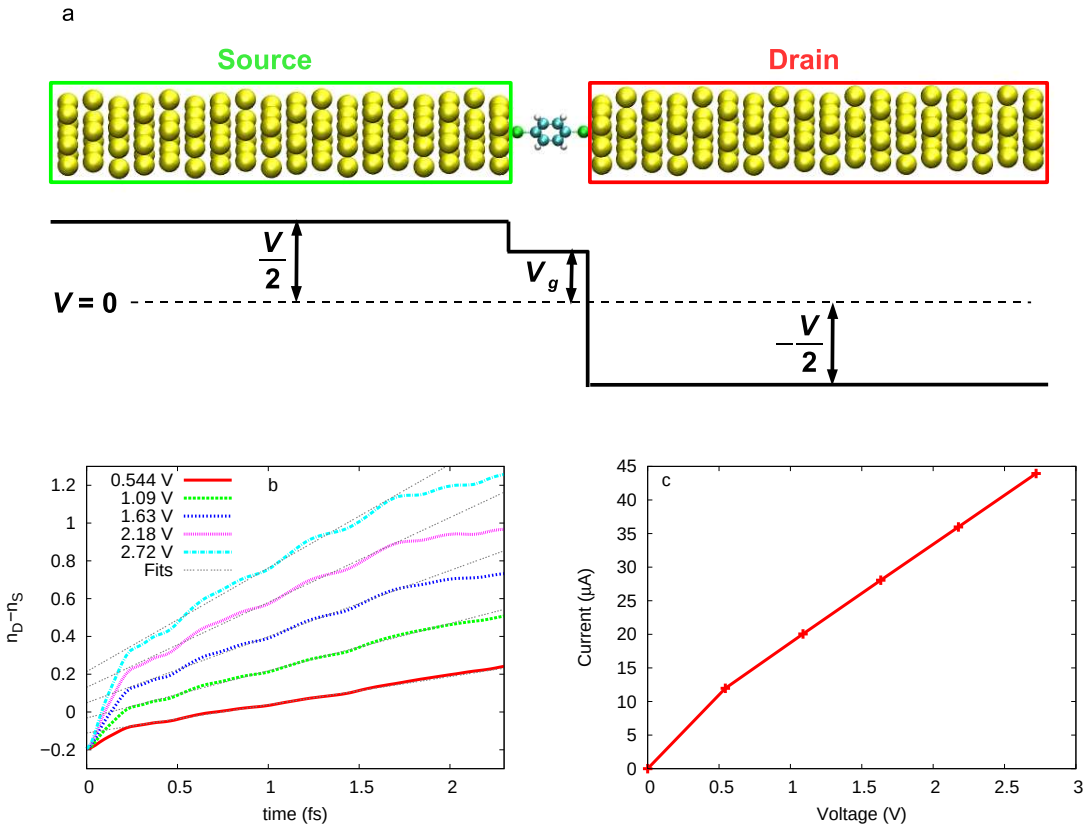

Figure 6-1: (a) Au_{114}-BDT-Au_{114} system with source and lead regions labeled along with the effect of lead potential, V, and gate potential, V_g, on electronic energies in each region. Atoms depicted include H (gray), C (light blue), S (green), and Au (gold) (b) Time dependent density difference ($n_D - n_S$) with linear fitting in the steady state region and (c) resulting current-voltage curve.

drain regions for the purpose of voltage profile and density definitions as shown in Fig. 6-1a.

We calculate currents via the voltage bias method defined in section 1.5 and used in chapter 5. For some of the calculations in this chapter, we include a gate voltage with the additional term $V_g\hat{n}_M$. The effect of the lead and gate voltages on the electronic state energies in each region is shown in Fig 6-1a. We determine the current from the time-dependent densities by the least-squares linear regression fitting method.In this chapter, the current is calculated over the time period of 0.24 to 1.57 fs. As an example, the regression fitting and I-V plot for the LDA functional are shown in Fig. 6-1b and c. This figure shows that we maintain a fairly good early time steady state with systems more complicated than the essentially one-dimensional polyacetylene systems we studied in chapters 3, 4, and 5.

6.2 Results and Discussion

Using these methods, we have generated small bias I-V curves with the LDA, B3LYP, and Hartree-Fock functionals. These results are shown in Fig. 6-2. We note that the calculated I-V curves are mostly linear over the low-bias regime shown. For Hartree-Fock, the average conductance over the calculated range is 0, indicating that this voltage range lies within the HF predicted conductance gap for the system. On the other hand, both B3LYP and LDA predict no conductance gap at the plot resolution of Fig. 6-2. A decrease in the conductance gap with methods that do not include 100% exact exchange has been previously reported [123, 208]. The average conductances, calculated from the largest plotted voltage point are 16 μS with LDA, and 10 μS with B3LYP. For comparison, the conductance quantum is 77 μS and the experimental conductance of BDT at the first conductance step (at $1.3V$) is approximately 0.05 μS [1]. Recall that this orders of magnitude overestimation of current over experiment is a common property of conduction calculations [56], especially with reduced exact exchange.

Although the difference in conductance between these methods has been asso-

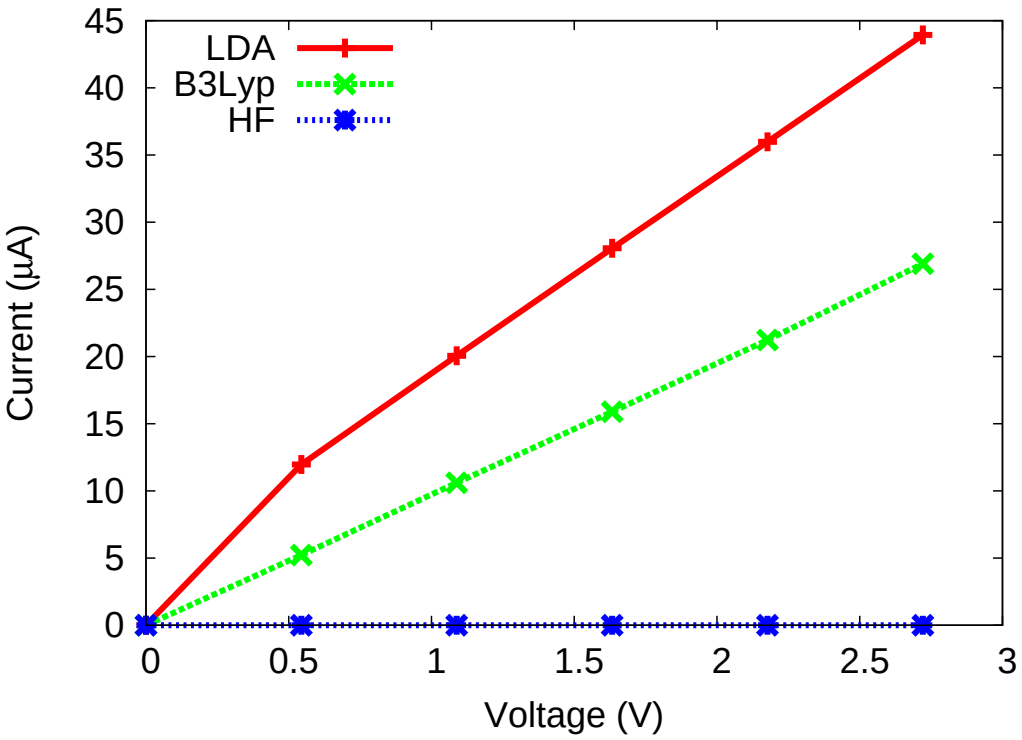

Figure 6-2: TDDFT calculated current-voltage curve using B3LYP, LDA, and Hartree-Fock exchange-correlation functionals. The calculated conductances are 16 μS with LDA, 10 μS with B3LYP, and 0 with HF

ciated with a decrease in the device HOMO-LUMO gap with the introduction of self-interaction error [123, 122, 124], we also notice a correlation with the density distribution in the equilibrium state. Using the Löwdin population definition, the total charge on the molecule is -1.38 with Hartree-Fock, -0.955 with B3LYP, and -0.851 with LDA. Thus, a more negative electronic charge on the molecular device correlates with a decrease in its conductance. This behavior resembles the coulomb blockade described earlier in that the additional Coulombic energy cost from increased electronic density correlates with decreased conductance.

We can estimate the coulomb energy associated with the charge differences if we simplify the molecular device to be a sphere of uniform charge density. In that case, the Coulombic repulsion energy is $E_C = \frac{3q^2}{20\pi\epsilon_0 R}$ where q is the total charge, and R is the radius. We choose the radius to be half the distance between the sulfur atoms in the BDT device, so $R = 3.2$ Å. The resulting energy difference between the LDA and HF calculated charges is 3.2 eV. This energy is certainly sufficient to push the conduction states outside of the voltage window. Furthermore, it is likely that charging the device to -1 or below saturates the conduction bands. Thus it is reasonable that the difference in equilibrium molecular charge predicted by the various functionals accounts for the differences in conduction behavior.

We generate the I-V curves from relatively short time dynamics ($t < 1.75$ fs) in which the current is approximately steady, but we find significantly different behavior at longer times. In Fig. 6-3, we plot dynamics results for the LDA calculated propagation under several external potentials. The dynamics data indicate that the electron density transport from the source to the drain does not occur at a constant rate. All three of the propagations include regions in which the time derivative of $n_D - n_S$, and therefore the transient current, is 0 or even negative. We see similar current oscillations with B3LYP, but because these long-time dynamics are computationally intensive, we choose to focus on the LDA results with the expectation that the B3LYP results would be qualitatively similar. Qualitative similarities in the I-V curve outside of the conductance gap with the various functionals [208, 123] suggests we may see similar results with HF as well.

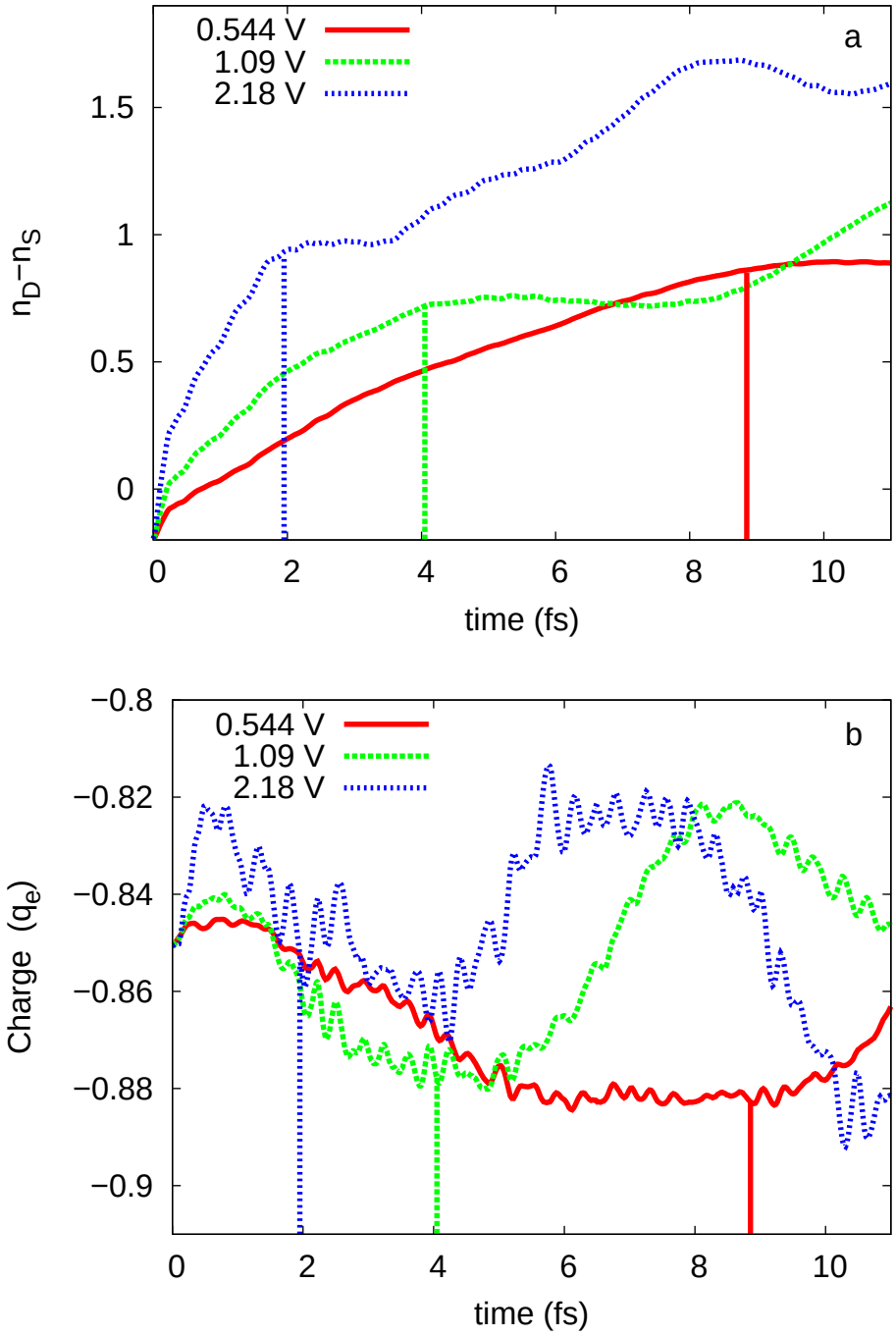

Figure 6-3: Time dependent density difference ($n_D - n_S$) (a) and device charge (b) as calculated by LDA. The vertical lines indicate approximated times at which the first 0 current regions begin for each potential. The periods of 0 current correspond with more negative charge on BDT.

In addition to the current oscillations, the long time simulations also demonstrate oscillations in the density on the molecule. These current and density oscillations demonstrate that the system does not evolve towards a steady state, but instead shows oscillatory behavior in support of the predictions of Stefanucci [151]. We have demonstrated the rapid oscillations previously [140] for simple conjugated wires, but this is the first work in which we examine oscillations with time periods as large as several fs. Stefannuci ascribes these oscillations to bound states in the system. Although this suggests that the oscillations represent resonance with molecular states, energies associated with the large period oscillations are smaller than the HOMO-LUMO gap of the bare molecular device. Additionally, their periods are sensitive to the applied potential, so the states corresponding to these oscillations must have a significant component on the metallic leads.

The lead dependent nature of the oscillations initially suggests the they are a finite system effect and that the periods of zero current may be caused by saturation of the finite leads or reflection off the ends of the wire. We discount the first possibility, because the positive current reappears and transports more electrons to the drain. We examined the second possibility by performing test calculations using shorter gold wires and found that the oscillation frequencies do not show a systematic change with wire length. Thus, the oscillations are not simply a finite lead effect.

The dynamics in Fig. 6-3 indicate a correlation of a period of zero current, with increased negative molecular device charge. The first period of zero current begins at 8.8 fs for the 0.544 V propagation, 4.0 fs for 1.09V , and 1.9 fs for 2.18V. At all of these points, the molecular charge profile indicates a region of increased negative charge. Although the 0.03 electron variation in charge is small, the uniform spherical charge approximation discussed above leads to a Coulombic energy variation of approximately 0.15 eV, which is significant relative to the voltages considered. Thus, we see a *dynamic* as well as static association between device charge and current, indicating a dynamic equivalent of coulomb blockade.

We note that the correlation observed between molecular charge and current is opposite to the previously reported [185, 201] tendency of a more negative charge to

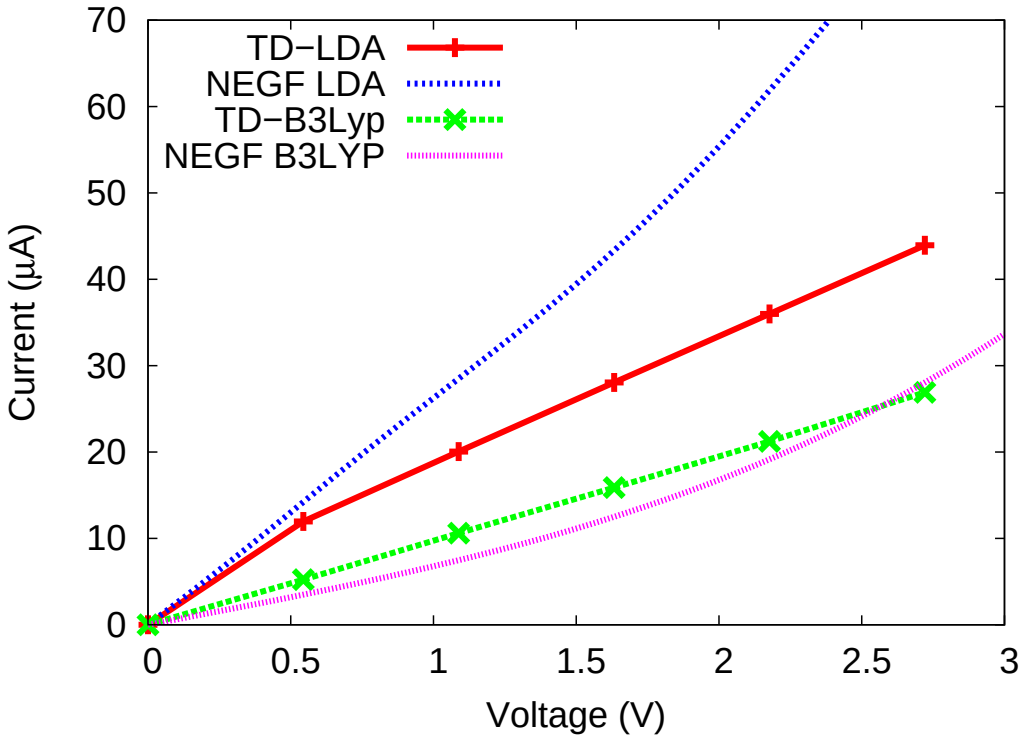

Figure 6-4: I-V plots calculated using both the real time propagation method and the voltage potential version of the NEGF procedure described in section 3.3.3. Both methods produce similar profiles, and there is no systematic difference between the two methods.

increase current. This calculation, unlike the other reported results, does not involve changes in lead-device separation which may impact current. This result may indicate a lowest unfilled molecular orbital influence on transport which would cause current to decrease with a more negatively charged device.

The oscillatory current behavior shown in Fig. 6-3 is relevant to the NEGF formalism, because the NEGF formalism is based upon a steady state assumption. However, the long time calculations indicate that the system reaches a persistent oscillatory, not steady, state. In our method, we generally calculate the current from the early steady state period in which the density is most like the equilibrium distribution used in the majority of NEGF studies. Indeed, we showed in chapter 3 [140] for the *trans*-polyacetylene wire that the NEGF method gives simlar results to the current found in the *short time* by averaging over the rapid oscillations. The NEGF I-V

curves shown in Fig. 6.2 show that this remains the case for Au_{114}-BDT-Au_{114}. The NEGF curves are calculated using the voltage potential (equation 1.36) version of the (non-self-consistent) NEGF procedure described in section 3.3.3. For the system under study, this early time current is certainly larger than the long-time average current including oscillations. If the large early time current is a general behavior, including oscillations would reduce calculated currents.

We do consider the possibility that the present oscillations result from the sudden change in the Hamiltonian at time $t = 0$. We note that by turning the voltage potential on slowly ($V(t) = V_{bias}\,[\mathrm{erf}(\omega t - 2) + 1]$ with $\omega = 2.07$ fs^{-1}) we are able to eliminate the rapid oscillations. We cannot perform a sufficiently long propagation to explore switching slowly enough to impact the slow (hundreds of femptoseconds) oscillations. However, removing the rapid oscillations does not significantly change the short-time I-V results. Indeed it is not clear how quickly we should switch on the potential to properly model experiment.

The association between charge and current suggests that we may be able to alter the current by inducing a change in the device charge . To that end, we introduce a gate voltage to the system under an external bias. Based upon the definition of gate voltage in Fig. 6-1a, we expect a positive potential to produce a less negative charge on the molecular device.

We show in Fig. 6-5, the early time current with an external potential of 1.09 V as a function of gate voltage. As we did for external potentials, we focus on small gate voltages to avoid overwhelming the chosen basis. Examination of the charge dynamics (not shown) verifies that the linear fit time period for current calculation occurs after the molecular charge has equilibrated in response to the gate voltage. The results indicate that by increasing the gate voltage, and thereby making the device charge less negative, we increase the current. We calculate a low voltage response of current to gate voltage of 5.8 μA/V, or 36% of the response to external voltage.

This simulation suggests that we can control the current through BDT with the application of a gate voltage. As a positive gate voltage creates a less negative device charge, the current increases. The device charge changes at a rate of 7.5 q_e/V leading

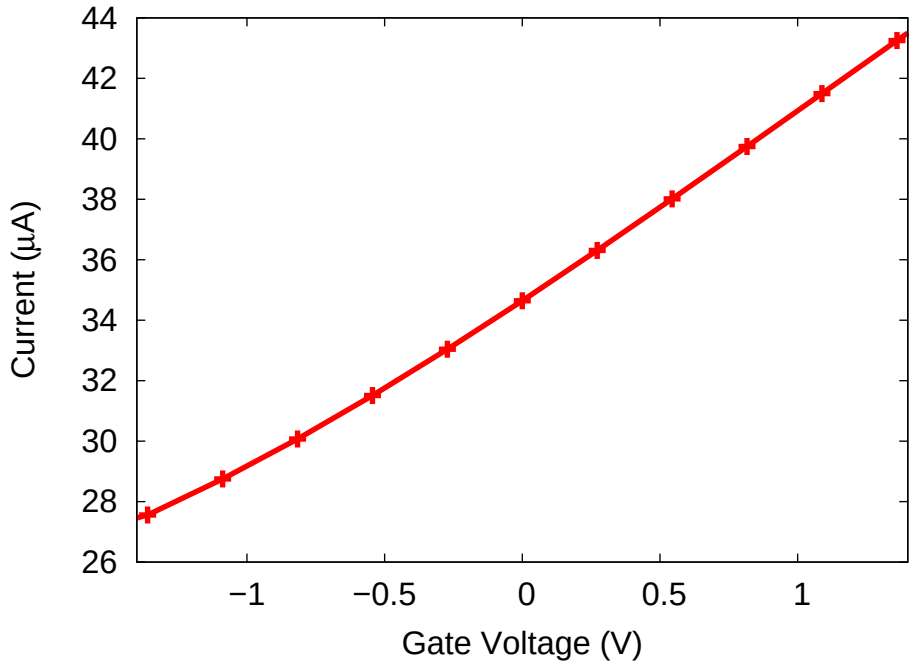

Figure 6-5: TDDFT calculated current as a function of gate voltage with left-right voltage set to 1.09 V and calculated with LDA. The response of current to gate voltage is 5.8 μA/V.

to a current to charge response of 0.77 $\mu A/q_e$. This is clearly much less than the response demonstrated in the dynamic results, however the impact of charge on current is significantly counteracted by the gate voltage required to generate that charge.

6.3 Conclusions

Our real-time propagation of the Au_{114}-BDT-Au_{114} cluster indicate oscillations, not steady state, in both the charge on the BDT molecule and the current from one gold wire to the other as predicted by Stefanucci [151]. A reduction in current is associated with a more negative charge on BDT in agreement with the charge and current comparisons from current calculations under several exchange-correlation functionals. This behavior suggests a dynamic equivalent to the coulomb blockade. We further demonstrate that a gate voltage can be used to induce molecular charging, and thus impact the current. We see that consideration of device charge is essential to predict

low bias conductance through single molecules like BDT. Furthermore, the presence of charge and current oscillations suggest that the steady state approximation may be inappropriate for single-molecule current calculations.

Chapter 7

Conclusions

We have applied real time propagation in time-dependent density functional theory to examine electron transport through quantum scale devices. Our real time method relies upon the time-dependent Kohn-Sham equations in which the single particle Hamiltonian is allowed to vary in time with a changing electron density. This is in contrast with the more common NEGF formalism in which the electronic-state, and therefore the single particle Hamiltonian, are assumed to be time-independent.

We discover in agreement with NEGF studies that transport behavior is highly dependent upon the exchange-correlation approximation. Specifically, we find that a reduction in the fraction of nonlocal, or exact, exchange causes more metallic-like transport. This is more apparent in spin conduction than charge conduction where we lack the coulomb interaction that seems to mitigate the results of exchange approximation. Unlike many properties calculated via density functional theory, conduction does not appear to benefit from a fortuitous cancelation of errors. Indeed, the correlated results in chapter 5 seem to indicate that the correlation errors add to rather than counteract exchange errors.

Where time-dependent conduction calculations improve upon standard NEGF is in rigorous application within density functional theory. TDDFT and the time-dependent KS equations act as a solid formalism in which to apply our propagation method. Furthermore, defining the potential by an externally applied single-particle operator is unambiguous. On the other hand, NEGF with DFT includes two *un-*

controlled approximations. First, the definition of potential in DFT relies upon the orbital energies of the noninteracting reference system, which are not physically relevant. Second, NEGF makes a time-independent Hamiltonian assumption which may not be appropriate in light of the current and density oscillations we have seen. The rapid oscillations in the polyacetylene calculations could be smoothed to give a current similar to that predicted by NEGF. However, the longer time oscillations shown by BDT will likely produce a smaller longtime current than the short time dynamics which correspond to the NEGF formalism. The ability of the time-dependent framework to examine time varying transport behavior is essential to examine this question.

Appendix A

Geometry of the Gold-BDT-Gold System

Table A.1: Geometry of the Au_{114}-BDT-Au_{114} system studies in chapter 6. Coordinates are Cartesian and in Å.

Atom Type	X	Y	Z
Au	9.43053269	4.45477272	45.991
Au	12.0025027	5.93969272	45.991
Au	9.44247983	7.42561905	45.991
Au	9.43053846	1.48492	45.991
Au	6.85856846	2.96985	45.991
Au	12.0037941	2.97263118	45.991
Au	6.85857423	5.93969272	45.991
Au	11.1451769	1.48492	43.569
Au	11.1451827	7.42462272	43.569
Au	8.57321269	5.93969272	43.569
Au	11.1451827	4.45477272	43.569
Au	8.57321846	2.96985	43.569
Au	6.00125423	4.45477272	43.569
Au	7.71582314	1.48492	41.147
Au	7.71581737	7.42462272	41.147
Au	10.2877874	5.93969272	41.147
Au	7.71581737	4.45477272	41.147
Au	10.2877816	2.96985	41.147
Au	12.8597458	4.45477272	41.147
Au	9.43053269	4.45477272	38.725

Continued on next page

Table A.1 – continued from previous page

Atom Type	X	Y	Z
Au	12.0025027	5.93969272	38.725
Au	9.44247983	7.42561905	38.725
Au	9.43053846	1.48492	38.725
Au	6.85856846	2.96985	38.725
Au	12.0037941	2.97263118	38.725
Au	6.85857423	5.93969272	38.725
Au	11.1451769	1.48492	36.303
Au	11.1451827	7.42462272	36.303
Au	8.57321269	5.93969272	36.303
Au	11.1451827	4.45477272	36.303
Au	8.57321846	2.96985	36.303
Au	6.00125423	4.45477272	36.303
Au	7.71582314	1.48492	33.881
Au	7.71581737	7.42462272	33.881
Au	10.2877874	5.93969272	33.881
Au	7.71581737	4.45477272	33.881
Au	10.2877816	2.96985	33.881
Au	12.8597458	4.45477272	33.881
Au	9.43053269	4.45477272	31.459
Au	12.0025027	5.93969272	31.459
Au	9.44247983	7.42561905	31.459
Au	9.43053846	1.48492	31.459
Au	6.85856846	2.96985	31.459
Au	12.0037941	2.97263118	31.459
Au	6.85857423	5.93969272	31.459
Au	11.1451769	1.48492	29.037
Au	11.1451827	7.42462272	29.037
Au	8.57321269	5.93969272	29.037
Au	11.1451827	4.45477272	29.037
Au	8.57321846	2.96985	29.037
Au	6.00125423	4.45477272	29.037
Au	7.71582314	1.48492	26.615
Au	7.71581737	7.42462272	26.615
Au	10.2877874	5.93969272	26.615
Au	7.71581737	4.45477272	26.615
Au	10.2877816	2.96985	26.615
Au	12.8597458	4.45477272	26.615
Au	9.43053269	4.45477272	24.193
Au	12.0025027	5.93969272	24.193
Au	9.44247983	7.42561905	24.193
Au	9.43053846	1.48492	24.193
Au	6.85856846	2.96985	24.193

Continued on next page

Table A.1 – continued from previous page

Atom Type	X	Y	Z
Au	12.0037941	2.97263118	24.193
Au	6.85857423	5.93969272	24.193
Au	11.1451769	1.48492	21.771
Au	11.1451827	7.42462272	21.771
Au	8.57321269	5.93969272	21.771
Au	11.1451827	4.45477272	21.771
Au	8.57321846	2.96985	21.771
Au	6.00125423	4.45477272	21.771
Au	7.71582314	1.48492	19.349
Au	7.71581737	7.42462272	19.349
Au	10.2877874	5.93969272	19.349
Au	7.71581737	4.45477272	19.349
Au	10.2877816	2.96985	19.349
Au	12.8597458	4.45477272	19.349
Au	9.43053269	4.45477272	16.927
Au	12.00250269	5.93969272	16.927
Au	9.44247983	7.42561905	16.927
Au	9.43053846	1.48492000	16.927
Au	6.85856846	2.96985000	16.927
Au	12.00379407	2.97263118	16.927
Au	6.85857423	5.93969272	16.927
Au	11.14517692	1.48492000	14.505
Au	11.14518269	7.42462272	14.505
Au	8.57321269	5.93969272	14.505
Au	11.14518269	4.45477272	14.505
Au	8.57321846	2.96985000	14.505
Au	6.00125423	4.45477272	14.505
Au	7.72387181	1.48479035	12.08177282
Au	7.72559365	7.42686223	12.07125607
Au	12.85690016	4.46409916	12.08287122
Au	7.71589269	4.45477272	12.08818000
Au	10.28785269	5.93969272	12.08818000
Au	10.28785846	2.96985000	12.08818000
Au	9.43053269	4.45477272	9.66331002
Au	12.00250269	5.93969272	9.66331002
Au	9.44247983	7.42561905	9.64513185
Au	9.43053846	1.48492000	9.66331002
Au	6.85856846	2.96985000	9.66331002
Au	12.00379407	2.97263118	9.66785691
Au	6.85857423	5.93969272	9.66331002
Au	11.14517692	1.48492000	7.23844002
Au	11.14518269	7.42462272	7.23844002

Continued on next page

Table A.1 – continued from previous page

Atom Type	X	Y	Z
Au	8.57321269	5.93969272	7.23844002
Au	11.14518269	4.45477272	7.23844002
Au	8.57321846	2.96985000	7.23844002
Au	6.00125423	4.45477272	7.23844002
Au	7.80784846	1.63192000	4.86144002
Au	7.80753423	7.27479272	4.86743002
Au	12.69427115	4.45306272	4.86009002
Au	10.37949846	2.82002000	4.86743002
Au	10.37981269	6.08669272	4.86144002
Au	7.55034269	4.45306272	4.86009002
S	9.43377829	4.45329819	3.17589923
C	9.43309269	4.45181272	1.39799998
H	11.29703269	5.52873272	1.23048998
H	7.56958269	3.37835272	1.22848998
C	10.47694269	5.05453272	0.69637998
C	10.48324269	5.05978272	-0.69458002
C	8.38420269	3.84977272	-0.69692002
C	8.39145269	3.85096272	0.69522998
H	11.29693269	5.53211272	-1.24060002
H	7.56849269	3.38200272	-1.24418002
C	9.43284269	4.45637272	-1.39447002
S	9.43497269	4.45764272	-3.17174002
Au	7.80784846	1.63192000	-4.86144002
Au	10.37949846	2.82002000	-4.86743002
Au	10.37981269	6.08669272	-4.86144002
Au	7.55034269	4.45306272	-4.86009002
Au	7.80753423	7.27479272	-4.86743002
Au	12.69427115	4.45306272	-4.86009002
Au	11.14517692	1.48492000	-7.23844002
Au	8.57321846	2.96985000	-7.23844002
Au	6.00125423	4.45477272	-7.23844002
Au	11.14518269	4.45477272	-7.23844002
Au	8.57321269	5.93969272	-7.23844002
Au	11.14518269	7.42462272	-7.23844002
Au	9.43053846	1.48492000	-9.66331002
Au	6.85856846	2.96985000	-9.66331002
Au	12.00249692	2.96985000	-9.66331002
Au	6.85857423	5.93969272	-9.66331002
Au	9.43053269	4.45477272	-9.66331002
Au	12.00250269	5.93969272	-9.66331002
Au	9.43053269	7.42462272	-9.66331002
Au	7.71589269	4.45477272	-12.08818000

Continued on next page

Table A.1 – continued from previous page

Atom Type	X	Y	Z
Au	10.28785846	2.96985000	-12.08818000
Au	10.28785269	5.93969272	-12.08818000
Au	7.72387181	1.48479035	-12.08177282
Au	7.72559365	7.42686223	-12.07125607
Au	12.85690016	4.46409916	-12.08287122
Au	11.14517692	1.48492000	-14.505
Au	11.14518269	7.42462272	-14.505
Au	8.57321269	5.93969272	-14.505
Au	11.14518269	4.45477272	-14.505
Au	8.57321846	2.96985000	-14.505
Au	6.00125423	4.45477272	-14.505
Au	9.43053269	4.45477272	-16.927
Au	12.00250269	5.93969272	-16.927
Au	9.44247983	7.42561905	-16.927
Au	9.43053846	1.48492000	-16.927
Au	6.85856846	2.96985000	-16.927
Au	12.00379407	2.97263118	-16.927
Au	6.85857423	5.93969272	-16.927
Au	7.71582314	1.48492	-19.349
Au	7.71581737	7.42462272	-19.349
Au	10.2877874	5.93969272	-19.349
Au	7.71581737	4.45477272	-19.349
Au	10.2877816	2.96985	-19.349
Au	12.8597458	4.45477272	-19.349
Au	11.1451769	1.48492	-21.771
Au	11.1451827	7.42462272	-21.771
Au	8.57321269	5.93969272	-21.771
Au	11.1451827	4.45477272	-21.771
Au	8.57321846	2.96985	-21.771
Au	6.00125423	4.45477272	-21.771
Au	9.43053269	4.45477272	-24.193
Au	12.0025027	5.93969272	-24.193
Au	9.44247983	7.42561905	-24.193
Au	9.43053846	1.48492	-24.193
Au	6.85856846	2.96985	-24.193
Au	12.0037941	2.97263118	-24.193
Au	6.85857423	5.93969272	-24.193
Au	7.71582314	1.48492	-26.615
Au	7.71581737	7.42462272	-26.615
Au	10.2877874	5.93969272	-26.615
Au	7.71581737	4.45477272	-26.615
Au	10.2877816	2.96985	-26.615

Continued on next page

Table A.1 – continued from previous page

Atom Type	X	Y	Z
Au	12.8597458	4.45477272	-26.615
Au	11.1451769	1.48492	-29.037
Au	11.1451827	7.42462272	-29.037
Au	8.57321269	5.93969272	-29.037
Au	11.1451827	4.45477272	-29.037
Au	8.57321846	2.96985	-29.037
Au	6.00125423	4.45477272	-29.037
Au	9.43053269	4.45477272	-31.459
Au	12.0025027	5.93969272	-31.459
Au	9.44247983	7.42561905	-31.459
Au	9.43053846	1.48492	-31.459
Au	6.85856846	2.96985	-31.459
Au	12.0037941	2.97263118	-31.459
Au	6.85857423	5.93969272	-31.459
Au	7.71582314	1.48492	-33.881
Au	7.71581737	7.42462272	-33.881
Au	10.2877874	5.93969272	-33.881
Au	7.71581737	4.45477272	-33.881
Au	10.2877816	2.96985	-33.881
Au	12.8597458	4.45477272	-33.881
Au	11.1451769	1.48492	-36.303
Au	11.1451827	7.42462272	-36.303
Au	8.57321269	5.93969272	-36.303
Au	11.1451827	4.45477272	-36.303
Au	8.57321846	2.96985	-36.303
Au	6.00125423	4.45477272	-36.303
Au	9.43053269	4.45477272	-38.725
Au	12.0025027	5.93969272	-38.725
Au	9.44247983	7.42561905	-38.725
Au	9.43053846	1.48492	-38.725
Au	6.85856846	2.96985	-38.725
Au	12.0037941	2.97263118	-38.725
Au	6.85857423	5.93969272	-38.725
Au	7.71582314	1.48492	-41.147
Au	7.71581737	7.42462272	-41.147
Au	10.2877874	5.93969272	-41.147
Au	7.71581737	4.45477272	-41.147
Au	10.2877816	2.96985	-41.147
Au	12.8597458	4.45477272	-41.147
Au	11.1451769	1.48492	-43.569
Au	11.1451827	7.42462272	-43.569
Au	8.57321269	5.93969272	-43.569

Continued on next page

Table A.1 – continued from previous page

Atom Type	X	Y	Z
Au	11.1451827	4.45477272	-43.569
Au	8.57321846	2.96985	-43.569
Au	6.00125423	4.45477272	-43.569
Au	9.43053269	4.45477272	-45.991
Au	12.0025027	5.93969272	-45.991
Au	9.44247983	7.42561905	-45.991
Au	9.43053846	1.48492	-45.991
Au	6.85856846	2.96985	-45.991
Au	12.0037941	2.97263118	-45.991
Au	6.85857423	5.93969272	-45.991

Bibliography

[1] M. A. Reed, C. Zhou, C. J. Muller, T. P. Burgin, and J. M. Tour. Conductance of a molecular junction. *Science*, 278(5336):252–254, October 1997.

[2] T. A. Jung, R. R. Schlittler, J. K. Gimzewski, H. Tang, and C. Joachim. Controlled Room-Temperature positioning of individual molecules: Molecular flexure and motion. *Science*, 271(5246):181–184, 1996.

[3] L. A. Bumm, J. J. Arnold, M. T. Cygan, T. D. Dunbar, T. P. Burgin, L. Jones, D. L. Allara, J. M. Tour, and P. S. Weiss. Are single molecular wires conducting? *Science*, 271(5256):1705–1707, March 1996.

[4] B. C. Stipe, M. A. Rezaei, and W. Ho. Single-Molecule vibrational spectroscopy and microscopy. *Science*, 280(5370):1732–1735, June 1998.

[5] G. Leatherman, E.N. Durantini, D. Gust, T.A. Moore, A.L. Moore, S. Stone, Z. Zhou, P. Rez, Y.Z. Liu, and S.M. Lindsay. Carotene as a molecular wire: Conducting atomic force microscopy. *Journal of Physical Chemistry B*, 103(20):4006–4010, May 1999.

[6] Hongkun Park, Jiwoong Park, Andrew K. L. Lim, Erik H. Anderson, A. Paul Alivisatos, and Paul L. McEuen. Nanomechanical oscillations in a single-C60 transistor. *Nature*, 407(6800):57–60, 2000.

[7] Philip G. Collins, Michael S. Arnold, and Phaedon Avouris. Engineering carbon nanotubes and nanotube circuits using electrical breakdown. *Science*, 292(5517):706–709, April 2001.

[8] X. D. Cui, A. Primak, X. Zarate, J. Tomfohr, O. F. Sankey, A. L. Moore, T. A. Moore, D. Gust, G. Harris, and S. M. Lindsay. Reproducible measurement of Single-Molecule conductivity. *Science*, 294(5542):571–574, October 2001.

[9] P.L. McEuen, M.S. Fuhrer, and Hongkun Park. Single-walled carbon nanotube electronics. *Nanotechnology, IEEE Transactions on*, 1(1):78–85, 2002.

[10] Wenjie Liang, Matthew P. Shores, Marc Bockrath, Jeffrey R. Long, and Hongkun Park. Kondo resonance in a single-molecule transistor. *Nature*, 417(6890):725–729, June 2002.

[11] Jiwoong Park, Abhay N. Pasupathy, Jonas I. Goldsmith, Connie Chang, Yuval Yaish, Jason R. Petta, Marie Rinkoski, James P. Sethna, Hector D. Abruna, Paul L. McEuen, and Daniel C. Ralph. Coulomb blockade and the kondo effect in single-atom transistors. *Nature*, 417(6890):722–725, June 2002.

[12] P. Avouris. Molecular electronics with carbon nanotubes. *Accounts of Chemical Research*, 35(12):1026–1034, December 2002.

[13] J.G. Kushmerick, J. Lazorcik, C.H. Patterson, R. Shashidhar, D.S. Seferos, and G.C. Bazan. Vibronic contributions to charge transport across molecular junctions. *Nano Letters*, 4(4):639–642, April 2004.

[14] X.Y. Xiao, B.Q. Xu, and N.J. Tao. Measurement of single molecule conductance: Benzenedithiol and benzenedimethanethiol. *Nano Letters*, 4(2):267–271, February 2004.

[15] N.P. Guisinger, M.E. Greene, R. Basu, A.S. Baluch, and M.C. Hersam. Room temperature negative differential resistance through individual organic molecules on silicon surfaces. *Nano Letters*, 4(1):55–59, 2004.

[16] R.L. McCreery. Molecular electronic junctions. *Chemistry of Materials*, 16(23):4477–4496, November 2004.

[17] K. Kitagawa, T. Morita, and S. Kimura. Molecular rectification of a helical peptide with a redox group in the Metal-Molecule-Metal junction. *Journal of Physical Chemistry B*, 109(29):13906–13911, July 2005.

[18] Ronald P. Andres, Thomas Bein, Matt Dorogi, Sue Feng, Jason I. Henderson, Clifford P. Kubiak, William Mahoney, Richard G. Osifchin, and R. Reifenberger. "Coulomb staircase" at room temperature in a Self-Assembled molecular nanostructure. *Science*, 272(5266):1323–1325, May 1996.

[19] R. Martel, T. Schmidt, H. R. Shea, T. Hertel, and Ph. Avouris. Single- and multi-wall carbon nanotube field-effect transistors. *Applied Physics Letters*, 73(17):2447–2449, October 1998.

[20] J. Chen, M. A. Reed, A. M. Rawlett, and J. M. Tour. Large On-Off ratios and negative differential resistance in a molecular electronic device. *Science*, 286(5444):1550–1552, November 1999.

[21] M. C. Hersam, N. P. Guisinger, J. Lee, K. Cheng, and J. W. Lyding. Variable temperature study of the passivation of dangling bonds at si(100)-2 x 1 reconstructed surfaces with h and d. *Applied Physics Letters*, 80(2):201–203, 2002.

[22] G. V. Nazin, X. H. Qiu, and W. Ho. Visualization and spectroscopy of a Metal-Molecule-Metal bridge. *Science*, 302(5642):77–81, October 2003.

[23] A. Salomon, D. Cahen, S. Lindsay, J. Tomfohr, V.B. Engelkes, and C.D. Frisbie. Comparison of electronic transport measurements on organic molecules. *Advanced Materials*, 15(22):1881–1890, 2003.

[24] David I. Gittins, Donald Bethell, David J. Schiffrin, and Richard J. Nichols. A nanometre-scale electronic switch consisting of a metal cluster and redox-addressable groups. *Nature*, 408(6808):67–69, November 2000.

[25] S.W. Wu, N. Ogawa, G.V. Nazin, and W. Ho. Conductance hysteresis and switching in a Single-Molecule junction. *Journal of Physical Chemistry C*, 112(14):5241–5244, April 2008.

[26] N. J. Tao. Electron transport in molecular junctions. *Nat Nano*, 1(3):173–181, December 2006.

[27] Latha Venkataraman, Jennifer E. Klare, Colin Nuckolls, Mark S. Hybertsen, and Michael L. Steigerwald. Dependence of single-molecule junction conductance on molecular conformation. *Nature*, 442(7105):904–907, 2006.

[28] David R. Penn. Electron mean-free-path calculations using a model dielectric function. *Physical Review B*, 35(2):482, 1987.

[29] B. J. van Wees, H. van Houten, C. W. J. Beenakker, J. G. Williamson, L. P. Kouwenhoven, D. van der Marel, and C. T. Foxon. Quantized conductance of point contacts in a two-dimensional electron gas. *Physical Review Letters*, 60:848, February 1988.

[30] J. M. Krans, C. J. Muller, I. K. Yanson, Th. C. M. Govaert, R. Hesper, and J. M. van Ruitenbeek. One-atom point contacts. *Physical Review B*, 48(19):14721, November 1993.

[31] D. A. Wharam, T. J. Thornton, R. Newbury, M. Pepper, H. Ahmed, J. E. F. Frost, D. G. Hasko, D. C. Peacock, D. A. Ritchie, and G. A. C. Jones. One-dimensional transport and the quantisation of the ballistic resistance. *Journal of Physics C: Solid State Physics*, 21(8):L209–L214, 1988.

[32] L. Olesen, E. Laegsgaard, I. Stensgaard, F. Besenbacher, J. Schio/tz, P. Stoltze, K. W. Jacobsen, and J. K. No/rskov. Quantized conductance in an atom-sized point contact. *Physical Review Letters*, 72(14):2251, April 1994.

[33] X. W. Tu, G. Mikaelian, and W. Ho. Controlling Single-Molecule negative differential resistance in a Double-Barrier tunnel junction. *Physical Review Letters*, 100(12):126807–4, March 2008.

[34] L.W. Yu, K.J. Chen, J. Song, J.M. Wang, J. Xu, W. Li, and X.F. Huang. Coulomb blockade induced negative differential resistance effect in a self-assembly si quantum dots array at room temperature. *Thin Solid Films*, 515(13):5466–5470, May 2007.

[35] Peter Liljeroth, Jascha Repp, and Gerhard Meyer. Current-Induced hydrogen tautomerization and conductance switching of naphthalocyanine molecules. *Science*, 317(5842):1203–1206, August 2007.

[36] F. D. M. Haldane. 'Luttinger liquid theory' of one-dimensional quantum fluids. i. properties of the luttinger model and their extension to the general 1D interacting spinless fermi gas. *Journal of Physics C: Solid State Physics*, 14(19):2585–2609, 1981.

[37] E. A. Jagla, K. Hallberg, and C. A. Balseiro. Numerical study of charge and spin separation in low-dimensional systems. *Physical Review B*, 47(10):5849, March 1993.

[38] C. Kollath, U. Schollwock, and W. Zwerger. Spin-Charge separation in cold fermi gases: A real time analysis. *Physical Review Letters*, 95(17):176401–4, October 2005.

[39] Marco Polini and Giovanni Vignale. Spin drag and Spin-Charge separation in cold fermi gases. *Physical Review Letters*, 98(26):266403–4, June 2007.

[40] Corinna Kollath and Ulrich Schollwck. Cold fermi gases: a new perspective on spin-charge separation. *New Journal of Physics*, 8(10):220, 2006.

[41] A. Recati, P. O. Fedichev, W. Zwerger, and P. Zoller. Spin-Charge separation in ultracold quantum gases. *Physical Review Letters*, 90(2):020401, 2003.

[42] Lars Kecke, Hermann Grabert, and Wolfgang Hausler. Charge and spin dynamics of interacting fermions in a One-Dimensional harmonic trap. *Physical Review Letters*, 94(17):176802–4, May 2005.

[43] Thilo Stoferle, Henning Moritz, Christian Schori, Michael Kohl, and Tilman Esslinger. Transition from a strongly interacting 1D superfluid to a mott insulator. *Physical Review Letters*, 92(13):130403, March 2004.

[44] Belen Paredes, Artur Widera, Valentin Murg, Olaf Mandel, Simon Folling, Ignacio Cirac, Gora V. Shlyapnikov, Theodor W. Hansch, and Immanuel Bloch. Tonks-Girardeau gas of ultracold atoms in an optical lattice. *Nature*, 429(6989):277–281, May 2004.

[45] C. Kollath, U. Schollwock, J. von Delft, and W. Zwerger. One-dimensional density waves of ultracold bosons in an optical lattice. *Physical Review A (Atomic, Molecular, and Optical Physics)*, 71(5):053606–9, May 2005.

[46] K. Hallberg, A. A. Aligia, A. P. Kampf, and B. Normand. Spin-Charge separation in Aharonov-Bohm rings of interacting electrons. *Physical Review Letters*, 93(6):067203, 2004.

[47] Shimul Akhanjee and Yaroslav Tserkovnyak. Spin-charge separation in a strongly correlated spin-polarized chain. *Physical Review B (Condensed Matter and Materials Physics)*, 76(14):140408–4, October 2007.

[48] A. A. Zvyagin. To the theory of spin–charge separation in one-dimensional correlated electron systems. *Low Temperature Physics*, 30(9):729–732, 2004.

[49] C. Livermore, C. H. Crouch, R. M. Westervelt, K. L. Campman, and A. C. Gossard. The coulomb blockade in coupled quantum dots. *Science*, 274(5291):1332–1335, November 1996.

[50] R. Landauer. Spatial variation of currents and fields due to localized scatterers in metallic conduction. *IBM Journal or Research and Development*, 1(3):223, 1957.

[51] Rolf Landauer. Electrical resistance of disordered one-dimensional lattices. *Philosophical Magazine*, 21(172):863, 1970.

[52] M. Buttiker, Y. Imry, R. Landauer, and S. Pinhas. Generalized many-channel conductance formula with application to small rings. *Physical Review B*, 31:6207, May 1985.

[53] M. Buttiker. Four-Terminal Phase-Coherent conductance. *Physical Review Letters*, 57(14):1761, October 1986.

[54] M. Buttiker. Absence of backscattering in the quantum hall effect in multiprobe conductors. *Physical Review B*, 38(14):9375, November 1988.

[55] Yongqiang Xue, Supriyo Datta, and Mark A. Ratner. First-principles based matrix green's function approach to molecular electronic devices: general formalism. *Chemical Physics*, 281(2-3):151–170, August 2002.

[56] Max Koentopp, Connie Chang, Kieron Burke, and Roberto Car. Density functional calculations of nanoscale conductance. *Journal of Physics: Condensed Matter*, 20(8):083203, 2008.

[57] F. Zahid, M. Paulsson, E. Polizzi, A. W. Ghosh, L. Siddiqui, and S. Datta. A self-consistent transport model for molecular conduction based on extended h[u-umlaut]ckel theory with full three-dimensional electrostatics. *The Journal of Chemical Physics*, 123(6):064707–10, 2005.

[58] Matthias Ernzerhof and Min Zhuang. Current transport through molecular electronic devices. *The Journal of Chemical Physics*, 119(8):4134–4140, 2003.

[59] Supriyo Datta and Michael Pepper Haroon Ahmad. *Electronic Transport in Mesoscopic Systems*. Cambridge Studies in Semiconductor Physics and Microelectronic Engineering. Cambridge University Press, 1997.

[60] Prashant Damle, Avik W. Ghosh, and Supriyo Datta. First-principles analysis of molecular conduction using quantum chemistry software. *Chemical Physics*, 281(2-3):171–187, August 2002.

[61] Per-Olov Lowdin. On the Non-Orthogonality problem connected with the use of atomic wave functions in the theory of molecules and crystals. *The Journal of Chemical Physics*, 18(3):365–375, March 1950.

[62] Istvan Mayer. *Simple Theorems, Proofs and Derivations in Quantum Chemistry*. Mathematical and Computational Chemistry. Springer, 1 edition, March 2003.

[63] J. J. Sakurai. *Modern Quantum Mechanics*. Addison Wesley, rev sub edition, September 1993.

[64] Yigal Meir and Ned S. Wingreen. Landauer formula for the current through an interacting electron region. *Physical Review Letters*, 68:2512, April 1992.

[65] Leo Kadanoff and Gordon Baym. *Quantum Statistical Mechanics*. Westview Press, Boulder, reprint edition, December 1994.

[66] V. Mujica, M. Kemp, and M. A. Ratner. Electron conduction in molecular wires. i. a scattering formalism. *The Journal of Chemical Physics*, 101(8):6849–6855, October 1994.

[67] M. P. Samanta, W. Tian, S. Datta, J. I. Henderson, and C. P. Kubiak. Electronic conduction through organic molecules. *Physical Review B*, 53(12):R7626, March 1996.

[68] Lachlan E. Hall, Jeffrey R. Reimers, Noel S. Hush, and Kia Silverbrook. Formalism, analytical model, and a priori green's-function-based calculations of the current–voltage characteristics of molecular wires. *The Journal of Chemical Physics*, 112(3):1510–1521, 2000.

[69] Supriyo Datta. Nanoscale device modeling: the green's function method. *Superlattices and Microstructures*, 28(4):253–278, October 2000.

[70] Tchavdar N. Todorov. Tight-binding simulation of current-carrying nanostructures. *Journal of Physics: Condensed Matter*, 14(11):3049–3084, 2002.

[71] P. Delaney and J. C. Greer. Correlated electron transport in molecular electronics. *Physical Review Letters*, 93(3):036805, July 2004.

[72] Jeremy Taylor, Hong Guo, and Jian Wang. Ab initio modeling of quantum transport properties of molecular electronic devices. *Physical Review B*, 63(24):245407, June 2001.

[73] P.A. Derosa and J.M. Seminario. Electron transport through single molecules: Scattering treatment using density functional and green function theories. *Journal of Physical Chemistry B*, 105(2):471–481, 2001.

[74] Mads Brandbyge, Jos-Luis Mozos, Pablo Ordejn, Jeremy Taylor, and Kurt Stokbro. Density-functional method for nonequilibrium electron transport. *Physical Review B*, 65(16):165401, March 2002.

[75] San-Huang Ke, Harold U. Baranger, and Weitao Yang. Electron transport through molecules: Self-consistent and non-self-consistent approaches. *Physical Review B*, 70(8):085410, 2004.

[76] Tomofumi Tada, Masakazu Kondo, and Kazunari Yoshizawa. Green's function formalism coupled with gaussian broadening of discrete states for quantum transport: Application to atomic and molecular wires. *The Journal of Chemical Physics*, 121(16):8050–8057, October 2004.

[77] Gemma C. Solomon, Jeffrey R. Reimers, and Noel S. Hush. Single molecule conductivity: The role of junction-orbital degeneracy in the artificially high currents predicted by ab initio approaches. *The Journal of Chemical Physics*, 121(14):6615–6627, October 2004.

[78] Gemma C. Solomon, Jeffrey R. Reimers, and Noel S. Hush. Overcoming computational uncertainties to reveal chemical sensitivity in single molecule conduction calculations. *The Journal of Chemical Physics*, 122(22):224502–7, June 2005.

[79] Vladimiro Mujica, Mathieu Kemp, Adrian Roitberg, and Mark Ratner. Current-voltage characteristics of molecular wires: Eigenvalue staircase, coulomb blockade, and rectification. *The Journal of Chemical Physics*, 104(18):7296–7305, May 1996.

[80] H. Ness and A. J. Fisher. Quantum inelastic conductance through molecular wires. *Physical Review Letters*, 83(2):452, July 1999.

[81] Tomasz Kostyrko and Bogdan R. Buka. Hubbard model approach for the transport properties of short molecular chains. *Physical Review B*, 67(20):205331, May 2003.

[82] Attila Szabo and Neil S. Ostlund. *Modern Quantum Chemistry: Introduction to Advanced Electronic Structure Theory*. Dover Publications, July 1996.

[83] N. Bushong, N. Sai, and M. DiVentra. Approach to Steady-State transport in nanoscale conductors. *Nano Letters*, 5(12):2569–2572, December 2005.

[84] Roi Baer, Tamar Seideman, Shahal Ilani, and Daniel Neuhauser. Ab initio study of the alternating current impedance of a molecular junction. *The Journal of Chemical Physics*, 120(7):3387–3396, February 2004.

[85] Qin Wu and Troy Van Voorhis. Direct optimization method to study constrained systems within density-functional theory. *Physical Review A (Atomic, Molecular, and Optical Physics)*, 72(2):024502–4, 2005.

[86] Q. Wu and T. VanVoorhis. Constrained density functional theory and its application in Long-Range electron transfer. *Journal of Chemical Theory and Computation*, 2(3):765–774, May 2006.

[87] Indranil Rudra, Qin Wu, and Troy Van Voorhis. Accurate magnetic exchange couplings in transition-metal complexes from constrained density-functional theory. *The Journal of Chemical Physics*, 124(2):024103–9, 2006.

[88] Massimiliano Di Ventra and Norton D. Lang. Transport in nanoscale conductors from first principles. *Physical Review B*, 65(4):045402, December 2001.

[89] D. S. Kosov and J. C. Greer. Many-electron systems with constrained current. *Physics Letters A*, 291(1):46–50, November 2001.

[90] D. S. Kosov. Lagrange multiplier based transport theory for quantum wires. *The Journal of Chemical Physics*, 120(15):7165–7168, April 2004.

[91] D. S. Kosov. Kohn–Sham equations for nanowires with direct current. *The Journal of Chemical Physics*, 119(1):1–5, July 2003.

[92] John P. Perdew, Robert G. Parr, Mel Levy, and Jose L. Balduz. Density-Functional theory for fractional particle number: Derivative discontinuities of the energy. *Physical Review Letters*, 49(23):1691, December 1982.

[93] John P. Perdew and Mel Levy. Physical content of the exact Kohn-Sham orbital energies: Band gaps and derivative discontinuities. *Physical Review Letters*, 51(20):1884, November 1983.

[94] L. J. Sham and M. Schl\"uter. Density-Functional theory of the energy gap. *Physical Review Letters*, 51(20):1888, November 1983.

[95] H. Appel, E. K. U. Gross, and K. Burke. Excitations in Time-Dependent Density-Functional theory. *Physical Review Letters*, 90(4):043005, 2003.

[96] W. J. Hehre, R. Ditchfield, R. F. Stewart, and J. A. Pople. Self-Consistent molecular orbital methods. IV. use of gaussian expansions of Slater-Type orbitals. extension to Second-Row molecules. *The Journal of Chemical Physics*, 52(5):2769–2773, March 1970.

[97] P. C. Hariharan and J. A. Pople. The influence of polarization functions on molecular orbital hydrogenation energies. *Theoretical Chemistry Accounts: Theory, Computation, and Modeling (Theoretica Chimica Acta)*, 28(3):213–222, 1973.

[98] P. Jeffrey Hay and Willard R. Wadt. Ab initio effective core potentials for molecular calculations. potentials for k to au including the outermost core orbitals. *The Journal of Chemical Physics*, 82(1):299–310, 1985.

[99] Ansgar Schafer, Hans Horn, and Reinhart Ahlrichs. Fully optimized contracted gaussian basis sets for atoms li to kr. *The Journal of Chemical Physics*, 97(4):2571–2577, 1992.

[100] Jan M. L. Martin and Andreas Sundermann. Correlation consistent valence basis sets for use with the Stuttgart–Dresden–Bonn relativistic effective core potentials: The atoms Ga–Kr and In–Xe. *The Journal of Chemical Physics*, 114(8):3408–3420, February 2001.

[101] Walter C. Ermler, Yoon S. Lee, Kenneth S. Pitzer, and Nicholas W. Winter. Ab initio effective core potentials including relativistic effects. II. potential energy curves for xe[sub 2], xe[sup +][sub 2], and xe*[sub 2]. *The Journal of Chemical Physics*, 69(3):976–983, 1978.

[102] S. Koseki, M. S. Godon, and M. W. Schmidt. Main group effective nuclear charges for Spin-Orbit calculations. *Journal of Physical Chemistry*, 99(34):12764–12772, 1995.

[103] Tracy P. Hamilton and Peter Pulay. Direct inversion in the iterative subspace (DIIS) optimization of open-shell, excited-state, and small multiconfiguration SCF wave functions. *The Journal of Chemical Physics*, 84(10):5728–5734, May 1986.

[104] Robert G. Parr and Yang Weitao. *Density-Functional Theory of Atoms and Molecules*. International Series of Monographs on Chemistry. Oxford University Press, USA, 1989.

[105] P. Hohenberg and W. Kohn. Inhomogeneous electron gas. *Physical Review*, 136(3B):B864, November 1964.

[106] Elliott H. Lieb and Barry Simon. Thomas-Fermi theory revisited. *Physical Review Letters*, 31(11):681, 1973.

[107] Elliott H. Lieb and Barry Simon. The Thomas-Fermi theory of atoms, molecules and solids. *Advances in Mathematics*, 23(1):22–116, 1977.

[108] H. Muller, E. Engel, and R. M. Dreizler. Extension of the relativistic Thomas-Fermi-Dirac-Weizscker model to arbitrary external fields. *Physical Review A*, 40(10):5542, November 1989.

[109] U. von Barth and L. Hedin. A local exchange-correlation potential for the spin polarized case. i. *Journal of Physics C: Solid State Physics*, 5(13):1629–1642, 1972.

[110] M. M. Pant and A. K. Rajagopal. Theory of inhomogeneous magnetic electron gas. *Solid State Communications*, 10(12):1157–1160, June 1972.

[111] P. A. M. Dirac. Note on exchange phenomena in the thomas atom. *Mathematical Proceedings of the Cambridge Philosophical Society*, 26(03):376–385, 1930.

[112] S. H. Vosko, L. Wilk, and M. Nusair. Accurate spin-dependent electron liquid correlation energies for local spin density calculations: a critical analysis. *Canadian Journal of Physics*, 58:1200–1211, 1980.

[113] A. D. Becke. Density-functional exchange-energy approximation with correct asymptotic behavior. *Physical Review A*, 38(6):3098, 1988.

[114] Chengteh Lee, Weitao Yang, and Robert G. Parr. Development of the Colle-Salvetti correlation-energy formula into a functional of the electron density. *Physical Review B*, 37(2):785, 1988.

[115] Renato Colle and Oriano Salvetti. Approximate calculation of the correlation energy for the closed shells. *Theoretical Chemistry Accounts: Theory, Computation, and Modeling (Theoretica Chimica Acta)*, 37(4):329–334, December 1975.

[116] P. J. Stephens, F. J. Devlin, C. F. Chabalowski, and M. J. Frisch. Ab initio calculation of vibrational absorption and circular dichroism spectra using density functional force fields. http://pubs.acs.org/doi/abs/10.1021/j100096a001, 1994.

[117] A. Savin. On degeneracy, near-degeneracy and density functional theory. In J. M. Seminario, editor, *Recent Developments and Applications of Modern Dnesity Functional Theory*, pages 327–357. Elsevier, Amsterdam, 1996.

[118] P. M. W. Gill. Coulomb-attenuated exchange energy density functionals. *Molecular Physics*, 88(4):1005–1010, 1996.

[119] Iann C. Gerber and Janos G. ngyn. Hybrid functional with separated range. *Chemical Physics Letters*, 415(1-3):100–105, October 2005.

[120] Oleg A. Vydrov, Jochen Heyd, Aliaksandr V. Krukau, and Gustavo E. Scuseria. Importance of short-range versus long-range Hartree-Fock exchange for the performance of hybrid density functionals. *The Journal of Chemical Physics*, 125(7):074106–9, 2006.

[121] C. Toher, A. Filippetti, S. Sanvito, and Kieron Burke. Self-Interaction errors in Density-Functional calculations of electronic transport. *Physical Review Letters*, 95(14):146402–4, 2005.

[122] Max Koentopp, Kieron Burke, and Ferdinand Evers. Zero-bias molecular electronics: Exchange-correlation corrections to landauer's formula. *Physical Review B (Condensed Matter and Materials Physics)*, 73(12):121403–4, March 2006.

[123] San-Huang Ke, Harold U. Baranger, and Weitao Yang. Role of the exchange-correlation potential in ab initio electron transport calculations. *The Journal of Chemical Physics*, 126(20):201102–4, May 2007.

[124] Na Sai, Michael Zwolak, Giovanni Vignale, and Massimiliano Di Ventra. Dynamical corrections to the DFT-LDA electron conductance in nanoscale systems. *Physical Review Letters*, 94(18):186810–4, May 2005.

[125] Erich Runge and E. K. U. Gross. Density-Functional theory for Time-Dependent systems. *Physical Review Letters*, 52(12):997, March 1984.

[126] E. Gross, J. Dobson, and M. Petersilka. *Density functional theory of time-dependent phenomena*, volume 181, pages 81–172. Springer, Berlin, 1996.

[127] Rdiger Bauernschmitt and Reinhart Ahlrichs. Treatment of electronic excitations within the adiabatic approximation of time dependent density functional theory. *Chemical Physics Letters*, 256(4-5):454–464, July 1996.

[128] So Hirata and Martin Head-Gordon. Time-dependent density functional theory for radicals: An improved description of excited states with substantial double excitation character. *Chemical Physics Letters*, 302(5-6):375–382, March 1999.

[129] Kieron Burke, Jan Werschnik, and E. K. U. Gross. Time-dependent density functional theory: Past, present, and future. *The Journal of Chemical Physics*, 123(6):062206–9, 2005.

[130] R. van Leeuwen and E. J. Baerends. Exchange-correlation potential with correct asymptotic behavior. *Physical Review A*, 49(4):2421, April 1994.

[131] Mark E. Casida, Christine Jamorski, Kim C. Casida, and Dennis R. Salahub. Molecular excitation energies to high-lying bound states from time-dependent density-functional response theory: Characterization and correction of the time-dependent local density approximation ionization threshold. *The Journal of Chemical Physics*, 108(11):4439–4449, March 1998.

[132] David J. Tozer. Effective homogeneity of the exchange-correlation energy functional. *Physical Review A*, 58(5):3524, November 1998.

[133] D. J. Tozer, R. D. Amos, N. C. Handy, B. O. Roos, and L Serrano-Andres. Does density functional theory contribute to the understanding of excited states of unsaturated organic compounds? *Molecular Physics*, 97(7):859–868, 1999.

[134] Andrzej L. Sobolewski and Wolfgang Domcke. Ab initio study of the excited-state coupled electron-proton-transfer process in the 2-aminopyridine dimer. *Chemical Physics*, 294(1):73–83, October 2003.

[135] Jrgen Fabian. Electronic excitation of sulfur-organic compounds performance of time-dependent density functional theory. *Theoretical Chemistry Accounts: Theory, Computation, and Modeling (Theoretica Chimica Acta)*, 106(3):199–217, July 2001.

[136] Rudolph Pariser and Robert G. Parr. A Semi-Empirical theory of the electronic spectra and electronic structure of complex unsaturated molecules. i. *The Journal of Chemical Physics*, 21(3):466–471, March 1953.

[137] J. A. Pople. Electron interaction in unsaturated hydrocarbons. *Transactions of the Faraday Society*, 49:1375–1385, 1953.

[138] K. Nishimoto and N. Mataga. Electronic structure and spectra of some nitrogen heterocycles. *Zeitschrift Fur Physikalische Chemie Neue Folge*, 12:335–338, 1957.

[139] N. Mataga and K. Nishimoto. Electronic structure and spectra of nitrogen heterocycles. *Zeitschrift Fur Physikalische Chemie Neue Folge*, 13:140–157, 1957.

[140] Chiao-Lun Cheng, Jeremy S. Evans, and Troy Van Voorhis. Simulating molecular conductance using real-time density functional theory. *Physical Review B (Condensed Matter and Materials Physics)*, 74(15):155112–11, October 2006.

[141] M. Petersilka, U. J. Gossmann, and E. K. U. Gross. Excitation energies from Time-Dependent Density-Functional theory. *Physical Review Letters*, 76(8):1212, February 1996.

[142] G. Stefanucci and C.-O. Almbladh. Time-dependent quantum transport: An exact formulation based on TDDFT. *EPL (Europhysics Letters)*, 67(1):14–20, 2004.

[143] Kieron Burke, Roberto Car, and Ralph Gebauer. Density functional theory of the electrical conductivity of molecular devices. *Physical Review Letters*, 94(14):146803–4, April 2005.

[144] M. Di Ventra and T. N. Todorov. Transport in nanoscale systems: the microcanonical versus grand-canonical picture. *Journal of Physics: Condensed Matter*, 16(45):8025–8034, 2004.

[145] S. Kurth, G. Stefanucci, C.-O. Almbladh, A. Rubio, and E. K. U. Gross. Time-dependent quantum transport: A practical scheme using density functional theory. *Physical Review B (Condensed Matter and Materials Physics)*, 72(3):035308–13, July 2005.

[146] Xiaofeng Qian, Ju Li, Xi Lin, and Sidney Yip. Time-dependent density functional theory with ultrasoft pseudopotentials: Real-time electron propagation across a molecular junction. *Physical Review B (Condensed Matter and Materials Physics)*, 73(3):035408–11, 2006.

[147] Wilhelm Magnus. On the exponential solution of differential equations for a linear operator. *Communications on Pure and Applied Mathematics*, 7(4):649–673, 1954.

[148] S. Blanes, F. Casas, J. A. Oteo, and J. Ros. Magnus and fer expansions for matrix differential equations: the convergence problem. *Journal of Physics A: Mathematical and General*, 31(1):259–268, 1998.

[149] S. Blanes, F. Casas, and J. Ros. Improved high order integrators based on the magnus expansion. *BIT Numerical Mathematics*, 40(3):434–450, 2000.

[150] High Performance Computational Chemistry Group. *NWChem, A Computational Chemistry Package for Parallel Computers, Version 4.6*. Pacific Northwest National Laboratory, Richland, Washington, USA, 2004.

[151] Gianluca Stefanucci. Bound states in ab initio approaches to quantum transport: A time-dependent formulation. *Physical Review B (Condensed Matter and Materials Physics)*, 75(19):195115–11, May 2007.

[152] Jeremy S. Evans, Chiao-Lun Cheng, and Troy Van Voorhis. Spin-charge separation in molecular wire conductance simulations. *Physical Review B (Condensed Matter and Materials Physics)*, 78(16):165108–11, October 2008.

[153] W. P. Su, J. R. Schrieffer, and A. J. Heeger. Solitons in polyacetylene. *Physical Review Letters*, 42(25):1698, June 1979.

[154] J. L. Bredas, R. R. Chance, and R Silbey. Theoretical study of charge transfer and bond alternation in doped polyacetylene. *Journal of Physical Chemistry*, 85(7):756–758, 1981.

[155] J. L. Bredas, R. R. Chance, and R. Silbey. Comparative theoretical study of the doping of conjugated polymers: Polarons in polyacetylene and polyparaphenylene. *Physical Review B*, 26(10):5843, November 1982.

[156] R. R. Chance, D. S. Boudreaux, J. L. Bredas, and R. Silbey. Neutral and charged soliton defects in polyacetylene. *Physical Review B*, 27(2):1440, 1983.

[157] D. S. Boudreaux, R. R. Chance, J. L. Bredas, and R. Silbey. Solitons and polarons in polyacetylene: Self-consistent-field calculations of the effect of neutral and charged defects on molecular geometry. *Physical Review B*, 28(12):6927, December 1983.

[158] J. L. Bredas and G. B. Street. Polarons, bipolarons, and solitons in conducting polymers. *Accounts of Chemical Research*, 18(10):309–315, 1985.

[159] S. Stafstrm and K. A. Chao. Soliton states in polyacetylene. *Physical Review B*, 29(4):2255, February 1984.

[160] S. Stafstrm and K. A. Chao. Polaron-bipolaron–soliton doping in polyacetylene. *Physical Review B*, 30(4):2098, 1984.

[161] Akira Terai and Yoshiyuki Ono. Phonons around a soliton and a polaron in Su-Schriffer-Heeger's model of trans-(CH)x. *Journal of the Physical Society of Japan*, 55:213–221, 1986.

[162] H. Wendel, P. Otto, M. Seel, and J. Ladik. Ab initio Hartree-Fock calculations of spin densities associated with bond alternating defects and end effects in trans-polyacetylene. *Solid State Communications*, 54(6):551–554, May 1985.

[163] W. Forner, C. L. Wang, F. Martino, and J. Ladik. Soliton dynamics in trans-polyacetylene using the full Pariser-Parr-Pople hamiltonian. *Physical Review B*, 37(9):4567, March 1988.

[164] Z. G. Soos and S. Ramasesha. Spin densities and correlations in regular polyene radicals. *Physical Review Letters*, 51(26):2374, December 1983.

[165] S. Mazumdar, S. Ramasesha, R. Torsten Clay, and David K. Campbell. Theory of coexisting charge- and Spin-Density waves in (TMTTF) 2Br, (TMTSF) 2PF 6, and alpha -(BEDT-TTF) 2MHg(SCN) 4. *Physical Review Letters*, 82(7):1522, February 1999.

[166] J.P. Pouget and S. Ravy. X-ray evidence of charge density wave modulations in the magnetic phases of (TMTSF)2PF6 and (TMTTF)2Br. *Synthetic Metals*, 85(1-3):1523–1528, March 1997.

[167] T. Sasaki and N. Toyota. Anisotropic galvanomagnetic effect in the quasi-two-dimensional organic conductor alpha -(BEDT-TTF)2KHg(SCN)4, where BEDT-TTF is bis(ethylenedithio)tetrathiafulvalene. *Physical Review B*, 49(15):10120, April 1994.

[168] M. V. Kartsovnik, A. E. Kovalev, I. F. Schegolev, V. N. Laukhin, N. D. Kushch, H. Ito, T. Ishiguro, G. Saito, and H. Mori. Magnetic field studies of the peculiar electronic state in the [alpha]-(BEDT-TTF)2MHg(SCN)4 family. *Synthetic Metals*, 70(1-3):811–814, March 1995.

[169] Y. Iye, R. Yagi, N. Hanasaki, Seiichi Kagoshima, H. Mori, H. Fujimoto, and G. Saito. The origin of anomalous angular dependent magnetoresistance oscillation effect in -(BEDT-TTF)2KHg(SCN)4. *Journal of the Physical Society of Japan*, 63:674–684, 1994.

[170] J. Caulfield, J. Singleton, P. T. J. Hendriks, J. A. A. J. Perenboom, F. L. Pratt, M. Doporto, W. Hayes, M. Kurmoo, and P. Day. Large magnetic-field-induced fermi surface changes in alpha -ET2KHg(NCS)4. *Journal of Physics: Condensed Matter*, 6(13):L155–L162, 1994.

[171] K. Miyagawa, A. Kawamoto, and K. Kanoda. 13C NMR study of nesting instability in alpha -(BEDT-TTF)2RbHg(SCN)4. *Physical Review B*, 56(14):R8487, October 1997.

[172] Hong Jiang, Harold U. Baranger, and Weitao Yang. Spin and Conductance-Peak-Spacing distributions in large quantum dots: A Density-Functional theory study. *Physical Review Letters*, 90(2):026806, 2003.

[173] Haitao Wang and Garnet Kin-Lic Chan. Self-interaction and molecular coulomb blockade transport in ab initio Hartree-Fock theory. *Physical Review B (Condensed Matter and Materials Physics)*, 76(19):193310–4, November 2007.

[174] C. Toher and S. Sanvito. Efficient atomic Self-Interaction correction scheme for nonequilibrium quantum transport. *Physical Review Letters*, 99(5):056801–4, 2007.

[175] Stephan Kummel, Leeor Kronik, and John P. Perdew. Electrical response of molecular chains from density functional theory. *Physical Review Letters*, 93(21):213002, November 2004.

[176] Yihan Shao, Laszlo Fusti Molnar, Yousung Jung, Jorg Kussmann, Christian Ochsenfeld, Shawn T. Brown, Andrew T.B. Gilbert, Lyudmila V. Slipchenko, Sergey V. Levchenko, Darragh P. O'Neill, Robert A. DiStasio Jr, Rohini C. Lochan, Tao Wang, Gregory J.O. Beran, Nicholas A. Besley, John M. Herbert, Ching Yeh Lin, Troy Van Voorhis, Siu Hung Chien, Alex Sodt, Ryan P. Steele, Vitaly A. Rassolov, Paul E. Maslen, Prakashan P. Korambath, Ross D. Adamson, Brian Austin, Jon Baker, Edward F. C. Byrd, Holger Dachsel, Robert J. Doerksen, Andreas Dreuw, Barry D. Dunietz, Anthony D. Dutoi, Thomas R. Furlani, Steven R. Gwaltney, Andreas Heyden, So Hirata, Chao-Ping Hsu, Gary Kedziora, Rustam Z. Khalliulin, Phil Klunzinger, Aaron M. Lee, Michael S. Lee, WanZhen Liang, Itay Lotan, Nikhil Nair, Baron Peters, Emil I. Proynov, Piotr A. Pieniazek, Young Min Rhee, Jim Ritchie, Edina Rosta, C. David Sherrill, Andrew C. Simmonett, Joseph E. Subotnik, H. Lee Woodcock III, Weimin Zhang, Alexis T. Bell, Arup K. Chakraborty, Daniel M. Chipman, Frerich J. Kiel, Arieh Warshel, Warren J. Hehre, Henry F.,III Schaefer, Jing Kong, Anna I. Krylov, Peter M. W. Gill, and Martin Head-Gordon. Advances in methods and algorithms in a modern quantum chemistry program package. *Physical Chemistry Chemical Physics*, 8(27):3172–3191, 2006.

[177] Magnus Paulsson and Sven Stafstrm. Self-consistent-field study of conduction through conjugated molecules. *Physical Review B*, 64(3):035416, June 2001.

[178] Swapan K. Pati. Transport in molecular wire with long-range coulomb interactions: A mean-field approach. *The Journal of Chemical Physics*, 118(14):6529–6535, April 2003.

[179] B. Muralidharan, A. W. Ghosh, and S. Datta. Probing electronic excitations in molecular conduction. *Physical Review B (Condensed Matter and Materials Physics)*, 73(15):155410–5, April 2006.

[180] Roi Baer and Daniel Neuhauser. Theoretical studies of molecular scale near-field electron dynamics. *The Journal of Chemical Physics*, 125(7):074709–9, 2006.

[181] Q. Wu and T. VanVoorhis. Direct calculation of electron transfer parameters through constrained density functional theory. *Journal of Physical Chemistry A*, 110(29):9212–9218, July 2006.

[182] Roi Baer, Ester Livshits, and Daniel Neuhauser. Avoiding self-repulsion in density functional description of biased molecular junctions. *Chemical Physics*, 329(1-3):266–275, October 2006.

[183] K. Capelle and E. K. U. Gross. Spin-Density functionals from Current-Density functional theory and vice Versa:A road towards new approximations. *Physical Review Letters*, 78(10):1872, March 1997.

[184] K. Capelle, G. Vignale, and B. L. Gyrffy. Spin currents and spin dynamics in Time-Dependent Density-Functional theory. *Physical Review Letters*, 87(20):206403, October 2001.

[185] San-Huang Ke, Harold U. Baranger, and Weitao Yang. Contact atomic structure and electron transport through molecules. *The Journal of Chemical Physics*, 122(7):074704–8, February 2005.

[186] Na Sai, Neil Bushong, Ryan Hatcher, and Massimiliano Di Ventra. Microscopic current dynamics in nanoscale junctions. *Physical Review B (Condensed Matter and Materials Physics)*, 75(11):115410–8, March 2007.

[187] C. Toher and S. Sanvito. Effects of self-interaction corrections on the transport properties of phenyl-based molecular junctions. *Physical Review B (Condensed Matter and Materials Physics)*, 77(15):155402–12, April 2008.

[188] David Lawrence Hill and John Archibald Wheeler. Nuclear constitution and the interpretation of fission phenomena. *Physical Review*, 89(5):1102, March 1953.

[189] James J. Griffin and John A. Wheeler. Collective motions in nuclei by the method of generator coordinates. *Physical Review*, 108(2):311, October 1957.

[190] K. Capelle. Variational calculation of many-body wave functions and energies from density functional theory. *The Journal of Chemical Physics*, 119(3):1285–1288, July 2003.

[191] E. Orestes, K. Capelle, A. B. F da Silva, and C. A. Ullrich. The generator coordinate method in time-dependent density-functional theory: memory made simple. *J. Chem. Phys.*, 127:124101, 2007.

[192] J. Paier, M. Marsman, K. Hummer, G. Kresse, I. C. Gerber, and J. G. \'Ang\'yan. Screened hybrid density functionals applied to solids. *The Journal of Chemical Physics*, 124(15):154709–13, April 2006.

[193] Masatoshi Imada, Atsushi Fujimori, and Yoshinori Tokura. Metal-insulator transitions. *Reviews of Modern Physics*, 70(4):1039, October 1998.

[194] Lars Hedin. New method for calculating the One-Particle green's function with application to the Electron-Gas problem. *Physical Review*, 139(3A):A796, 1965.

[195] John F. Stanton and Rodney J. Bartlett. The equation of motion coupled-cluster method. a systematic biorthogonal approach to molecular excitation energies, transition probabilities, and excited state properties. *The Journal of Chemical Physics*, 98(9):7029–7039, May 1993.

[196] G. Vignale and Mark Rasolt. Density-functional theory in strong magnetic fields. *Physical Review Letters*, 59(20):2360, November 1987.

[197] G. Vignale and Walter Kohn. Current-Dependent Exchange-Correlation potential for dynamical linear response theory. *Physical Review Letters*, 77(10):2037, 1996.

[198] G. Vignale, C. A. Ullrich, and S. Conti. Time-Dependent density functional theory beyond the adiabatic local density approximation. *Physical Review Letters*, 79(24):4878, December 1997.

[199] M. van Faassen, P. L. de Boeij, R. van Leeuwen, J. A. Berger, and J. G. Snijders. Ultranonlocality in Time-Dependent Current-Density-Functional theory: Application to conjugated polymers. *Physical Review Letters*, 88(18):186401, April 2002.

[200] Yongqiang Xue, Supriyo Datta, and Mark A. Ratner. Charge transfer and "band lineup" in molecular electronic devices: A chemical and numerical interpretation. *The Journal of Chemical Physics*, 115(9):4292–4299, 2001.

[201] David Q. Andrews, Revital Cohen, Richard P. Van Duyne, and Mark A. Ratner. Single molecule electron transport junctions: Charging and geometric effects on conductance. *The Journal of Chemical Physics*, 125(17):174718–9, November 2006.

[202] Yongqiang Xue and Mark A. Ratner. Microscopic study of electrical transport through individual molecules with metallic contacts. i. band lineup, voltage drop, and high-field transport. *Physical Review B*, 68(11):115406, 2003.

[203] J. O. Lee, G. Lientschnig, F. Wiertz, M. Struijk, R. A. J. Janssen, R. Egberink, D. N. Reinhoudt, P. Hadley, and C. Dekker. Absence of strong gate effects in electrical measurements on Phenylene-Based conjugated molecules. *Nano Letters*, 3(2):113–117, 2003.

[204] Xiulan Li, Bingqian Xu, Xiaoyin Xiao, Xiaomei Yang, Ling Zang, and Nongjian Tao. Controlling charge transport in single molecules using electrochemical gate. *Faraday Discussions*, 131:111–120, 2006.

[205] W. D. Wheeler and Yu. Dahnovsky. Molecular transistors based on BDT-type molecular bridges. *The Journal of Chemical Physics*, 129(15):154112–6, October 2008.

[206] A. W. Ghosh, T. Rakshit, and S. Datta. Gating of a molecular transistor: Electrostatic and conformational. *Nano Letters*, 4(4):565–568, 2004.

[207] Ante Bilic, Jeffrey R. Reimers, and Noel S. Hush. The structure, energetics, and nature of the chemical bonding of phenylthiol adsorbed on the au(111) surface: Implications for density-functional calculations of molecular-electronic conduction. *The Journal of Chemical Physics*, 122(9):094708–15, March 2005.

[208] J. S. Evans, O. Vydrov, and T. Van Voorhis. Exchange and correlation in molecular wire conductance: nonlocality is the key.